# Advancing probabilistic risk assessment of offshore wind turbines on monopiles

*David Wilkie*

A dissertation submitted in partial fulfillment

of the requirements for the degree of

**Doctor of Philosophy**

of

**University College London**.

Department of Civil, Environmental and Geomatic Engineering

University College London

February 9, 2020

I, David Wilkie, confirm that the work presented in this thesis is my own. Where information has been derived from other sources, I confirm that this has been indicated in the work.

# Abstract

Offshore Wind Turbines (OWTs) are a unique type of engineered structure. Their design spans all engineering disciplines, ranging from structural engineering for the substructure and foundation to electrical or mechanical engineering for the generating equipment. Consequently, the different components of an OWT are commonly designed independently using codified standards. Within the OWT design process, financial cost plays an important role as a constraint on decision making, because of the competition between prospective wind farm operators and with other forms of electricity generation. However, the current, independent design process does not allow for a combined assessment of OWT system financial loss. Nor does it allow for quantification of the uncertainties (e.g., wind and wave loading, materials properties) that characterise an OWT's operations and which may have a strong impact on decision making.

This thesis proposes quantifying financial losses associated with an OWT exposed to stochastic wind and wave conditions using a probabilistic risk modelling framework, as a first step towards evaluating Offshore Wind Farm (OWF) resilience. The proposed modelling framework includes a number of novel elements, including the development of site-specific fragility functions (relationships between the likelihood of different levels of damage experienced by an OWT over a range of hazard intensities), which account for uncertainties in both structural capacity and demands. As a further element of novelty, fragility functions are implemented in a closed-form assessment of financial loss, based on a combinatorial system reliability approach, which considers both structural and non-structural components.

Two important structural performance objectives (or limit states) are evaluated in this thesis: 1) the Ultimate Limit State (ULS) which assesses the collapse of an OWT due to extreme wind and wave conditions, such as those resulting from hurricanes; and 2) the Fatigue Limit State (FLS), which addresses the cumulative effects of operational loading, i.e., cracks growing over the life of the structure until they threaten its integrity. This latter limit state is assessed using a novel machine learning technique, Gaussian Process (GP) regression, to develop a computationally-efficient surrogate model that emulates the output from computationally-expensive time-domain structural analyses.

The consequence of the OWT failing is evaluated by computing annualised financial losses for the full OWT system. This provides a metric which is easily communicable to project stakeholders, and can also be used to compare the relative importance of different components and design strategies. Illustrative applications at case-study sites are presented as a walk-through of the calculation steps in the proposed framework and its various components. The calculation of losses provides a foundation from which a more detailed assessment of OWT and OWF resilience could be developed.

# Impact Statement

This thesis contributes towards developing resilience-based methods for improved design and assessment of OWTs. To achieve this aim, the thesis develops a set of novel techniques that can be used to quantify structural failure of OWTs. The failure of the structural components is then combined with the important equipment in terms of financial loss, providing an easily communicable metric of OWT performance.

The impact of this research can be summarised through societal, economic and academic elements.

The work is highly relevant to UK society in helping to achieve national and European targets associated with energy use and carbon reduction, particularly towards the legal obligations the UK has committed to under the 2015 Paris Agreement and the 2008 Climate Change Act. Impact in this area can be realised through public and private organisations implementing improved performance-based design and risk management strategies for OWTs based on the frameworks presented in this study. The study proposes new risk assessment techniques to help reducing the economic cost of offshore wind and therefore will aid the sectors future development.

With respect to economic impact, the outputs from this study may provide both the offshore wind and the (re)insurance industry with tools to perform improved risk assessment of OWTs. This will enable them to operate more competitively in the global energy and financing market, where there is competition to provide cost effective yet reliable energy generation.

Finally, this study addresses major intellectual challenges by going beyond

the state-of-the-art in assessment of OWTs by developing a comprehensive probabilistic risk assessment method for offshore infrastructure. It has resulted in academic impact, communicated through three journal papers:

1. D. Wilkie, C. Galasso, "Site-specific ultimate limit state fragility of offshore wind turbines on monopile substructures", *Engineering Structures*, under final review.

2. D. Wilkie, C. Galasso, "A probabilistic framework for offshore wind turbine loss assessment", *Renewable Energy*, under final review.

3. D. Wilkie, C. Galasso, "Using Gaussian processes in fatigue reliability assessment of offshore wind turbines", *Structural Safety*, under review.

Additionally, the research outcomes have been communicated through participation in international conferences including:

1. The 13th International Conference on Applications of Statistics and Probability in Civil Engineering (ICASP13), Seoul. The paper was awarded the the International Civil Engineering Risk and Reliability Association (CEERA) Student Recognition Award.

2. The 12th International Conference on Structural Safety & Reliability (ICOSSAR12), Vienna. The work presented won the The International Association for Structural Safety and Reliability (IASSAR) student scholarship.

3. The European Geophysics Union (EGU) 2019, Vienna.

4. The Urban Sustainability and Resilience conference 2017, London.

5. The European Association of Wind Energy PhD forum 2017, Milton Keynes.

# Acknowledgements

This project was supported by the UK Engineering and Physical Sciences Research Council DTP grant EP/M507970/1 which was greatly appreciated. Completing this PhD has been a truly rewarding experience, not least due to the large number of people have contributed to its success with their ideas, motivation, and support. In particular, I would like to thank:

My primary supervisor Dr Carmine Galasso, whose commitment to academic research is inspiring. Thank you for your continual support throughout the PhD, providing me with technical, and more importantly moral support, pushing me to improve my research and investigate new areas. I would also like to thank my second supervisor Dr Phillippe Duffour who influenced my growth as a researcher, and especially for providing feedback on my thesis.

All the students, faculty and staff associated with EPICentre. I am grateful to remain part of this welcoming research group, and have enjoyed all the workshops, dinners and parties we've had together.

The wider CEGE community, especially those sitting in the research office office GM16. It's been wonderful to share your with successes, and more late night fast food than is healthy.

Finally, I would like to express my deep gratitude to my family and friends for their constant support and encouragement. Especially my girlfriend Mian for being by my side throughout. Also my mum, dad and brother, the number of chocolates you've posted me over the past three years has been truly overwhelming.

David Wilkie - UCL London, July 2019

# Contents

# List of Figures

# List of Tables

# Acronyms

| | |
|---|---|
| AF | Apparent Fixity. |
| CAT | Catastrophe Risk. |
| CCDF | Complementary Cumulative Distribution Function. |
| CDF | Cumulative Distribution Function. |
| CoV | Coefficient of Variation. |
| DAF | Dynamic Amplification Factor. |
| DEL | Design Equivalent Load. |
| DLC | Design Load Case. |
| DM | Damage Measure. |
| DNVGL | Det Norske Veritas Germanischer Lloyd. |
| DOE | Design of Experiment. |
| DS | Damage State. |
| DV | Decision Variable. |
| EDP | Engineering Design Parameter. |
| EL | Elevation. |
| EP | Exceedance Probability. |
| FAST | Fatigue Aerodynamics Structures and Turbulence. |

| | |
|---|---|
| FEA | Finite Element Analysis. |
| FLS | Fatigue Limit State. |
| FORM | First Order Reliability Method. |
| GEV | Generalised Extreme Value. |
| GP | Gaussian Process. |
| iCDF | Inverse Cumulative Distribution Function. |
| IEC | International Electrotechnical Commission. |
| IJ | Ijmuiden. |
| IM | Intensity Measure. |
| ISO | International Standards Organisation. |
| IWWA | Incremental Wind-Wave Analysis. |
| KDE | Kernel Density Estimator. |
| LCoE | Levelised Cost of Energy. |
| LRFD | Load Resistance Factored Design. |
| MA | Massachusetts. |
| MLE | Maximum Likelihood Estimation. |
| MRP | Mean Return Period. |
| MSL | Mean Sea Level. |
| MW | Mega watt. |
| NREL | National Renewable Energy Laboratory. |
| OWF | Offshore Wind Farm. |
| OWT | Offshore Wind Turbine. |

| | |
|---|---|
| PBE | Performance Based Engineering. |
| PDF | Probability Density Function. |
| PMF | Probability Mass Function. |
| PPD | Presidential Policy Directive. |
| RNA | Rotor Nacelle Assembly. |
| SE | Squared-Exponential (kernel function). |
| SN | Stress Life. |
| ULS | Ultimate Limit State. |

# List of Symbols

| | |
|---|---|
| $\alpha$ | Scale mixture parameter in the rational quadratic covariance function |
| $\mathbb{E}$ | Expectation |
| $\epsilon$ | Error in surrogate model |
| $\hat{\beta}$ | Standard deviation of log-normal distribution |
| $\hat{\eta}$ | Median of log-normal distribution |
| $\hat{\mathbf{x}}$ | Set of test input variables |
| $\hat{h}(\cdot)$ | Emulator of relationship predicting structural demand |
| $\hat{y}$ | Estimate of response variable |
| $\lambda$ | Mean annual rate of occurrence |
| $\lambda_{f,DS}$ | Rate of failure for a given damage state |
| $\mu_{\hat{\mathbf{x}}}$ | Conditional mean vector |
| $\mu_{GEV}$ | Location parameter for the generalised extreme value distribution |
| $\phi$ | Diameter of beam cross-section (m) |
| $\phi_R$ | Rotor diameter (m) |
| $\sigma_f$ | Variance in the squared exponential covariance function |
| $\sigma_n$ | Noise in surrogate model |

$\sigma_r$ Applied stress range ($N/m^2$)

$\sigma_{Ax}$ Axial membrane stress in wall cross-section ($N/m^2$)

$\sigma_{Bm}$ Bending membrane stress in wall cross-section ($N/m^2$)

$\sigma_{GEV}$ Scale parameter for the generalised extreme value distribution

$\sigma_{Mem}$ Total membrane stress in beam cross-section ($N/m^2$)

$\sigma_{TP}$ Von Mises stress in transition piece in grout ($N/m^2$)

Conditional covariance matrix

$\mathbf{K}$ Unconditional covariance matrix

$\mathbf{A}$ Matrix of system failure events

$\mathbf{a}^*$ Subset of failure events with events of an equivalent specified cost

$\mathbf{A}_c$ Matrix of system failure costs

$\mathbf{w}$ Vector of weights in the surrogate model

$\theta_{CS}$ Angle around beam cross-section (deg)

$\theta_{mis}$ Misalignment between wind and wave inflow angle (deg)

$\theta_{wa}$ Wave inflow angle (deg)

$\theta_{wi}$ Wind inflow angle (deg)

$b$ Structural performance threshold

$C$ Consequence of failure

$c_r$ Direct material loss due to a failure event (k€)

$c_{mon}$ Cost of monopile (k€)

$C_{storms}$ Consequence of storms occurring

$C_{WT}$ Cost of wind turbine (k€)

$D_j$ Fatigue damage calculated for a set of environmental conditions

$D_{j,life}$ Damage calculated over component life

$DEL$ Design equivalent load

$E$ Young's Modulus ($N/m^2$)

$Ev$ An event

$F$ Cumulative distribution function

$f$ Probability density function

$f_E$ Probability density function of environmental conditions

$F_y$ Yield strength ($N/m^2$)

$f_{\Sigma p}$ Probability density function of stress range

$f_{cap,M}$ Buckling resistance of tower cross-section ($N/m^2$)

$f_{cap,T}$ Buckling resistance of tower cross-section ($N/m^2$)

$f_{TP}$ Maximum transition piece limit state function ($N/m^2$)

$G$ Limit state function

$g$ Acceleration due to gravity ($m/s^2$)

$G(t, X)$ Fatigue limit state, dependent on time

$G_{BLD}$ Blade limit state

$G_{DLife}$ Fatigue limit state evaluated over component design life

$G_{DNV,M}$ DNV GL limit state applied to the OWT monopile

$G_{DNV,T}$ DNV GL limit state applied to the OWT tower

$G_{i,k}$ Limit state function identified by the $k$ index

$G_{MCR}$ Critical moment limit state function

$G_{TP}$ Transition piece limit state

$h(\cdot)$ Relationship predicting structural demand

$H_s$ Significant wave height (m)

$h_{hub}$ Hub height (m)

$h_{water}$ Water depth (m)

$i_c$ Cross-section radius of gyration (m)

$I_F$ Indicator function

$K_\mu$ SN curve x-axis intersection

$k_{GEV}$ Shape parameter for the generalised extreme value distribution

$k_{MT,5/2}$ Matern 3/2 covariance function

$k_{MT,5/2}$ Matern 5/2 covariance function

$k_{RQ}$ Rational quadratic covariance function

$k_{SE}$ Squared exponential covariance function

$L$ Financial loss (k€)

$L_c$ Length of cylinder (m)

$L_{ef}$ Effective length of a beam

$Loss_{total}$ Total system loss (k€)

$m$ SN curve slope

$M_{CAP}$ Moment capacity of a blade (Nm)

$M_{DEM}$ Moment demand of a blade (Nm)

$M_{FA}$ Bending moment acting on beam in fore-aft direction ($Nm$)

$M_{SS}$ Bending moment acting on beam in side-to-side direction ($Nm$)

$M_{ULT}$ Maximum bending moment capacity of cross section (Nm)

$N$ Number of cycles to fatigue failure

$n$ Number of fatigue cycles experience by a component

$N_{Ax}$ Axial force acting on beam ($N$)

$N_{EQ}$ Equivalent number of cycles used in DEL calculation

$N_{LSamp}$ Number of limit state samples in fatigue reliability calculation

$N_{MRP}$ Number of MRP evaluated when fitting the fragility function

$N_{samples}$ Number of samples used to evaluate $P_f$

$N_{SMP}$ Number of samples of environmental conditions in fatigue damage estimation

$N_{sys}$ Number of system components

$P_f$ Probability of failure

$P_i$ Probability of failure of the ith system component

$P_{sys}$ Probability of system failure

$P_{WT}$ Power of wind turbine (MW)

$Pr_j$ Probability of discrete environmental condition occurring

$R$ Structural resilience

$R(t, X)$ Fatigue capacity over time

$R_{DLife}$ Fatigue capacity evaluated over component design life

$RRI$ Relative resilience indicator

$S(t, X)$ Fatigue demand over time

$S_{DLife}$ Fatigue demand evaluated over component design life

$t$ Thickness of beam cross section (m)

$t$ Time

$T_i$ Turbulence intensity (%)

$T_p$ Peak spectral period (s)

$T_{analysis}$ Time simulated in structural analysis (hr)

$T_{life}$ Design life of component (hr)

$V_w$ Mean wind speed (m/s)

$X$ Set of input variables

$X_.$ Random variable, identified by the subscript

$x_{GEV}$ Input parameter for the generalised extreme value distribution

$y$ Response variable

# Chapter 1

# Introduction

## 1.1 Offshore wind energy

The European Wind Energy Association reports that the offshore wind industry began in 2000 [20] when the first utility-scale OWF was installed in the Danish sector of the North Sea, at the Middelgrunden site. This makes offshore wind a relatively recent form of energy production compared to others, even onshore wind which is now over 40 years old [21]. However, within this short history large changes have occurred, including: rapid growth in OWT capacity, increases in the size of OWFs, and recent reductions in the Levelised Cost of Energy (LCoE) (i.e., the amount of money the generator charges for each Mega watt (MW) hour of energy produced over the full life of the OWF). Increases in OWT capacity have been such that the average rated capacity of an OWT installed in 2018 was around 7MW, more than three times the 2MW average capacity of OWT installed in 2000 [2]. Many of these changes are a result of the industry working towards best practice in designing, constructing and maintaining offshore assets, and governments improving policy to support this activity [22].

The recent growth in total wind energy capacity, both offshore and onshore wind, makes it the second largest source of electricity generation in Europe, as shown in Figure 1.2. Since 2016 wind energy generation has been consistently just behind natural gas, which has around 190GW of installed capacity [23].

Indeed, if the trend shown on this figure continues wind will be the largest form of energy production by 2021. The global offshore wind industry has grown to the point that approximately 21GW of capacity are currently installed [24]. However, this means that the offshore industry is still small compared to the onshore wind industry which, in Europe alone, has over 160GW of installed capacity [23].

Nevertheless, offshore wind capacity continues to grow with Europe being the focus of this expansion to date. It provides 88% (18.5GW) of worldwide

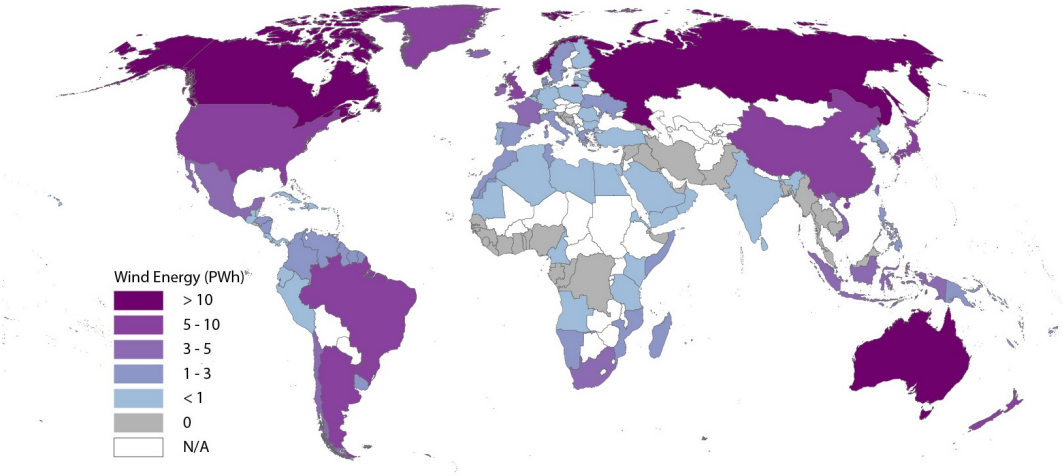


**Figure 1.1:** Distribution of wind offshore wind energy density by country, taken from [1].

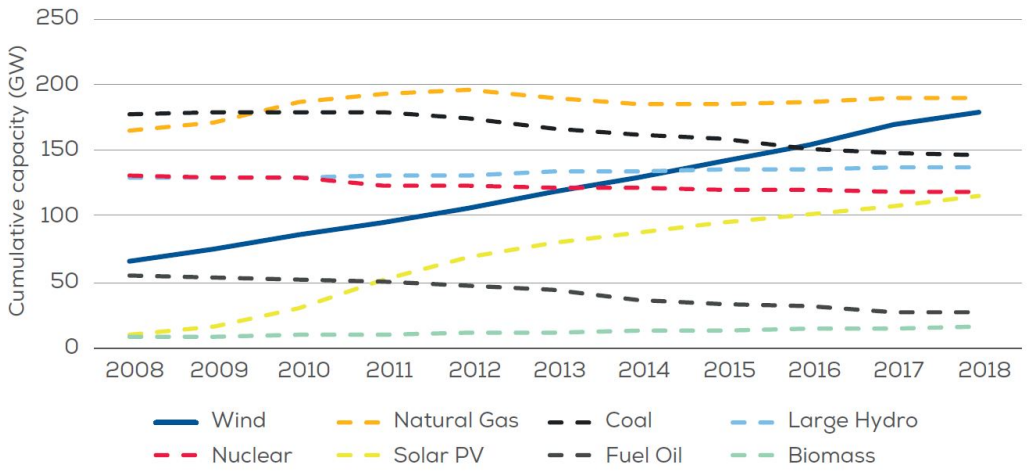


**Figure 1.2:** Energy production from different sources in the UK between 2008 and 2018. Taken from Selot et al. [2].

installed capacity as of 2018, the year with most recent statistics, and a further 25GW worth of projects due to be installed by 2020 [25, 2]. The UK currently has the largest market share of any single country at 43% of European capacity [2] (or 38% of 2017 world capacity). The concentration within Europe is partly due to formal agreements entered into by European governments to increase reliance on renewable sources, including a European Commission target to source "20% primary energy demand from renewable sources by 2020". Individual governments have committed to developing offshore wind, including the UK government which has committed to supporting 30GW of offshore wind energy by 2030 [22]. Additionally, the high wind energy density around the North Sea means that farms in this region will have a particularly high energy yield, as indicated in Figure 1.1, which shows the offshore wind energy yield for each country with a sea border. Indeed, the UK Parliament's Committee for Climate Change [22] recently highlighted that the UK has the potential to support between 95GW and 245GW of offshore wind energy generation, compared to only 29GW to 96GW of onshore wind. Zheng et al. [26] highlighted that high offshore wind energy density is present in other geographical regions, some of which have plans to install OWFs, including North America [24] and East Asia [27, 28, 11]. However, there is also high energy density in locations currently without well-developed plans to install OWFs such as South America, Australia, and South Africa, as shown in Figure 1.1. This suggests a large potential for future growth in offshore wind generation that surpasses the currently planned farms. Therefore, offshore wind has the potential to become an important part of the energy mix in many countries even although current installed capacity is relatively small.

Building an OWF is very capital intensive, and the ability to complete a project is influenced by the cost at which the OWF developer can borrow [29]. In total around 70% of this capital cost is spent on the turbine and foundations, as shown on Figure 1.3 which shows a breakdown of the capital cost of different components for a typical bottom-fixed OWT. Any reduction in the capital cost

will have the knock-on effect of reducing the cost of capital, as less borrowing will be necessary. Additionally, any reduction in risk will have an indirect effect on the cost of capital, due to lower risk premiums. However, these costs have historically been high for offshore wind compared to other forms of electricity generation, the high cost in 2012 is shown on Figure 1.4 compared to other forms of electricity generation. Consequently, offshore wind energy production has required support from national governments in order to make the long-term financial commitments viable. The mechanism for supporting OWF development currently used in the UK is the 'contract for difference' [30], in which wind farm operators bid for zones, and the most competitive bid is awarded a contract to develop the site. These contracts typically last for 15 years [30] and provide a minimum guaranteed income to the operator for the electricity they generate. This is referred to as the strike price, and is the amount paid (£/MWh) to an OWF operator for each megawatt hour (MWh) of electricity produced. This effectively shields them from fluctuations in wholesale electricity prices. The LCoE is the cost the operator will incur and includes capital costs, operating costs and borrowing costs (i.e. the cost of capital). Lowering the LCoE lowers the strike price at which operators can bid to develop a site and still make a profit. Consequently, reducing LCoE gives operators a competitive advantage over their rivals. Recent auctions have resulted in strike prices below the most ambitious targets set by the Crown Estate's Cost Reduction Pathways Study published in 2012 [31] which envisioned cost reduction to a LCoE of £100/MWh by 2020. The reductions also beat the previous industry predictions of LCoE reaching £115/MWh by the mid 2020s [11]. In the UK, the average LCoE for a new OWF, calculated in 2016, was £97/MWh [32]. Furthermore recent auctions in the Netherlands and Denmark have resulted in strike prices much lower [30, 33], leading to a global LCoE around £92/MWh [34]. These reductions mean offshore wind has become a competitive form of energy production, with lower LCoE than nuclear and in some cases even gas as indicated on Figure 1.4. However, this

later result is dependent on the ease with which the OWF site can be developed [30], e.g., if there are existing electrical connections to the shore present from nearby OWFs. The overall LCoE of offshore wind is still much higher than onshore wind, which had a 2018 global LCoE of around £50/MWh [34].

Cost reduction remains an important goal for OWF operators as:

- The recent reductions in cost are partially due to historically low borrowing costs [30] and therefore exposed to fluctuations in economic con-

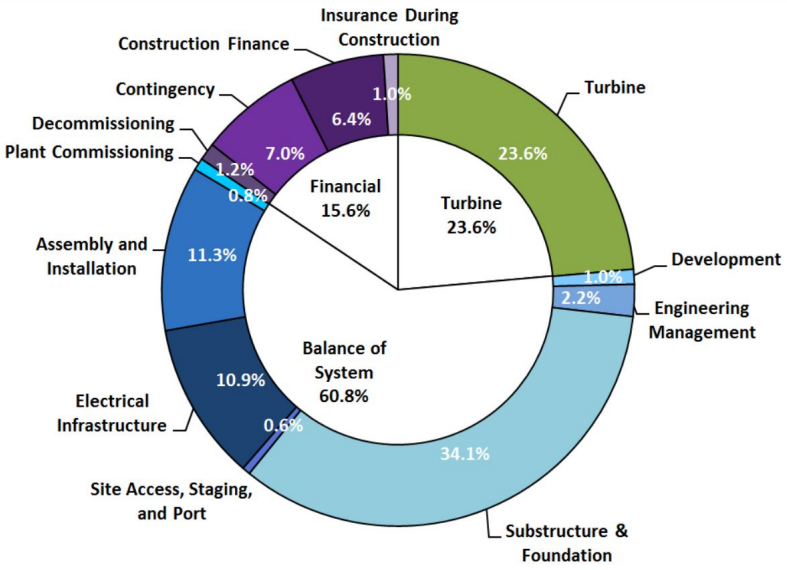


**Figure 1.3:** Capital cost breakdown of an OWT components for a reference OWT. Taken from Stehly et al. [3].

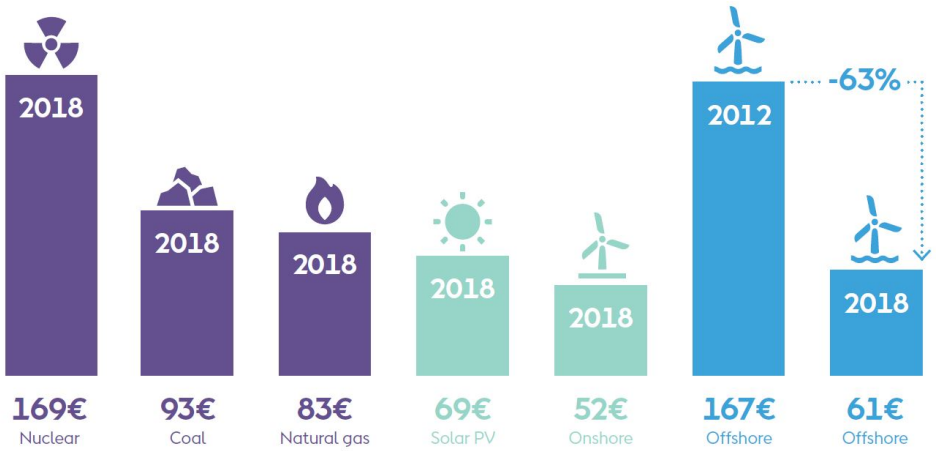


**Figure 1.4:** Cost of different types of energy, in terms of 2017 Euros. Taken from Orsted [4].

ditions.

- The auction mechanism for assigning OWF zones mean that additional cost reduction will give bidding consortia a competitive advantage over the other bidders.

Additionally, lower costs could improve the uptake of offshore wind in markets without current plans for installations.

The Leanwind project [35] reviewed potential cost saving strategies and highlighted that "Optimised foundations and novel designs need to be developed". However novel technologies have been associated with higher borrowing costs, due to technological risk, especially on offshore wind projects [36]. Probabilistic risk modelling that can quantify the reliability of OWT structures could help confirming the adequacy of new technologies, by quantifying their risk in terms of lifetime financial losses and structural and nonstructural safety. Additionally, these techniques could potentially be used to identify more optimised and capitally-efficient designs than attainable by current prescriptive code-based approaches [37].

Achieving improved, integrated, design is challenging as OWTs are unique engineering structures which depend on:

- electrical components - including a control system which regulates energy production;
- mechanical components - including a generator, drive train and gearbox;
- and structural components - comprising a tower, monopile, transition piece and blades;

to remain operational. Currently, design of these systems is fragmented as all components are designed separately. This is especially true in the case of structural design which is undertaken at the component level, where the tower and monopile are designed separately, often by different companies [38]. There is a large gap between current practice and considering these structures

as integrated systems comprised of structural and mechanical components. Within this thesis, the framework of risk and resilience will be seen to provide suitable tools for approaching this problem in a rigorous and quantitative way.

## 1.2 Offshore wind turbines

OWTs are typically much larger than their onshore counterparts. The largest onshore wind turbine can produce 4.8MW of power compared to the largest OWT which has a rated capacity of 9.5MW and a rotor diameter of 164m. The growth in the size of OWT is charted in Figure 1.5, which shows their development over time. Since 2002 the capacity and size of OWTs have increased rapidly meaning that large specialist vessels are now used to assemble them offshore.

Within an OWF, the individual OWTs are comprised of similar components, allowing "mass" manufacturing. However, there are different mechanisms that are used to attach the turbine to the seabed, as summarised by Vorpahl et al. [39]. Floating OWTs are attracting a lot of interest in the current research setting; however, to date, few have been installed in commercial OWFs. For OWTs that are fixed to the seabed (fixed-bottom), there are a range of support-structure types available. This thesis focuses on OWT supported by monopile foundations, as these comprise over 80% of existing offshore wind installations [2] and will be used in large quantities in future developments [40]. They have been found to be more adaptable than originally envisaged, providing the most cost efficient foundation solution over a range of water depths up to 38m [41]. These foundations take the form of large cylindrical members, with diameters up to 10m, which are driven into the seabed. An example of this foundation type is shown in Figure 1.6. A platform is then placed on top of the monopile; it allows correction of rotations introduced during installation and supports the walkways that allow maintenance crews access to the OWT.

The main structural components of a bottom fixed OWT are defined in

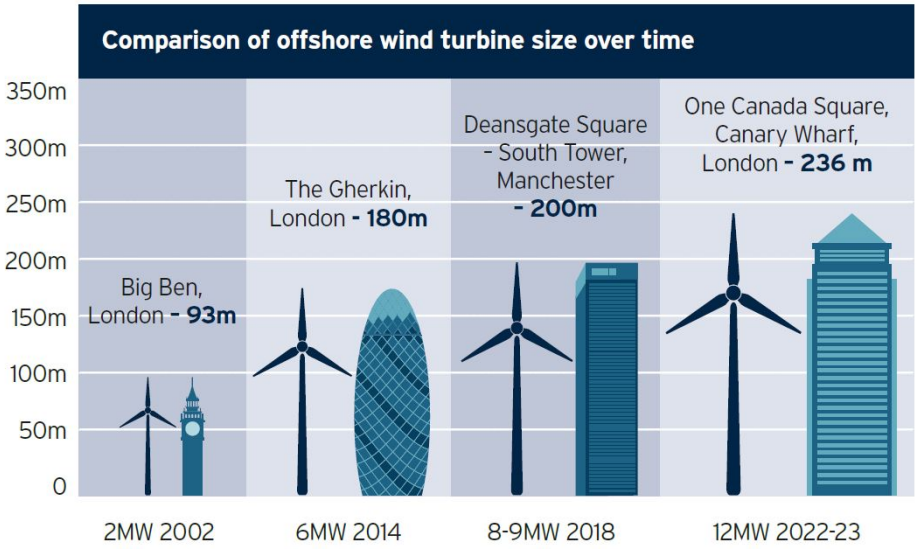


**Figure 1.5:** Increasing average size and capacity of offshore wind turbines with time, taken from [5].

the design code International Electrotechnical Commission (IEC) 61400-3 [6] and are shown on a typical turbine structure in Figure 1.6. The components include a support structure comprised of: a foundation, a tower and a sub-structure (which spans between the seabed to the tower). The Rotor Nacelle Assembly (RNA) is located on top of the tower and contains the majority of equipment used to generate electricity. This component sits on bearings and can rotate about the vertical (central) axis of the tower. When the direction of the wind changes the yaw system pivots the RNA into the wind direction so that the rotor is perpendicular to the incoming wind flow, maximising energy production. Each of the three blades connects to the hub and is installed on its own set of bearings, allowing them to rotate about their central axis and regulate the speed at which the rotor turns [11]. A shaft connects the rotor and gearbox through a hole in the front of the RNA, transmitting rotations from the blades into the generator.

The majority of OWT are operated using a variable speed, torque and pitch controller, which regulates the angle of the blades relative to the incoming wind. It attempts to produce a constant torque on the generator after the wind speed at the RNA height reaches a pre-defined threshold. This rated wind

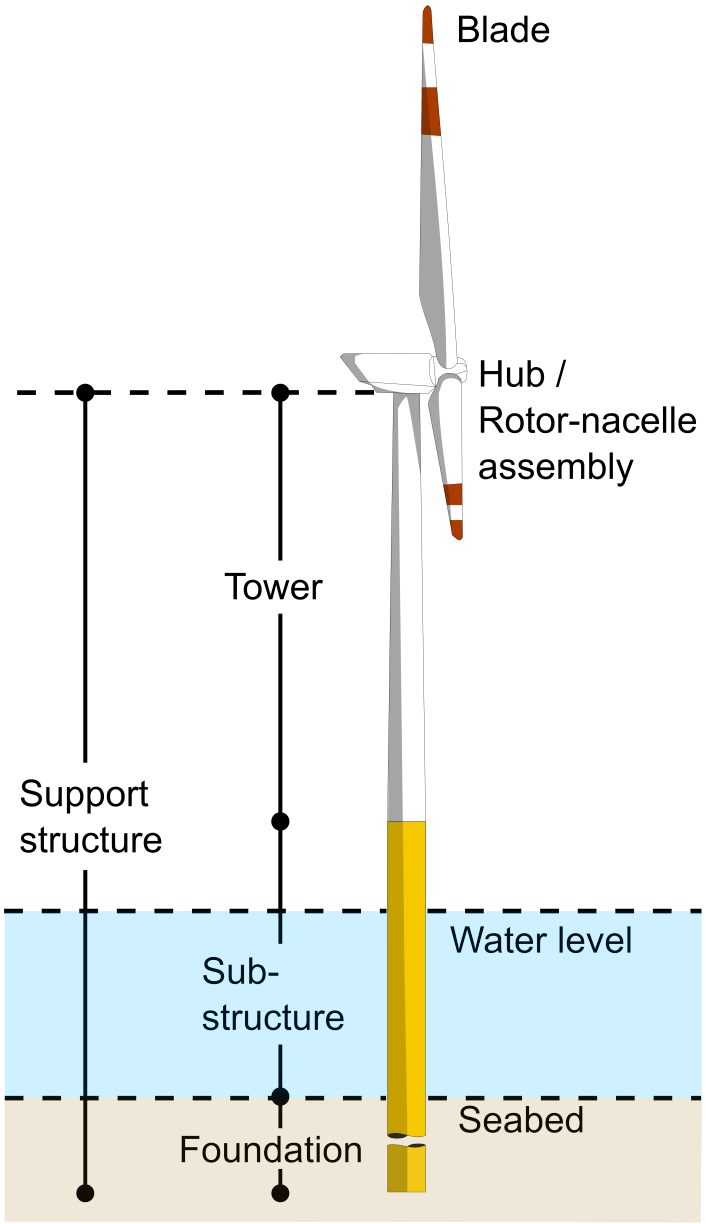


**Figure 1.6:** Components of an offshore wind turbine as defined in IEC 61400-3 [6].

speed is associated with the largest operational thrust forces; for instance, a common OWT used in academic research has a rated speed of $12m/s$ [42]. Separately, a cut-in and cut-out speed govern the RNA mean wind speed at which the OWT will start to produce electricity or will shut-down to protect itself from high loading during storms. When in the shut-down state, the blades are pitched 90° into the wind, minimising lift forces and preventing the rotor from spinning. This means that rotor thrust has a complex, non-linear, relationship to the mean wind speed [11], which is important to capture in the assessment of OWT loads.

## 1.3 Research objectives

Cost reduction remains an important objective when planning offshore wind installations. This is especially true as the OWT is unmanned for most of its operating life, and therefore life safety issues are not a paramount concern. As highlighted in Section 1.1, probabilistic risk modelling may be used to justify designs which are less conservative than those produced by traditional approaches based on design codes. However, suitable integrated assessment techniques for quantifying financial losses do not currently exist, particularly for the structure, as emphasised in the Leanwind project [35]. Motivated by these observations, the primary questions that this thesis aims to answer are: can computational tools be developed that allow integrated assessment of OWT performance? How can OWT structural and non-structural performance be communicated to stakeholders? The research vision which addresses these questions is the development of an advanced, harmonised and engineering-based risk assessment framework for offshore wind energy installations.

This overall aim can be split into a series of objectives and related tasks. Most of these focus on the OWT structural components as the equipment components will be seen to be sufficiently covered by existing empirical databases in Section 2.2.4. Specifically, in order to achieve the overall aims, the following objectives are addressed throughout this thesis:

- To define types of failure that are important for OWT structures through relevant limit states, investigating the structural ULS and FLS;

- To develop a probabilistic risk framework for the ULS using numerical fragility functions, focusing on extreme events and investigating the sensitivity of structural fragility to various modelling and analysis assumptions/strategies;

- To develop a probabilistic, computationally-efficient reliability assessment framework for the FLS. This limit state is particularly important and difficult to assess because it is associated with high computational cost. Additionally, to date, little research has investigated this limit state in a fully probabilistic manner.

- To demonstrate how the proposed fragility/reliability calculation for different limit states can be applied in practice through a series of case-study applications. This will provide an integrated assessment of OWT failure in terms of financial losses, including both the mechanical and structural components. It goes beyond the current state of practice, as most published studies focus on either the structural or mechanical components in isolation.

This thesis focuses on wind farms located in the North Sea and OWTs on monopile foundations, which comprise the majority of currently installed turbines. Intense hurricane and earthquake conditions are not expected in the North Sea and are therefore not the primary focus of this work; however they would be relevant to OWT located in America or Southeast Asia. In the assessment of the ULS an additional site on the USA East Coast is investigated. Additionally, the foundations which support the OWT are included in the analysis of the FLS, but are not included in the explicit uncertainty quantification.

## 1.4 Thesis structure and publications

The research objectives are addressed within the main chapters of this thesis, some of which have been published as stand-alone articles, as summarised in the impact statement:

- Chapter 2 contains the literature review which introduces the concepts of risk and resilience as applied to engineering systems in general. It then focuses on the concepts of risk, reliability and resilience as developed for structural engineering problems and the methods that have been applied specifically to assess offshore wind infrastructure. This is followed by a summary of structural analysis methods used for load-response assessment of OWT and a review of the limit states used in design of OWT. The current literature concerning risk assessment of wind energy is reviewed. A number of gaps present in the existing literature are highlighted, and a methodology addressing these is proposed.

- Chapters 3 and 4 assess OWTs at the ULS, initially proposing a probabilistic risk modelling approach to evaluate the structural risk posed by extreme weather conditions to OWTs in Chapter 3. This approach is based on a Performance Based Engineering (PBE) framework which uses fragility functions to expresses the likelihood of different levels of damage experienced by the OWT structural components over a range of hazard intensities. A closed-form technique, based on a combinatorial system reliability approach, is proposed to assess failure consequences (e.g., financial loss) for a OWT system comprised of both structural and nonstructural components. This is a novel application of fragility functions, which have been widely used for loss estimation of other civil engineering structures, but not OWTs. In Chapter 4, fragility functions are developed for OWTs on monopile foundations exposed to extreme metocean conditions using dynamic aero-elastic simulations. This is done for two case-study locations, one in the USA East Coast and one in the North Sea. The impact of different modelling and analysis choices on

the obtained fragility functions are quantified. Additionally, interdependencies between failure modes for different OWT components are investigated. A coherent treatment of epistemic uncertainties in the definition of fragility functions (e.g., sampling variability in fragility estimation) is implemented using statistical resampling to provide loss results accounting for uncertainty of estimation.

- Chapter 5 and 6 assess OWTs in the FLS. Chapter 5 summarises the problems encountered in FLS assessment and proposes using novel, computationally-efficient GP surrogate model to address these issues. This approach makes it possible to evaluate the large number of load-cases which comprise the operating conditions of an OWT through the use of a surrogate model, surpassing the current state of the art techniques that rely on simplifying the number of load-cases. The surrogate model prediction of fatigue damage is incorporated into a framework for calculating the reliability of an individual OWT including uncertainty in the fatigue material properties. Chapter 6 demonstrates that the proposed approach can reduce the computational effort required to evaluate the FLS through application to three case-study offshore wind farm sites. The sensitivity of various goodness of fit metrics to different model assumptions is investigated in order to further reduce the computational effort required to perform the GP regression. The efficient surrogate model is finally used in a structural reliability calculation to evaluate the probability of failure of an OWT when the fatigue parameters are modelled as random variables, highlighting the large scatter inherent to the fatigue limit state. The full loss calculation, developed for the ULS in Chapter 3, is applied to the FLS, allowing the two limit states to be compared in terms of financial losses.

- The conclusions of the observations arising from the analyses are provided in Chapter 7. This includes a critical review of the results and recommendations for further work.

The chapters of this thesis are developed to be largely self-contained because they have been published as individual journal articles. As such, there is some repetition in introductions and background material. In addition, notational conventions were chosen to be simple and clear for the topic of each chapter rather than for the thesis as a whole; because of this, the notational conventions may not be strictly identical for each chapter.

# Chapter 2

# Literature Review

## 2.1 Introduction

This chapter provides a review of the existing literature regarding probabilistic risk assessment applied to OWTs. The chapter is organised as follows: Section 2.2 provides an overview of risk assessment, describing this in terms of its relationship to resilience, then it summarises specific approaches that have been developed for quantifying risk. Section 2.3 summarises the state-of-the-art for modelling OWT structures, this includes a review of the important limit states to be considered in the assessment. Section 2.4 discusses how these limit states have been utilised in risk modelling studies of OWT structures. Finally, Section 2.5 summarises the research gaps which have been identified and proposes a framework for addressing them. The proposed framework is developed in the main body of the thesis.

## 2.2 Resilience of infrastructure

### 2.2.1 Resilience modelling

The concept of resilience provides a framework in which to assess the behaviour of complex systems over time, particularly after disruptive events which have a large impact on the system functionality. A modern, technical, usage of the term was originally developed within the field of ecology [43]. In this context, resilience measures the magnitude of disturbance that a system can withstand

while its functionality persists. However, the term is now widely applied outside of ecology, across a broad field of disciplines, including [43, 44]: economics, psychology, disaster risk management and engineering (focusing on infrastructure management); and the literature contains many overlapping definitions [44, 43, 45]. The USA Presidential Policy Directive (PPD) 21 [46] provides a useful foundation by stating that "the resilience of a system's function can be measured based on the persistence of a corresponding functional performance under uncertainty in the face of distress". This emphasises the time-dependence of resilience commonly utilised in most definitions [44, 43, 45]. Similar definitions are provided by other institutions and, in the UK, the Civil Contingencies Secretariat of the Cabinet Office defined resilience as: "the ability of a system or organisation to withstand and recover from adversity". The PPD definition is advantageous as, in mentioning uncertainty, it is consistent with the International Standards Organisation (ISO) definition of risk as being the "effect of uncertainties on objectives" [43]. Thereby, this provides a definition that allows risk assessment techniques to be incorporated within a framework for assessing resilience. This definition is also broad, and therefore applicable over a wide range of different infrastructure systems and stakeholders.

In order to assess or develop strategies to enhance resilience, a measure of system performance is necessary; this can be qualitative or quantitative [45]. Qualitative approaches are applicable to community-scale resilience [43]. Quantitative approaches, in contrast, can provide detailed and specific information, useful for optimal decision making for engineering systems. A quantitative approach requires a numerical measure that defines the resilience of the system over time, such as through the mathematical theory of metrics [45]. However, quantitative approaches can also be described schematically through Figure 2.1, often referred to as the resilience triangle [44]. The solid line indicates the system's performance (e.g., for an OWT this might be electricity generation) which is reduced after a disruptive event (e.g., a windstorm) occurring at $t_0$. Performance is gradually recovered along the time axis, to an

"as-new", "at-event", or "deteriorated" performance level. The system operator has different options for making repairs, depending on the desired level of post-event functionality. This behaviour can be described by four attributes which characterise the system [7]:

- Robustness - The capability of the system to withstand a disruptive event. It can be quantified as the residual functionality directly after the event occurs and is therefore a measure of the overall system performance.

- Rapidity - The speed to recover, contain losses, and avoid future disruptions. It can be viewed as the rate of recovery (i.e., the slope of recovery in Figure 2.1), and therefore determines the time gap from $t_0$ to $t_D$, $t_E$ or $t_N$.

- Redundancy - The extent to which other components can satisfy and sustain functional requirements after a disruptive event, which causes a loss of functionality.

- Resourcefulness - The capacity to diagnose and prioritise problems that can cause reduced functionality, then to initiate measures that will lead to functional recovery. This relates to the ability of an organisation to

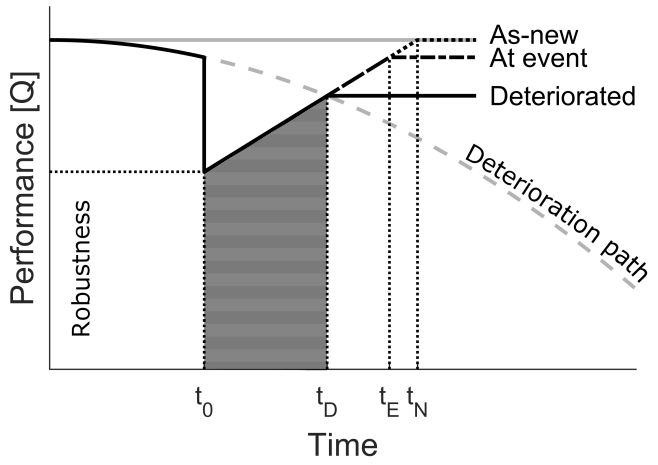


**Figure 2.1:** Graphical definition of resilience after an event (at $t_0$), with different repair options (adapted from [7]).

react after an extreme event has occurred and therefore influences the rapidity.

The focus on functionality over time, in the PPD definition, makes resilience a suitable tool for assessing engineering infrastructure. For example, a full resilience study was conducted to assess recovery strategies for a bridge by Deco et al. [47]. However, this analysis required a large number of details about the bridge and costs incurred when the bridge was unusable (including the financial impact of increased commuting time) to determine which recovery strategy would incur the lowest cost. It would be difficult to apply this type of assessment to all systems, as very detailed information is necessary. This is especially true at the design stage when detailed information about the operational stage is unlikely to be available to the engineer [48]. In the absence of detailed information, resilience may be inferred through the robustness attribute alone, by assuming that resilience and robustness are correlated [49]. This can then be used in a later, full assessment of resilience.

### 2.2.2 Probabilistic risk modelling

Modern risk assessment techniques are based on three distinct elements: hazard, exposure and vulnerability [50]. This approach is consistent with the ISO definition of risk: "the effect of uncertainties on objectives" [43], as each component of the risk assessment is associated with uncertainty. For infrastructure systems, the objective is continued functionality in the presence of natural hazards.

*Hazard* considers the likelihood and extent of a peril. This can be assessed for natural hazards using either empirically recorded data from previous events or physics-based models (e.g., climate prediction in the case of weather-related hazards). Events are defined by their severity and probability of occurrence across a geographical region of interest, e.g., for a hurricane hazard the intensity might be represented using the peak gust wind speed and the extent by the hurricanes footprint. A probabilistic model is necessary to generate event likelihoods, and is commonly evaluated using synthetic catalogues [51]. These

are effectively computational histories in which a long, 10,000 year, time-spans are simulated using a climate model to predict events. The catalogue can then be used to calculate event probabilities for a given Intensity Measure (IM) by counting the number of year in which has an IM above the threshold and dividing by the length of the catalogue.

*Exposure* considers the characteristics of the asset being assessed and its location with respect to the hazard. This comprises information about the asset, including: location, physical construction details, and replacement costs.

*Vulnerability* considers how susceptible the asset is to physical damage from the specific hazard being assessed. The level of damage depends on the severity of the hazard, and so the asset response needs evaluated over the full range of plausible hazard intensities. Additionally, the different performance levels of the asset need to be considered, e.g., for a building it is typical to split the structural performance into various damage states corresponding to no damage, moderate damage, severe damage and collapse thresholds [52].

Finally, some method for communicating the risk to stakeholders is necessary. This is often achieved through a separate loss analysis which estimates the consequence of physical damage in terms of either financial loss, casualties/injury to users or downtime [51]. It provide a series of metrics for communicating performance, including Exceedance Probability (EP) curves which represent the probability of incurring different levels of financial loss for a specific asset or over a region of interest. Integrating the EP curve yields another useful metric in the form of average annual loss for the asset [53].

Two paradigms exist for applying the risk assessment framework to real world engineering systems: PBE and Catastrophe Risk (CAT) modelling. The overall approach used in both is very similar because they rely on combining the different risk assessment components using the theorem of total probability. However, they were both developed independently, and for different purposes, so they will be briefly introduced separately.

PBE was developed within the field of Civil Engineering in the early

2000's, as a development of structural reliability techniques [50]. In the 1960's, previous to PBE, un-calibrated (or calibrated in a simplified way), code-based approaches were used to design and assess structures. These were insufficient as they could not guarantee a consistent level of structural reliability [50]. As a result, new Load Resistance Factored Design (LRFD) structural design codes were developed, with safety factors calibrated using structural reliability techniques; however higher levels of reliability were still necessary for critical buildings. Consequently, nuclear power stations and important buildings, which were exposed to highly uncertain earthquake hazards, were the focus of the first PBE applications [8]. The framework was subsequently extended to encompass a wide variety of natural hazards, including: blast [48], wind [54, 55] and tsunami hazards [56, 57]. PBE is typically applied to single structures as either a tool to improve design or select improved maintenance and retrofitting strategies for existing ones [58]. The general approach is described through the equation [59]:

$$\lambda(DV) = \iiint F(DV|DM)|f(DM|EDP)||f(EDP|IM)||d\lambda(IM)|, \qquad (2.1)$$

in which the total probability theory has been applied to decompose the mean annual frequency of occurrence, $\lambda(\cdot)$, of a Decision Variable (DV) into the components of risk assessment. $F(\cdot|\cdot)$ is a conditional Cumulative Distribution Function (CDF) and $f(\cdot|\cdot)$ is a conditional Probability Density Function (PDF). The variables within these functions are:

- IM, a quantity that indicates the severity of the hazard at a given site. It acts as an interface between the natural hazard and the structure, e.g., wind hazard might be represented through the mean wind speed.
- Engineering Design Parameter (EDP), an engineering design parameter describes the structural response to the hazard, e.g., by computing the stress in a component.

- Damage Measure (DM) describes the physical damage to the structure. This is defined in terms of a limit state, which sets EDP thresholds above which a certain level of damage will occur.

- DV represents the performance objectives of the system being assessed, such as: casualties, monetary loss or downtime.

The full framework is compiled by integrating each term in Eq.(2.1). The approach can also be described using the flowchart shown in Figure 2.2 and relates to the components of risk assessment:

- Hazard - Model representing the frequency of occurrence of the parameters selected as the $IM$. In Eq. (2.1), it is represented through the annual rate of occurrence of the IM, the term $\lambda(IM)$.

- Loss - A conditional distribution of the losses for different damage levels $DM$, captured through the term $F(DV|DM)$.

- Vulnerability - A distribution of the total loss or loss ratio (repair cost over replacement cost) with respect to the IM. The fragility function is a closely related concept which defines a structure's susceptibility to damage in terms of probability of a limit state being exceeded across the full range of hazard intensity (IM). These typically are expressed as a CDF, which can be extracted from Eq. (2.1) by integrating over the EDP variable, yielding the term $|f(DM|IM)|$, and converting it to a

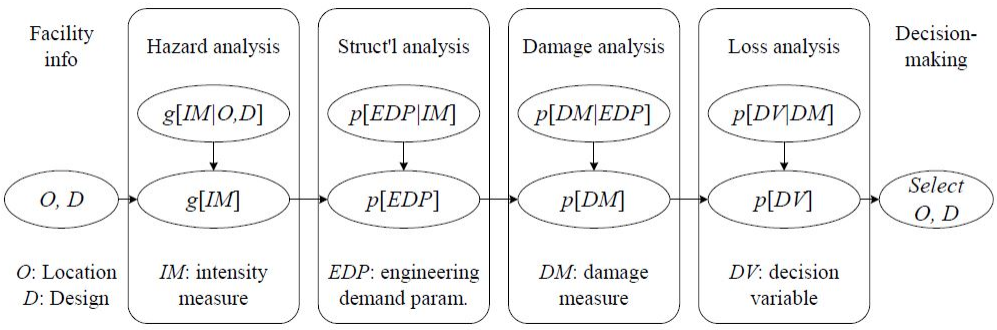


**Figure 2.2:** PBE risk modelling framework, taken from [8].

CDF $F(DM|IM)$. Fragility functions combine the structural analysis and damage analysis component in Figure 2.2, and allow uncertainty in structural capacity (e.g., geometry, material properties, models) to be captured. The vulnerability function is evaluated by combining damage-to-loss models and fragility functions, resulting in a distribution of loss conditional on the hazard intensity $F(DV|IM)$ .

CAT modelling uses the same approach as PBE for combining the risk assessment components. However, it operates on a different scale, predicting losses over large geographical regions, instead of for specific assets. This approach was developed within the insurance industry in the 1980's [51], as the previous method of manually recording insurance claims on maps was cumbersome and inaccurate for rare, catastrophic events, with a sparse historical record. CAT modelling was based on newly developed scientific understanding and modelling techniques which used computational platforms to predict the occurrence of natural hazards [51]. This allowed risk assessment to be carried out for large portfolios of assets, using the general structure shown in Figure 2.3. All the components of a CAT model are similar, and are combined in the same way, as PBE. However, as these models can operate at a regional scale, there are differences with the PBE approach [58]. A key one for this work, is that vulnerability is defined over a large series of structures which are taken as representative of the building stock in the region, not for each individual structure [51].

Both PBE and CAT models are suitable for modelling the response of infrastructure to extreme events. However, because they rely on decomposing the risk assessment problem, specifically between the hazard and fragility / vulnerability, it is difficult to include deterioration mechanisms which effect the structure over time within the standard framework. These mechanisms include corrosion and fatigue, and can be analysed using explicitly time-dependent life-cycle techniques [60].

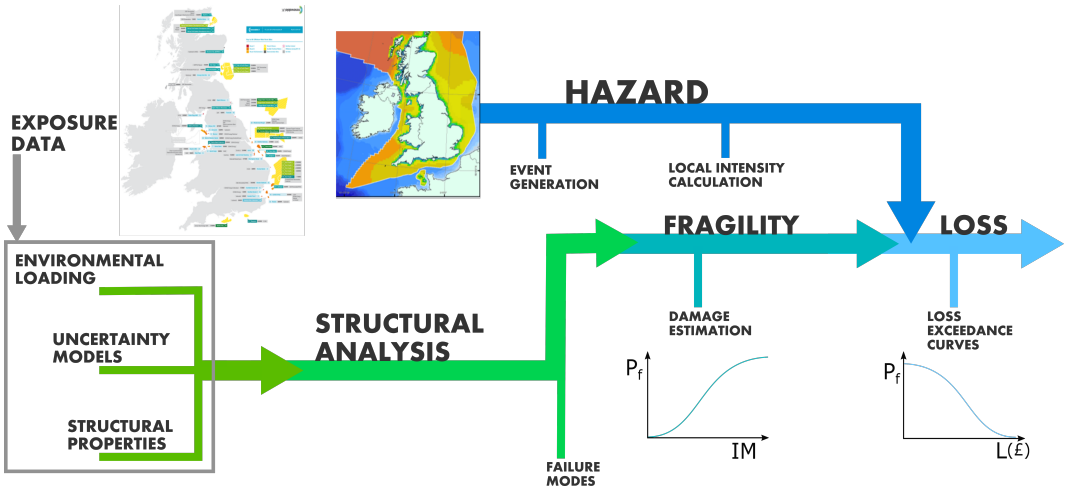


**Figure 2.3:** CAT risk framework for a wind hazard.

### 2.2.3 Fragility evaluation techniques

Fragility functions describe the susceptibility of a structure or structural element to damage [61]. This is expressed through a probability valued function that represents the probability of exceeding the structures capacity at a given level of hazard intensity for a single damage state [59], i.e., $F(DM|IM)$ as introduced in the previous section. Consequently, fragility functions sit in the middle of the risk assessment process, and act as an interface between the environmental conditions and the prediction of damage.

A wide range of techniques have been developed for producing fragility functions within both PBE and CAT modelling frameworks [61]. Data from historical, recorded events can be used to define fragility functions empirically. This is a purely data-driven approach where statistical techniques are used to estimate damage probabilities [62]. Empirical approaches are regarded as the most reliable source of damage statistics as they are based on real-world observations [52]. They may be more useful in a CAT modelling context, because they rely on averaging damage over a set of recorded data (typically from buildings with a range of characteristics) [62]. However, an empirical approach depends on high quality information from previous events. If detailed information is unavailable, expert judgement can be used as an alternative method for producing fragility functions. However, the reliability of expert judgement

is questionable because it depends on the experience of the experts who are consulted. A different approach driven by the problems inherent in expert judgement and the scarcity of empirical data is based on generating fragility functions numerically [63]. This relies on mathematical models to represent the behaviour of a building, or series of representative (index) buildings under different levels of hazard intensity [59]. However, the disadvantage is that this approach requires detailed information in order to define a sufficiently accurate structural model. Any of these approaches can be combined using hybrid fragility techniques which attempt to compensate for the drawbacks of individual approaches [61].

Structural reliability techniques can be thought of as predicting a single point from an analytical fragility function. Indeed these techniques originated for use in first generation of calibrated LRFD codes [50] for predicting the probability of failure of a single code limit state, i.e., a single hazard-intensity level. Reliability problems are often posed in terms of a response variable, $Y$, exceeding a specified performance threshold $b$, where the response is predicted using a set of input variables, $\mathbf{X}$, which are converted through a relationship ($h(\cdot)$):

$$Y = h(\mathbf{X}). \tag{2.2}$$

Reliability estimation is the process of evaluating how likely failure is to occur when the value of the input variables are uncertain (and can be modelled as a joint-PDF). The probability of failure is the probability of exceeding the performance threshold $P(Y > b)$. The reliability is then $P(Y \leq b) = 1 - P(Y > b)$, which can also be evaluated as an integral of the joint-PDF of the input variables ($q(\mathbf{x})$) over the parameter space in which failure occurs ($F$) [9]:

$$P(Y > b) = \int_F q(\mathbf{x}) d\mathbf{x} = \int I_F(\mathbf{x}) q(\mathbf{x}) d\mathbf{x} = \mathbb{E}[I_F(\mathbf{x})]. \tag{2.3}$$

$I_F(\mathbf{x})$ is an indicator function that takes the value of 1 when $\mathbf{x}$ is in its

failure space. The boundary between system failure and safety is defined using a limit state equation ($G(\cdot)$), which encodes the desired performance objectives for the system:

$$G(\mathbf{x}) = b - h(\mathbf{x}). \tag{2.4}$$

A large number of input random variables are typically used in modern reliability simulation and mean that it can be difficult to visualise the integral in Eq. (2.3). However, a simplified problem which has two random variables can be observed, such as shown on Figure 2.4 (left). Depending on the function that relates $Y$ to $\mathbf{X}$ the failure region can be a complex shape, with a non-linear boundary separating the failure and non-failure regions. The design point is defined as the point on the failure boundary that is nearest to the origin, and is highlighted with the symbol $\mathbf{x}^*$ in Figure 2.4 (left).

One early method referred to as the First Order Reliability Method (FORM) [64] simplifies the failure boundary by assuming it takes the form of a linear relationship, as shown on Figure 2.4 (right) providing an analytical solution. The approach is based on firstly transforming the joint-PDF of $\mathbf{X}$ into a multivariate standard Gaussian distribution; this transformed version of

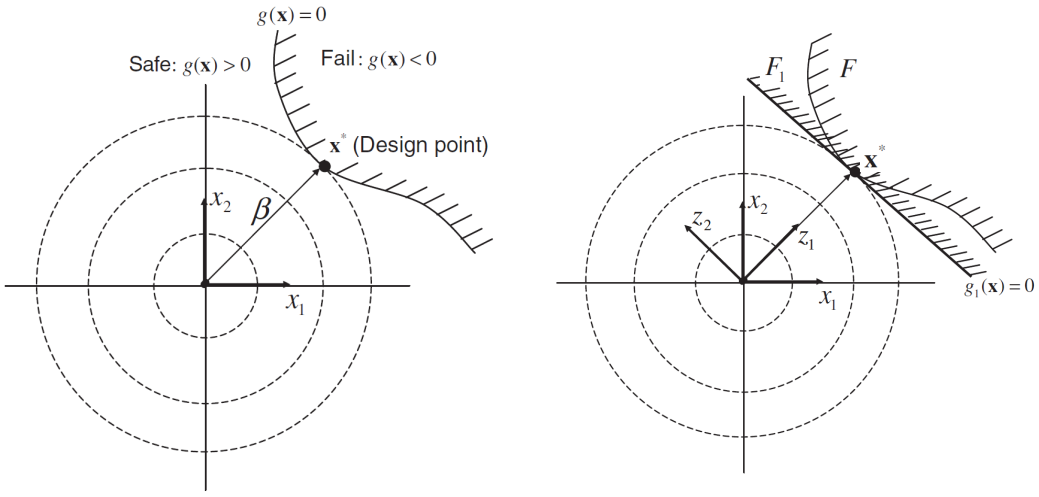


**Figure 2.4:** Failure space for a system with two random variables, each of which follows a standard Gaussian distributions (left). The complex failure surface is simplified to a linear relationship (right). Taken from [9].

the reliability problem is plotted in Figure 2.4 (right). Numerical optimisation is used to locate the design point and the distance of this point from the origin is denoted $\beta$, the reliability index. The probability of failure can be estimated by simply evaluating the CDF of $-\beta$, as the Gaussian PDF is axisymmetric.

A separate family of techniques for structural reliability assessment are based on sampling. The most widely used approach is plain Monte Carlo simulation [64] which relies on the observation that probability of failure can be viewed as an expectation (as indicated in Eq. (2.3)), and can be calculated by statistical averaging [9]. Realisations of $\mathbf{X}$ are sampled and the system response $Y$ corresponding to each is evaluated. The probability of failure is then the average over responses where the system exceeds it's performance threshold, when Eq. (2.4) is less than zero. However, because of it's reliance on averaging, Monte Carlo simulation requires a large number of samples to evaluate small probabilities of failure. This can be computationally demanding if the relationship between $\mathbf{X}$ and $Y$ is complicated, e.g, evaluated through Finite Element Analysis (FEA). Consequently modifications have been developed that either attempt to improve sampling efficiency (importance sampling, subset simulation) or the Monte Carlo technique is combined with others, such as response surfaces, to improve the sampling speed [64].

Surrogate models are another family of methods used in structural reliability assessment, and which also have a much larger field of application. These replace the limit state with an approximation which is less computationally expensive to evaluate. Typically this approximation is a mathematical function that does not contain any physics from the limit state (e.g., a finite element model) [65]. These models are typically calibrated to the limit state by analysing the physics-based model at a discrete number of locations, then using an optimisation algorithm to find he parameters of the surrogate model which represent the limit state data best. The locations used to calibrate the surrogate model are selected using a design of experiment method such as: random sampling, Latin Hypercube sampling or other space filling algorithms

[66]. In the field of structural reliability analysis surrogate models based on polynomials are referred to as "response surfaces" [64], where the polynomial represents the limit state function:

$$\hat{Y} = \hat{h}(\mathbf{X}) \tag{2.5}$$

This approximation of the limit state ($\hat{h}(\cdot)$) can be rapidly evaluated, and, for example be used to draw a large number of samples with a Monte Carlo simulation.

### 2.2.4 Risk modelling of offshore wind turbines

Full resilience studies specifically focusing on OWTs are rare. Indeed, a search of the Scopus abstract and citation database on 24/04/19 using keywords: offshore, wind turbine, and resilience identified only two studies. The first was a qualitative assessment of human error and organisational capacity, Mentes and Turan [67], which is not relevant to the aims of this thesis. The second paper, Feng et al. [68], proposed using series and parallel relationships to quantify the system resilience of OWFs. However, this study only used OWFs as an illustrative application of a general approach for evaluating resilience, and did not investigate the failure of OWTs in detail. It completely neglected the OWT structure and evaluated the reliability of OWT components using existing empirical data. This study was focused on estimating resilience, in terms of spare repair capacity, and not economic loss. It therefore neglected a key element of OWF decision making.

Instead of resilience most literature has focused on characterising the reliability of different wind turbine components, either: empirically, using databases of recorded failures, or analytically, using mechanical models to simulate the behaviour of the component/system over its operating life. Empirical reliability analyses of the wind turbines and OWTs have tended to focus on the mechanical components. Studies on onshore wind turbines have consistently highlighted that the blades and drive-train components have a large

influence on reliability [69, 70, 71, 72], but have often neglected the structural components. Additionally, these studies have focused on failure rates and down-time, as opposed to financial losses resulting from failure of the different sub-systems. OWTs were assessed using empirical data by Delorm et al. [73] using reliability block diagrams. However, this study only focused on failure rates and didn't include structural components. A similar study by Lazakis et al. [74] used generic failure rates from an offshore Oil and Gas handbook for the OWT components, but highlighted the importance of structural failure in terms of life-safety and operations performance metrics. Data from real world OWT operators was analysed by Carroll et al. [10] across $\sim 350$ OWTs and included financial losses for different component failures. The results are shown on Figure 2.5 in terms of failure rates for different components. This study is a useful comparison to other empirical studies as it included many large utility scale OWTs. It confirmed the importance of the drive-train components and blades, however did not include major replacement of the structural components. It also confirmed the relationship between increasing mean wind speed and increased component failure rate observed for onshore wind turbines by Ferrari et al. [69].

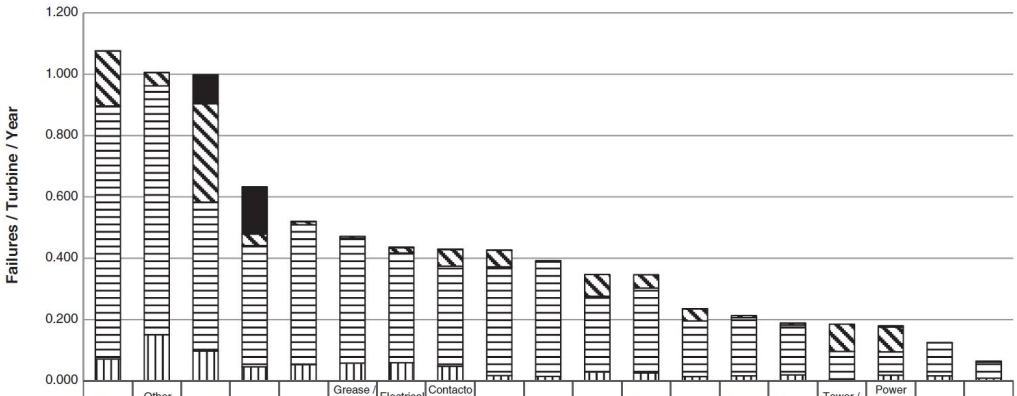


| | Pitch / Hyd | Other Components | Generator | Gearbox | Blades | Grease / Oil / Cooling Liq. | Electrical Components | Contactor / Circuit Breaker / Relay | Controls | Safety | Sensors | Pumps/ Motors | Hub | Heaters / Coolers | Yaw System | Tower / Foundation | Power Supply / Converter | Service Items | Transformer |
|---|---|---|---|---|---|---|---|---|---|---|---|---|---|---|---|---|---|---|---|
| Major Replacement | 0.001 | 0.001 | 0.095 | 0.154 | 0.001 | 0.000 | 0.002 | 0.002 | 0.001 | 0.000 | 0.000 | 0.000 | 0.001 | 0.000 | 0.001 | 0.000 | 0.005 | 0.000 | 0.001 |
| Major Repair | 0.179 | 0.042 | 0.321 | 0.038 | 0.010 | 0.006 | 0.016 | 0.054 | 0.054 | 0.004 | 0.070 | 0.043 | 0.038 | 0.007 | 0.006 | 0.089 | 0.081 | 0.001 | 0.003 |
| Minor Repair | 0.824 | 0.812 | 0.485 | 0.395 | 0.456 | 0.407 | 0.358 | 0.326 | 0.355 | 0.373 | 0.247 | 0.278 | 0.182 | 0.190 | 0.162 | 0.092 | 0.076 | 0.108 | 0.052 |
| No Cost Data | 0.072 | 0.150 | 0.098 | 0.046 | 0.053 | 0.058 | 0.059 | 0.048 | 0.018 | 0.015 | 0.029 | 0.025 | 0.014 | 0.016 | 0.020 | 0.004 | 0.018 | 0.016 | 0.009 |

**Figure 2.5:** Failure rates observed for different owt sub-assemblies, taken from Carroll et al. [10].

The analytical reliability analysis of OWTs has been summarised in two comprehensive literature reviews. Leimeister and Kolios [75] reviewed qualitative and quantitative approaches applied to all components of offshore wind installations. The qualitative approaches, include techniques such as fault tree diagrams, events tree diagrams and Bayesian belief networks, which can be transformed into quantitative approaches by weighting the component failure branches by a probability of occurrence. These approaches were used when there was insufficient detailed information about the system to allow a fully quantitative assessment. The quantitative approaches were found to provide a detailed assessment of reliability and were typically more sophisticated than qualitative approaches, at the cost of requiring detailed information about the system. This category includes a wide variety of analytical methods based on mechanics-based simulation, which was the focus of the review by Jiang et al. [76]. Most studies focusing on OWT structural components evaluate reliability using an analytical approach because few failures have been observed. Consequently, studies investigating OWT structural reliability investigate different analytical limit states depending on the type of failure being modelled. Two important analytical limit states for structural reliability, the ULS and FLS, are reviewed in Section 2.3. Then approaches to reliability analysis are described in Section 2.4.

## 2.3 Structural assessment of offshore wind turbines

### 2.3.1 Structural analysis methods

OWTs are designed to withstand environmental loading over a 20-25 year design life. This requires precise assessment of the OWTs dynamic behaviour in order to analyse the full range of conditions which it will experienced accurately. The current state-of-the-art for structural design is assessment based on integrated time-history analysis [39]. This approach enables modelling of dynamic coupling, which is important to predict structural response, including:

aerodynamic damping, changing blade pitch with wind speed and non-linear dynamic properties of the blades (such as stiffness changes caused by centrifugal forces).

Integrated, time-domain analysis of OWTs is based on evaluation of the structures reaction to simulated time-series of environmental loading. The OWT model typically includes the full support structure, blades, drive-train and the control system. The motion of these components is integrated through coupled equations of motion, and solved using a time stepping algorithm [77]. It is necessary for the time-step used by this algorithm to be small to prevent numerical instabilities. Consequently, time-domain simulation is associated with a large computational cost. This is magnified by the need to assess a large number of design situations, referred to as Design Load Case (DLC), see Section 2.3.2 and 2.3.3 for details of ULS and FLS assessment respectively. Specialised, fully coupled aero-hydro-servo-elastic software packages exist that allow this type of analysis including: FAST [77], Bladed, HAWC2 and 3DFloat. FAST is often used in academic research as it is open-source and has been validated against the other commercial aero-hydro-servo-elastic software packages [78]. Other, more computationally efficient, methods exist for analysis of OWTs, but they are not commonly used in detailed structural design [11]. For example, decoupled time-domain simulation applies wind and wave loading independently and superimposes the resulting decoupled response. However, this approach has been shown to be inaccurate for jacket structures [79]. Similarly, frequency domain methods are computationally efficient [80] but are not commonly used in the detailed design phase of OWTs as they cannot model the non-linearities which are important to the structural response. Additionally, both of these approaches require careful consideration of the aero-dynamic damping to avoid large over-predictions of the OWT's response [81].

Wind and wave conditions are the main external loads on OWTs and both naturally vary over time. In computational simulation both processes are split into long- and short-term components. For wind loading this is justified

through observations of the wind spectrum where a trough in the spectral energy can be observed between the Diurnal (daily) and Turbulent (one minute) frequencies, van der Hoven [12] and illustrated in Figure 2.6. This is a natural point at which to split the loading between variation modelled internally within the simulation and externally. A similar justification is used for separating waves into long- and short-term components. In both cases, long-term variation is modelled statistically by running different computer simulations with changing input conditions. Short-term variations are assessed within the simulation by using stochastic environmental models which generate loads rapidly changing within a time-series [39].

Short-term wind conditions are typically comprised of a mean and turbulent component [13]. These are computed independently and summed to produce a wind speed time-series. The mean component is static during the simulation, but varies with increasing height from the Mean Sea Level (MSL) as shown on Figure 2.7 and modelled mathematically using a logarithmic or power rule [13]. Wind turbulence is defined through an energy spectrum and converted into a time-domain signal using Fourier transforms. The Kaimal spectrum is a common choice, and recommended in the wind turbine design

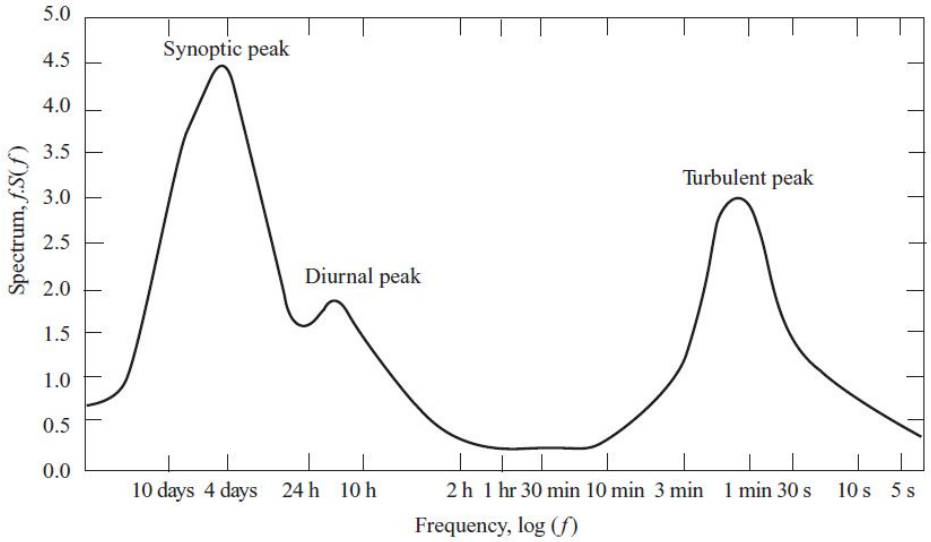


**Figure 2.6:** Wind spectrum taken from Burton [11], based on measurements from van der Hoven [12].

codes [6]. This calculation is carried out for a grid of points that overlay the wind turbine rotor, with correlation between the spatially close points enforced using an exponential coherence model [6]. Turbulence at the grid locations is superimposed over the constant mean wind profile [39]. This produces a wind speed time-series for each grid point which can be used to calculate forces in the main structural calculation.

Linear wave kinematics are frequently modelled in OWF design as varying stochastically. The wave height is modelled through a frequency domain energy spectrum which is converted into a time-domain signal using Fourier transforms. Then water particle kinematics (position, velocities, accelerations) are evaluated using a wave theory, linear Airy waves are a common choice [82]. This model neglects higher-order, non-linear, effects that occur when waves near their breaking limit [83], but has been found to be sufficient for small waves that occur during normal conditions [84]. The wave kinematics are converted into forces using Morrison's equation [82] and used in the main structural calculation.

OWTs are slender structures which respond to wind and wave loading dynamically. For instance, every blade passes the tower once during each revolution of the rotor, this momentarily shields the tower from wind load,

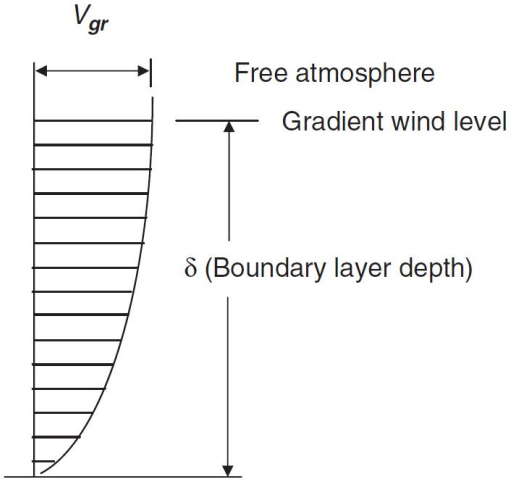


**Figure 2.7:** Mean wind profile, showing wind speed ($V_{gr}$) changing with height over the atmospheric boundary layer, taken from Simiu [13].

creating an excitation at a frequency referred to as the 3P frequency [15] (as it is three times the rotor frequency). Similarly, an unbalanced cyclic force acts on the tower each revolution of the rotor as a result of mass imbalances in the rotor, referred to as the 1P frequency [15]. These properties depend on the rotational speed of the rotor, which changes with the mean wind speed, and so the 1P and 3P frequency cover a range of frequencies [11]. They are important in design of OWTs as the structure will resonate during normal operation if its natural frequency falls within the 1P or 3P bands. For OWTs on fixed foundations it is common to select a natural frequency which falls between the 1P and 3P band [38], sometimes referred to as soft-stiff design. Additionally, the main energy content of wind and wave loading typically occurs at frequencies below or overlapping the 1P frequency band. These bands can be visualised using a Campbell diagram, Figure 2.8 for the National Renewable Energy Laboratory (NREL) 5MW OWT [42] (a common OWT model used in academic research), which shows the safe natural frequency limits for the turbine.

However, the gap between the 1P and 3P bands is commonly narrow, falling between between 0.22Hz and 0.32Hz for the NREL 5MW OWT on fixed foundations [14] or non-existent for some other OWT structures [15], see Figure

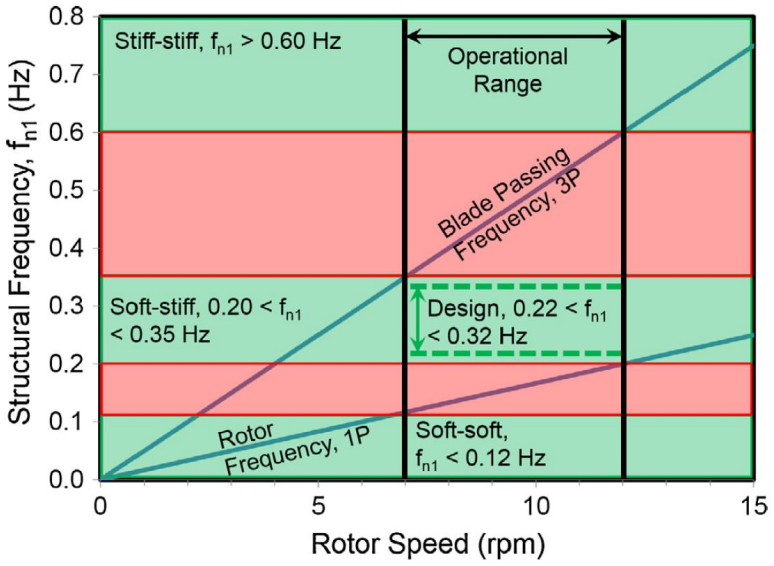


**Figure 2.8:** Campbell diagram for the NREL 5MW OWT, taken from [14].

2.9. Therefore accurate prediction of the OWTs natural frequency is vital in order to select an appropriate structural stiffness. The natural frequency is effected by the dynamic properties of the rotor (e.g., centrifugal stiffening), the support structure and the foundation. The first two items are modelled in the current generation of aero-hydro-servo-elastic software packages, including FAST [77]. However, these software packages do not currently include tools for detailed assessment of the OWT foundations, which are vital to the dynamic response [85].

Another important dynamic feature is damping, which removes energy from vibration of the OWTs structure, reducing the amplitude of the response at resonant peaks and therefore reducing structural motion. Damping is commonly split into components which are caused by different sources, including: aerodynamic, hydrodynamic, structural and soil. Aerodynamic damping is caused by the drag generated as the rotating blades oscillate due to motion of the RNA. It has a large impact, particularly on the fore-aft motion of an operating rotor, but little influence on the side-to-side motion and when the turbine is parked [86]. Aerodynamic damping is non-linear with changing wind speed [81] as the wind turbine controller alters thrust forces and therefore motion of the RNA. One reason for preferring aero-elastic (time-domain)

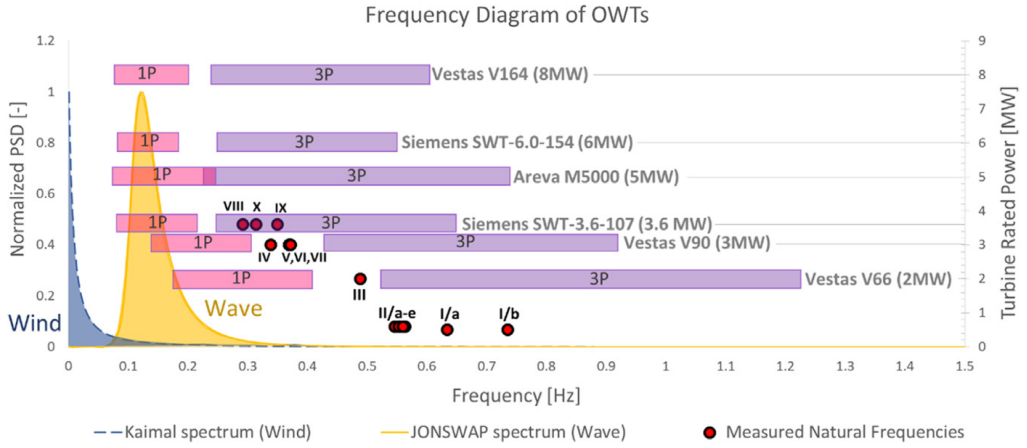


**Figure 2.9:** Comparison of 1P and 3P frequencies for a series of different OWTs [15].

simulation is that aerodynamic damping is implicitly evaluated. Soil damping is a consequence of motion of the pile and hysteretic material damping (as soil behaves non-linearly). It has been found to be important for parked OWTs [87]. Structural damping is low for steel structures, but the presence of a grouted connection at the transition piece may introduce higher levels of damping [88]. Hydrodynamic damping is caused by motion of water around the sub-structure and has been found to be of minimal importance [86].

In design of OWTs, analysis of monopile foundations is commonly based on discrete spring models that utilise p-y curves [87]. These are an intuitive approach and define a force displacement relationship along the pile, but have a number of well-known limitations [87]. For example, it is common to simplify the non-linear p-y curves to a linear relationship, but soil behaves non-linearly. Additionally, the standard p-y implementation does not include foundation damping. Selecting spring stiffness is also problematic, with the code-based approach (used for offshore Oil and Gas piles) too have been found to be too soft. A wide variety of other foundation models exist, with different levels of computational complexity and empirical verification [89]. Recent work has emphasised the importance of correctly replicating the stiffness and damping of the foundation in order to reproduce measured OWT response during idling conditions [89]. However the contribution of foundation damping to the overall damping is smaller for operational load cases due to the presence of high aerodynamic damping [86] and the load cases drive fatigue loading [90].

### 2.3.2 Ultimate limit state

The ULS considers failure of OWT as a result of overload. Failure modes in this limit state can include yielding or buckling, as specified by Det Norske Veritas Germanischer Lloyd (DNVGL) [91]. The DNVGL-ST-0126 design code requires checks against all of these failure modes to be conducted for steel structures. However, the bucking check is particularly important as the tower and sometimes monopile typically have a large diameter to wall thickness ratio [92] which makes them susceptible to this failure mode. Additionally the tower

includes a door which can act as a reduce the strength of the lower portion of the tower and initiate the buckle [93].

When assessing the ULS, the OWT design code IEC 61400-3 [6] works in parallel with the onshore wind turbine design code IEC 61400-1 [94], adding provisions specific to OWTs, such as wave loading [11]. These standards employ the LRFD approach to specify a certain safety level in structural components. They incorporate uncertainties in a conservative way, by employing safety factors, to ensure a structural component (and therefore it is assumed structural system) does not fail with a frequency greater than a pre-defined target threshold. The safety factors account for structural demand- and capacity-affecting uncertainties by magnifying loads, and thereby ensure 'safe' designs. In the current generation of design codes these are a combination the factors used in the offshore Oil and Gas industry and for onshore wind turbines. The factors are provided to mitigate against both aleatory uncertainties, associated with the calculation of an OWTs structural capacity (e.g., geometry, materials), and epistemic uncertainties, due to modelling and analysis assumptions. Currently, code based design uses the uncalibrated partial safety factors as a way for dealing with these uncertainties [95]. However, the unknown calibration of these factors, when considering the actual risk profile of an OWT, could produce design solutions that are either too conservative, and not cost-effective, or unsafe, leading to potentially catastrophic losses such as those that would be caused by a large numbers of cascading failures in an OWF. Indeed, this is the situation, meaning that implied reliability levels are unclear, and not intelligible to the engineers who design OWTs.

The IEC design code [6] captures the different situations that might lead to overload by specifying a wide range of environmental conditions, each of which needs to be assessed independently. These are specified through a set of DLC which aim to model the full range of conditions an OWT will experience during it's life, including loads occurring during installation. Each DLC has a partial safety factor that multiplies the maximum load to account for uncertainty in

load calculation. However, the specification of a structural capacity necessary to resist loads determined by the DLC is left to existing, recognised offshore standards (with their own material factors). The choice of code depends on the type of sub-structure is being designed. The DLCs contain a range of situations which fall into three broad categories [96, 11]:

- Normal operating environmental conditions with loads extrapolated to 50-year return period values.
- Extreme operating environmental conditions which have a 50-year return period.
- Loads resulting from transient conditions or faults with the control system.

The latter set of DLC are transient conditions (such as sudden wind changes or yaw misalignment resulting from a loss of power to the control system) which are highly dependent on the OWT specific control system. For the NREL 5MW archetype OWT they were found not to drive maximum loads in the structural components [95]. In contrast the extrapolated 50-year loads were found to cause largest seabed moments, an indicator of ULS importance for the sub-structure, when the NREL 5MW OWT was assessed at the Ijmuiden wind farm site in the Dutch North Sea. The rotor is operational during this set of DLC as they assess the full range of normal operating conditions. The resulting load time series are post-processed to evaluate the 50-year return period load of the normal operating condition (which do not consider the probability that the environmental conditions will occur). The most severe DLC in this category assessed operational wind speeds while applying the maximum 50-year return period wave height (independent of the wind speed). This means that the 50-year Mean Return Period (MRP) significant wave height is coincident with the rated wind speed, the wind speed which produces the highest loads. This is an unrealistic scenario as, in reality, the wind speed and significant wave height are correlated, with larger wave heights tending

to occur during higher wind speeds. The 50-year return period environmental conditions were also found to result in large loads [95], generated using the site joint probability distribution for mean wind speed and wave height (with other environmental conditions selected using deterministic code parameters). Hubler et al. [96] found that assessing the ULS using a fully probabilistic approach resulted in larger ULS loads than the deterministic DLC for the 50-year return period. This method was developed by sampling environmental conditions directly from site joint probability distribution function (PDF), avoiding the determinism of the code DLC.

Both IEC [6] and DNVGL [91] standards specify ULS DLC characterized by an upper limit of 50-year MRP wind and wave conditions. The probability of exceedence for this MRP is 33% over a 20-year design life. This is substantially lower than the maximum MRP of 10,000 years used in LRFD codes to assess offshore Oil and Gas structures [97, 98]. In other words, the current design procedure appears to neglect rare, but severe, storm conditions characterized by higher MRP, such as the typhoon conditions which have been observed to cause failure in onshore wind turbines [99].

### 2.3.3 Fatigue limit state

During an OWTs operational life it experiences a large number of load cycles from stochastic environmental loading and cyclic actions of the rotor at the 1P and 3P frequencies [39]. The consequence of these load cycles is that small cracks develop from weak points in the structure, such as welded joints or areas with high stress concentrations. Over time they can grow to threaten the structural integrity of the OWT. This process is cumulative as load cycles sequentially contribute to the crack initiation or growth, and is captured in design of OWTs through evaluation of the FLS. To assess fatigue, the full load spectrum acting on the OWT over it's operating life needs to be considered. However, this is a complex task as it must encompass situations where the OWT is operating, parked (due to low/high wind speeds or is under maintenance) and operating under transient conditions (such as during start-up)

[11].

All structural components are exposed to fatigue, especially the welds which join the monopile and tower [16]. Welds are particularly vulnerable because small flaws (in the form on inclusions or voids) are introduced to the structure as the joint solidifies, providing an initiation point from which cracks can grow [16]. The base of the monopile is frequently the focus of analysis as it experiences the largest bending moments. Additionally the rotating drive train components are exposed to fatigue as they turn during power production.

The approach taken in the OWT design code (IEC 61400-3 [6]) to assessment of the FLS is similar to that taken for the ULS. A series of DLC are defined, with each assessed independently. They span the full range of scenarios that it is expected the OWT will encounter, including: power production (i.e., operating), fault, parked and shut-down each with differing assumptions about the environmental conditions. However, the focus of research has been on DLC 1.2 which assesses damage accumulated while an OWT is producing power [90]. The FLS is computed by splitting the continuous range of wind speeds at which the OWT is operational into a series of discrete bins. For each wind speed bin the wind and wave parameters are also discretized using a table that contains different combinations of the wave parameters (often referred to as a scatter chart). Each combination of environmental conditions is evaluated independently using time-history structural analysis to produce a load spectrum. A combined load spectrum over the entire OWT design life is evaluated by weighting the damage caused by each set of environmental conditions by the length of time they are predicted to persist during the OWT design life [11]. This extrapolates the short interval over which the structural loads are evaluated to the design life of the OWT.

The design code for OWTs, IEC 61400-3 [6], recommends either using a certified fatigue design code or partial safety factors from the onshore code IEC 61400-1 if one is unavailable. The external fatigue design code is stipulated to use combined (load, material and consequence of failure) partial safety factors

no less than in those IEC 61400-1. For a fatigue design code that uses 99.7% probability of survival fatigue design curves the partial safety factor is 1.1 on structural stresses. The commonly used fatigue design code DNVGL-RP-C203 contains these fatigue design curves for offshore structures. It does not employ partial safety factors but specifies using design fatigue factors which are integers greater than one and less than 10, which scale the design curve. They are selected by the designer depending on the ability of the structure to be inspected for fatigue cracks during service.

In structural design based on time-history simulation, fatigue loads need extracted from load time-histories produced for all components. This is done through the DNVGL design code [100] using either:

- The Stress Life (SN) approach - where the fatigue crack is implicitly modelled. Stresses are extracted from the global structural analysis model and the development of the crack is assessed using data from laboratory experiments on small test specimen.

- Fracture mechanics - where loads from a global structural analysis are used to explicitly model the growth of a fatigue crack, either through a series of equations (using Paris' law) or a detailed structural FEA model. In this approach, the crack length can be predicted at any point during the structures life.

The stress life approach is most frequently used in structural design as it is simple to implement. Fatigue loads are assessed using an SN curve (or design curve) which records the number of tolerable cycles against the corresponding constant amplitude stress range, as shown in Figure 2.10. Loading from dynamic time-history analysis has a variable amplitude and is segmented into individual load cycles using the rainflow counting algorithm [101]. Then the fatigue damage caused by the each individual stress cycle is calculated using linear damage accumulation (also referred to as Miner's Law). This method is linear and so the ordering of fatigue loads do not matter, i.e., a large stress

cycle followed by a small cycle causes the same damage as a small stress cycle followed by a large one.

Fracture mechanics explicitly models the development of the fatigue crack and can include the effects of order on fatigue damage, e.g., a stress cycle of equivalent magnitude will cause a larger growth in the crack length if it occurs after a series of damaging stress cycles. However, it is not commonly used in design assessment of OWTs, as load order was found to have little effect on the overall fatigue life [102]. Additionally, fracture mechanics requires selection of material properties which govern crack growth and aren't available for all materials [16]. One solution involves calibrating these factors so that the fatigue life matches that predicted using the SN method [102]. However, this means the only advantage of fracture mechanics over the SN approach lies in knowing the crack length over time, as the predicted fatigue life will be equal in both methods.

Discretisation of the environmental conditions is important for modelling fatigue damage accurately, as it effects the fidelity at which the loads on the turbine are evaluated. The mean wind speed is commonly split into 2m/s wide discrete bins which span the operating wind speeds of the OWT. The blade

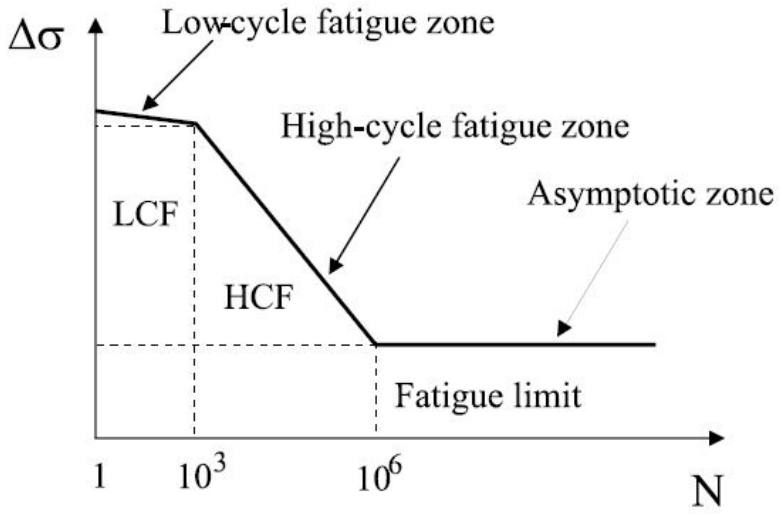


**Figure 2.10:** Example SN curve for a steel material, taken from Schijve [16]. The stress amplitude is denoted $S_a$ and the number of cycles $\Delta\sigma$.

controller behaves non-linearly with changing mean wind speed, and fatigue loads typically increase until the rated wind speed is reached then reduce afterwards. Large wind speed bins need to be selected carefully to ensure the peak mean wind speed for fatigue loading is properly captured. Furthermore, a single value of turbulence intensity is commonly defined for each mean wind speed, whereas in reality a distribution of values are encountered during the design life. Additionally, for each mean wind speed bin, the standard recommends using a conditional PDF to model the wave conditions [6]. However this leads to a large number of analyses, more that 50,000 may be required for evaluating DLC 1.2 [39] resulting in large computing times. The mean wind and wave parameters are commonly combined into a single set of values [103] to reduce the number of simulations (and the overall computational time). An early study suggested that this caused only few percent error in the predicted lifetime fatigue damage [11]. However, more recent verification against measurements from instrumented OWTs indicate that this low-fidelity discretisation underestimates the variability in fatigue loading [104]. Fully probabilistic environmental conditions capture these loads better [96] but are computationally expensive to evaluate.

## 2.4 Reliability assessment of wind turbines

### 2.4.1 Ultimate limit state reliability

A wide range of techniques for reliability analysis have been applied to assess the structural ULS of OWTs, some of which have worked within the probabilistic risk frameworks described in Section 2.2.1.

An early investigation into the ULS reliability of onshore wind turbines, Sørensen and Toft [105], developed a procedure for assessing the probability of failure of onshore turbine towers based on the FORM. They also proposed a range of random variables capturing the uncertainty in modelling assumptions, loads and material properties, as factors multiplying the structural demand or capacity. However, mechanical models for OWTs are more complex because

they need to consider wind and waves simultaneously. The Incremental Wind-Wave Analysis (IWWA) was developed for Oil and Gas platforms [106] and models non-linear increases in bending moment due to increasing lever arm by directly applying wave heights as opposed to scaling loads, as the case in a standard pushover analysis. When applied to OWTs by Wei et al. [107, 18], the mean wind speeds and significant wave height were coupled using a joint-PDF. Static structural analysis was conducted at all combinations of the environmental conditions, yielding a deterministic response surface, and the capacity was defined by a code-based equation. Then the reliability was evaluated by using Monte Carlo simulation to sample from the response and capacity surface to calculate the probability of failure. The response surface was deterministic and avoided the need to run structural simulations for each sample, but made it difficult to assess random variables that alter the structural response. The material yield stress was included as a random variable by scaling the capacity surface to each sample. This technique would be difficult to apply to a probabilistic model with multiple random variables, as the capacity or demand curve would need to be scaled by each. Ultimately, the probability of failure for the NREL 5MW OWT on the Upwind jacket was found to be low at a site on the East Coast of the USA, except where hurricane loads were applied [18].

A strategy for including a wider range of random variables was utilised by Muskulus et al. [108] using importance sampling directly on a range of input variables; including material, hydrodynamic and aerodynamic properties. However, this study used an uncoupled time-domain structural analysis with impulse based sub-structuring (a technique developed to speed up structural simulation), taking rotor thrust from a fixed hub aeroelastic simulation. The random variables were applied directly to the structural analysis inputs and therefore this represents a progression from the method used by Wei et al. [18], which relied on deterministic inputs. Kim et al. [109] took a different approach to reliability assessment, using the FORM. They simplified the

structural assessment by using results from a static analysis multiplied by a dynamic amplification factor. Morato et al. [95] used a Kriging model, this approach involves building a surface to represent the response. This is similar to the approach used by Wei et al. [107, 18], however the Kriging approach includes statistical uncertainty of the structural model within the response surface, i.e., it is a stochastic response surface.

PBE was applied to onshore wind turbines by Quilligan et al. [110] to derive fragility functions considering uncertainties in material properties and loading as direct inputs to the structural demand calculation. In their assessment, failure is assumed to occur after a plastic hinge forms in the tower. The fragility of OWTs was investigated by Mardfekri and Gardoni [111, 112, 113] who developed fragility curves using dynamic analysis for the structural load calculation. They used Monte Carlo simulation to generate a sample from a wide range of random variables covering: material properties, load uncertainty and response uncertainty. A fully coupled dynamic analysis was run in FAST for each sample to assess whether or not structural failure would occur. In addition, they added a correction term directly to the FAST results; the correction was derived in advance by comparing dynamic simulation results to those from a high fidelity FEA model. Two fragility curves were produced with: (1) constant wave height $H_s = 1m$ and varying wind speed $V_w = [0:25]m/s$, (2) varying wave height $H_s = [1:10]m$ and three wind speeds $V_w = [3, 12, 25]m/s$. They concluded that the wave loads had little impact on the ULS fragility. However, only uncoupled wind and wave environmental conditions were considered, i.e., the mean wind speed was varied while the significant wave height was held constant and vice versa. This means that the fragility curves do not cover a sufficient range of conditions to be applicable to the environment experienced by real OWTs. Wei et al. [18] developed fragility curves for OWTs using the response surface technique described earlier. These were ultimately embedded within a larger hurricane risk assessment procedure for OWF located on the US Atlantic Coast [114]. However this framework stopped at

the evaluation of expected failure rates for different OWF sites, and did not attempt to evaluate losses. De Risi et al. [115] also developed fragility functions for OWTs experiencing earthquakes occurring during normal operating conditions.

This brief review has highlighted the lack of a harmonised framework for defining fragility functions for OWTs exposed to severe wind and wave conditions. In addition, there has been little research comparing the effect of different modelling assumptions on the fragility of OWTs and the impact that different random variable models, used to capture demand- and capacity-related uncertainty, have on the predicted failure rate.

### 2.4.2 Fatigue limit state reliability

Direct comparison between the existing FLS reliability studies is difficult because they have used a range of different substructures, including: tripods [116], jackets [117, 108] and monopiles [108, 118]. The different studies have also used a combination of frequency and time-domain load-response calculations. In each case, the fatigue life calculation used Miners law to calculate the damage arising from stress cycles counted using a rainflow counting algorithm. Only Dong et al. [117] used fracture mechanics, for helping to schedule structural inspections, where it is necessary to know the crack length.

Additionally, all have focused on OWTs in their operational state, therefore contributions to fatigue damage arising from storms, when OWTs are parked, have been neglected. Reliability calculations have been carried out using a variety of different techniques, including: the FORM [117, 118] and importance sampling [108]. A modified FORM approach was used by Yeters et al. [116], developed by fitting a distribution to the long term stress ranges calculated using FEA, this allowed a simpler limit state function to be constructed based on the distribution of stress and other random variables. The FORM was then used to calculate the probability of failure, without needing to recalculate the long term stress distribution. A response surface was used by Veldkamp [118], who fitted a 2nd order polynomial to the fatigue predicted

by time-domain analysis building a simple relationship of the output in the form of a multi-dimensional regression. Samples of the fatigue damage were extracted from this response surface using FORM, resulting in a reduced analysis load compared to using FORM directly on the output from time-domain simulation.

A number of studies have investigated which random variables effect fatigue loading the most. Muskulus [108] reported that varying the aerodynamic damping had the largest impact on fatigue life. Additionally fatigue damage resistance and soil stiffness were found to be important. This was partially confirmed Yeters et al. [116], who found that the reliability of the tripod was most sensitive to the aerodynamic force parameter they defined and least sensitive to the fatigue model variables. Some random variables such as fatigue damage resistance [108] can be sampled after the load-response calculation (i.e. FEA). This means that they can be sampled easily without the need to re-run computationally expensive FEA calculations. Others, such as aerodynamic damping would require a full re-run of the load-response calculation, which is time consuming as each load case need to be re-analysed. However this variable is likely to be more important when using an analysis technique in which aerodynamic damping is not explicitly modelled. In contrast, Veldkamp [118] found that material factors relating to the definition of the SN curve had the largest impact on fatigue reliability, with all other wind related variables contributing only 15% to to the variability in the probability of failure.

A useful contribution from the perspective of PBE was provided by Muskulus [108] who plotted fatigue damage caused by each wind speed. This provides a constant relationship between wind speed (IM) and damage (EDP) that could be combined with a external hazard model. A different approach to representing the FLS is to plot the increasing probability of fatigue failure over the structures life [117, 116]. Dong et al. [117] combined the time dependant structural reliability with a model for the effect of corrosion - estimating both the increased likelihood of a fatigue crack and decay in the properties of

the structure over time. This method for representing the FLS is particularly useful for planning the likely in-service inspection requirements for a structure.

The literature highlighted that no work, to date, has considered the FLS nor assessed an OWT within a PBE framework. Although a substantial contribution was made by Veldkamp [118] who has estimated financial costs associated with fatigue failure of OWT structural components.

## 2.5 Research gaps and proposed framework

The focus of this thesis is to develop a harmonised risk assessment procedure for OWTs, including both equipment and structural components. The preceding literature review has highlighted a number limitations in the current approaches used to assess OWTs.

In the discussion of risk for offshore wind, a key gap was the lack of a combined approach for assessing the different components of an OWT, as summarised in Section 2.2.4. The equipment and structural components are typically treated separately. The mechanical and electrical components are commonly assessed using empirical databases of observed failure rates. However, analytical methods are necessary to assess the reliability of the structural components, as their low failure rate means that historical empirical records are insufficient. Additionally, efforts to reduce conservatism in the structural capacity will make any existing empirical records inaccurate, as new structures may have a higher probability of failure than those currently installed. The correlation observed between the environmental conditions and probability of failure is particularly important for the structural components as these are directly exposed to environmental conditions, and consequently, a structural model needs to accurately capture both wind and wave loading. The literature review of the structural limit state for OWTs, Section 2.3.2 to 2.3.3, identified that both the ULS and FLS are relevant.

A number of limitations are present in current approaches to ULS assessment, a key one is that code specifications only assess environmental con-

ditions up to a MRP of 50 years. Additionally, the summary of reliability procedures applied to ULS analysis of OWTs indicated that a wide range of different techniques had been applied. However, none of literature reviewed has computed the full PBE, framework described in Section 2.2.2. Fragility analysis comprises a key component of PBE and the analytical approach requires a method for uncertainty quantification. All existing methods have evaluated fragility using simplified structural models, and none has developed a satisfactory method for considering the variability in wind and wave loading. Techniques using static analysis [119, 18] are not appropriate for dynamic monopile substructures. Those based on dynamic analysis [112, 108] rely on finite time-domain simulation which is assumed sufficiently long to capture the worst case combination of wind and wave loading. However, this assumption can cause the analysis model to under predict the ultimate loading [120], statistical treatment of the structural response can circumvent this problem [121]. Techniques based on capturing dynamic behaviour by combining the result of a static analysis with a dynamic amplification factor (Dynamic Amplification Factor (DAF)) fail to simplify the problem substantially. A large number of time-domain analyses are still required to define the DAF. There are however a set of reliability techniques which are suitable for fragility analysis of OWTs in the ULS. The approach used in IWWA is a logical method for assessing increasingly rare environmental conditions as it analyses stationary combinations of mean wind speed and significant wave height in order to calculate the response. It results in an approach which could build a fragility curve. Therefore this technique produces results which fit easily within a PBE model. The main gap lies in using dynamic structural analysis within the IWWA framework to capture the reliability of OWTs.

A more general gap is present for the FLS relating to the methods that are appropriate for implementing reliability analysis. As discussed, in Section 2.4.2, there have been a very limited number of general FLS reliability studies across all civil engineering fields, not just for OWTs. To date, no attempts

have been made to represent the FLS within a PBE modelling framework, as fatigue damage estimates are time dependent and are therefore difficult to decompose into the fragility and hazard components. However, it is possible to represent fatigue loading using damage over the structures life, which will allow a FLS to be assessed.

The main challenge present in developing structural models of OWTs is caused by the need to assess loads arising from two stochastic processes (wind and waves) simultaneously, as described in Section 2.3.1. Simplifying the OWT model by assuming that the wind and waves act statically means that important structural behaviour is neglected. For instance, when the turbine is operational a static analysis would be unable to capture coupling between the wind load, wave load and tower motion. Coupled analysis techniques simulate joint wind/wave loading but have long run times. This becomes important when many calls to the analysis package are required, as is the case in a reliability analysis of the FLS. This project utilises FAST for the full structural analysis, due to the error introduced by using other, simpler, models [122].

In summary, the primary objective of this thesis is to develop a framework for quantifying an OWT's structural risk, using structural reliability assessment to evaluate the ULS and FLS. Moreover, this thesis aims to produce a combined assessment framework which also includes the equipment. The focus on structural components is necessary due to the lack of existing formalised approaches. These two limit states will be addressed seperately using the general framework presented in Figure 2.11 for the ULS and Figure 2.12 for the FLS.

This study addresses the gaps highlighted in the preceding review through the steps summarised below:

1. Development of a framework for calculating the ULS risk of OWT structures using coupled time-domain simulation. In fact, existing work has used static or uncoupled dynamic methods. The proposed approach also ensures that the predictions of structural failure can be combined with

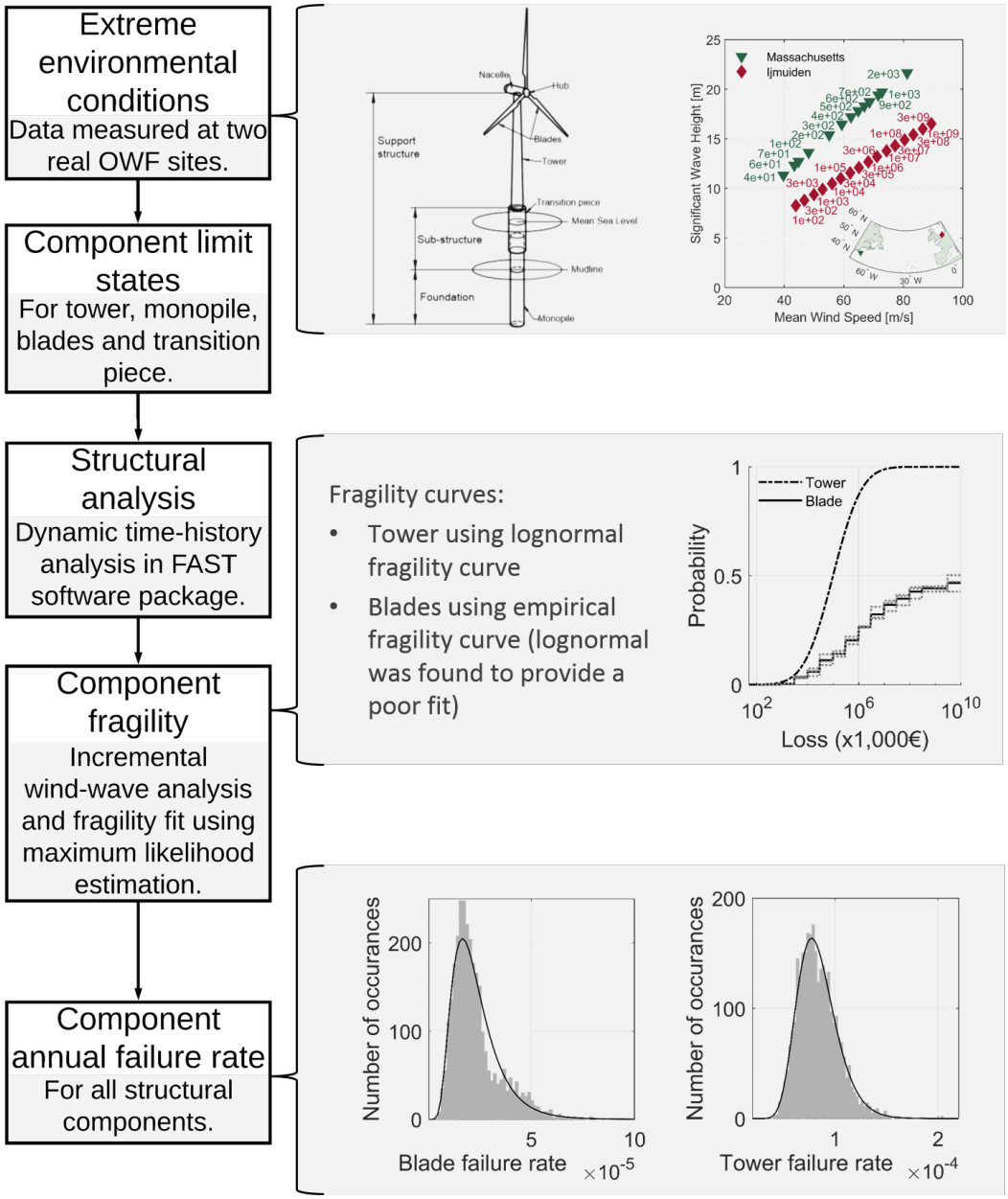


**Figure 2.11:** Framework proposed to assess ULS risk.

equipment failure in terms of financial loss.

The general methodology followed for risk calculation is shown on Figure 2.11, where extreme environmental conditions at real offshore wind farms will be used as input to a PBE framework. Fragility curves will be defined to capture the probability of failure of different structural components as the environmental conditions change in severity. Finally, fragility curves

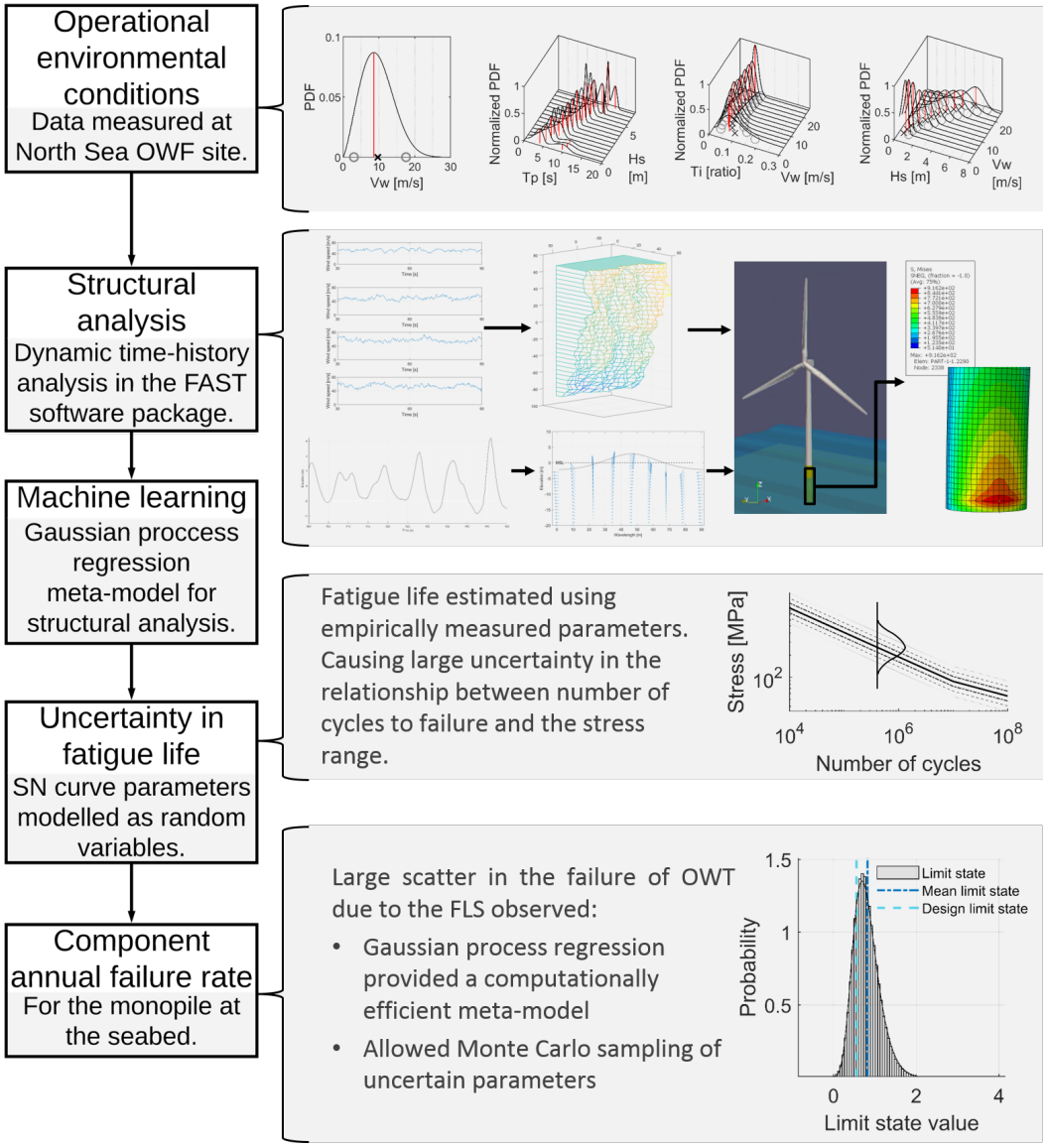


**Figure 2.12:** Framework proposed to assess FLS risk.

can be converted into distributions of annual failure rates. This will allow a separate loss calculation to be developed that can combine failure of the structural components with the equipment in terms of financial losses.

2. Application of the proposed ULS framework to case-study OWTs/sites to demonstrate the calculation steps in the proposed framework and assess financial losses.

3. Development of a framework for assessing FLS risk, as limited work has been completed in this area to date. One of the challenges highlighted in

the literature review relating to the FLS is the inclusion of the full range of environmental conditions an OWT is expected to experience during its operating life.

The approach that will be taken is summarised in Figure 2.12, where the FLS is assessed over the full range of operational environmental conditions. This calculation is made computationally feasible by applying the machine learning technique GP regression, which is used as a surrogate model for the fatigue damage calculation. This approach will allow uncertainty in the fatigue material properties to be captured and ultimately enable calculation of annual failure rates for structural components in the FLS. The failure of structural components can then be combined with the equipment using the previously developed loss calculation.

4. Application of the proposed FLS framework to case-study OWTs/sites to demonstrate the calculation steps in the proposed framework and assess financial losses.

# Chapter 3

# Ultimate limit state loss framework

## 3.1 Introduction

The ULS assesses failure of a structural system due to overload of its components in the form of yielding or buckling, as introduced in Section 2.3.2. For OWTs this type of loading is a result of the site-specific wind and wave conditions that are expected to be encountered over the turbine's life. These can include severe typhoons in Asia, hurricanes in the USA, and extra-tropical cyclones (windstorms) in Europe. Indeed, failures of the tower and blades on smaller onshore wind turbines have been observed as a result of recent typhoons in China [99], during which 10-minute averaged hub height wind speeds in excess of 60m/s were recorded.

The design and assessment of OWTs is currently based on semi-probabilistic prescriptive approaches, described in IEC code 61400-3 [6] and DNVGL-ST-0126 [91]. These standards employ the LRFD approach in an attempt to guarantee a certain safety level in structural components. In particular, current state-of-the-art codes and standards do not explicitly consider the structural risk posed by uncertainties associated with physical properties of OWTs (e.g., material, geometry) and loading conditions (e.g., wind and wave loading). Instead, they deal with such uncertainties in a conservative

way, by employing safety factors to ensure a structure (or a structural component) does not fail with a frequency greater than a pre-defined, target rate. However, as discussed in Section 2.3.2 these safety factors have not been calibrated specifically for OWT. Any "integrated design" of new OWTs (or assessment of existing ones) should explicitly account for both uncertainty in environmental conditions, especially those occurring during extreme events (e.g., severe windstorm), as well as the possibly complex interdependencies between components. For instance, stopping the rotor will change the loading on the blades which will in turn influence loads on the tower and monopile. The problem is how to quantify the risk associated with these diverse subsystems in a coherent way, accounting for the impact of their failure on the overall structural performance of the farm. The concept of resilience provides an effective framework in which to assess an OWT as a system of integrated structural and mechanical/electrical components, focusing on the functionality performance of the overall system and not just that of individual components.

Resilience was defined in the literature review, Section 2.2.1 and 2.2.1. This definition is developed in Section 3.2 where resilience is discussed in relationship to the specific problem of assessing OWT performance. The analytical method proposed to assess the combined losses of the structural and mechanical / electrical components is discussed in Section 3.3. Annual losses associated with the failure of an OWT system are evaluated by combining the probability of failure of the individual components in Section 3.3.5. This includes a procedure for evaluating the failure probability of the structure based on a PBE modelling approach, which employs time-domain structural analysis and uncertainty modelling to derive structural fragility (i.e., the likelihood of different levels of damage experienced by the OWT over a range of hazard intensities). The overall calculation is illustrated through a case-study in Chapter 4 at two wind farm locations: one in the Dutch sector of the North Sea, experiencing windstorms (extra-tropical cyclones), and another on the USA East Coast, experiencing hurricane-like conditions.

## 3.2 Structural resilience

The concept of resilience provides an effective framework for enabling integrated design of a given engineering system, allowing a rational assessment of the system performance in the presence of uncertainties. Resilience can be numerically quantified as the area below a system's performance curve, and is quantified through the following four metrics which characterise a given system, as discussed in Chapter 2:

- Robustness,
- Rapidity,
- Redundancy,
- Resourcefulness.

It may be difficult to quantify some of these metrics, especially at the design stage. For instance, information regarding the capacity of an organisation to make budget available in the case of a disruptive event (i.e., part of resourcefulness) is seldom available to a design engineer. Nor would it be clear to a designer whether an operator would decide to restore functionality to an improved, the original or a degraded level (i.e., $t_D$ in Figure 2.1). A methodology for assessing structural resilience of OWTs relying on their robustness features would allow this concept to be directly applied at the design stage. The initial design-stage estimate of an OWT robustness could be used in a full resilience calculation at a later stage which would also consider recovery. An approach, investigated by Bruneau and Reinhorn [49] and applied here, assumes that loss of functionality after a disruptive event and the time to recovery are highly correlated. This is intuitive as, in general, if an event (e.g. a windstorm) causes more damage, it will take longer to repair the considered asset. A similar approach has previously been applied to structures experiencing blast by defining a relative resilience indicator ($RRI$), which is correlated to the overall structural resilience ($R$) as follows [48]:

$$R(Ev) \propto RRI(Ev) = 1/C(Ev). \tag{3.1}$$

In Eq. (3.1), $RRI$ can be defined as the inverse of the consequence ($C$) of a disruptive event ($Ev$). Under this assumption, a structure experiencing a lower consequence (i.e., less damage and lower financial loss) as the result of a hazardous event, is viewed as more resilient.

This approach requires a metric quantifying the consequence of failure that correctly represent the effect of failure of individual components on the OWT (or OWF) functionality. Considering a single OWT structure, loss of an important sub-assembly will completely stop production, resulting in the OWT dropping to zero functionality. However, the failure of different components will have different implications in terms of recovery time. Therefore, it is not enough to define consequence using the reduction in functionality caused by component failure alone. This consideration also precludes the use of some common structural consequence measures, such as percentage of the structure collapsing [48], or percentage of mechanical components failing, which do not provide sufficiently detailed information about the type of failure. Other metrics, such as those relating to life-safety are not of primary importance for offshore wind as turbines are normally unmanned, apart from brief periods of maintenance activities [105]. Rose et al. [123] quantified resilience of an OWT through robustness by estimating the cost incurred by loss of functionality after an extreme event. This allows the failure severity of different components to be compared within a unified metric, because each has a different material (replacement) cost. Financial loss is also easy to communicate to stakeholders and is therefore used in this study. However, it neglects the operational costs of repair, such as hiring vessels, which are expensive but the precise costs are difficult to quantify as the length of the hire is unknown.

## 3.3 Probabilistic risk modelling for offshore wind turbines

A probabilistic risk modelling framework is proposed to assess structural risk associated with OWTs in their ULS exposed to extreme environmental conditions. This approach is based on decomposing the total risk into conditional probability distributions which are evaluated sequentially and finally combined using the law of total probability, as discussed in the literature review. It can be used in principle to 1) test new design strategies, extending performance-based design frameworks to account for multiple hazards; 2) devise efficient and targeted asset management techniques; and 3) develop resilience-enhancing solutions for combined wave and wind hazards, e.g. based on structural health monitoring and structural control. These options all rely on assessing the risks associated with OWTs, including uncertainties in structural modelling and analysis. The basic structure of a probabilistic risk model was discussed in the literature review, Section 2.2.1, where the overall framework is decomposed into a series of sequential components [124]. Given knowledge about the repair costs for different types of damage, vulnerability functions can be estimated, defining the relationship between hazard intensity and expected loss [125].

$$\lambda(L) = \iint F[L|DS] \cdot |f[DS|IM]| \cdot |d\lambda(IM)|. \tag{3.2}$$

In Eq. (3.2), the variables are $\lambda(L)$ the rate of incurring a level of financial loss ($L$), $F[\cdot]$ a CDF, a measure of the intensity of a natural hazard (intensity measure; or IM), e.g., wind speed or wave height, and damage states ($DS$s), e.g., the performance level of the structure and/or its components, as a function of the given IM. This framework was schematically represented through the flowchart in Figure 2.3, in the literature review Section 2.2.1, where the individual tasks include:

- Hazard analysis,

- Exposure (or structural) characterisation,
- Fragility analysis,
- Loss analysis.

Structural and equipment components need to be treated differently because structural failure is usually predicted analytically (or numerically) based on structural simulations, whereas equipment failure data are usually obtained from empirical databases, mainly recording the rate of failure without reference to specific environmental conditions. Consequently, equipment failure is not typically conditional on the IM and does not require site-specific analysis. The general probabilistic risk modelling framework shown in Figure 2.3 can be adapted to the specific loss analysis of an OWT (Figure 3.1), considering both structural and mechanical/electrical equipment. The elements of Figure 3.1 are described in more detail in the following sub-sections.

### 3.3.1 Hazard modelling

The primary environmental perils that threaten an OWT are those relating to severe wind and/or wave conditions. Wind and wave conditions are frequently parametrised using a separate variable to describe the severity of each (this is further discussed in Section 4.2.1). Common choices are the significant waves height (i.e., the average trough to crest height of the highest one-third waves in a sea-state [82]) and mean wind speed (averaged over a 10-minute period). The variables can be combined into a single IM by assuming that wind and waves are linked through the MRP, i.e., the most extreme conditions associated with each MRP are coincident, a conservative, yet practical assumption used to assess OWTs [119]. If the hazard model is based on site environmental measurements that are comprised of a limited amount of data, the uncertainty introduced as a result of the limited number of observations should also be quantified.

Specific values of mean wind speed and significant wave height can be calculated using an appropriate probabilistic model, which describes frequency

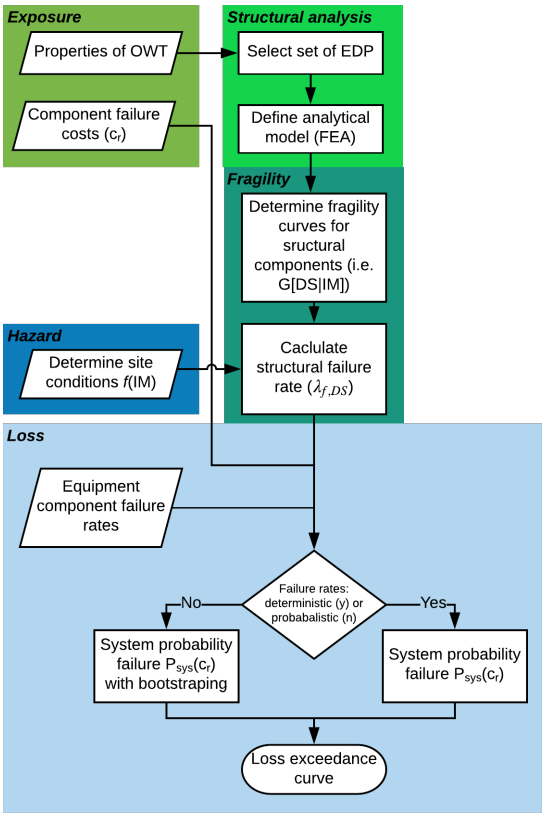


**Figure 3.1:** Proposed probabilistic risk modelling methodology used to calculate financial losses in this study.

of occurrence of the environmental conditions at a site.

### 3.3.2 Exposure modelling

The structural response of an OWT is highly dependent on turbine-specific parameters including the power rating and control system [39]. Consequently, exposure data has to be more detailed than typically used in a probabilistic risk model for buildings, where only general information (e.g., in terms of construction class, height, and age of construction) about a portfolio of assets may be included [51]. Exposure data should include all pertinent information required to compute loss of the structure being assessed. This includes: location, geometric characteristics, material properties, and failure costs (i.e., replacement costs) for the OWT components.

### 3.3.3 Structural analysis

This step involves building a computational model capable of predicting the response of the OWT to environmental conditions (wind and waves) represented through the selected IMs. For an OWT exposed to stochastic environmental loading, the use of time-domain analysis is a common approach [39]. The first step consists in specifying a set of EDPs representing the response of the structural components of interest and computed through structural analysis. A key element of this process involves a set of Damage States (DSs) defining structural performance criteria. Violation of a limit state indicates failure of the structure [64] and these conditions are usually formulated as an equation containing a capacity (or resistance) and a demand (or load effect) terms. In the ULS, for instance, failure of an OWT relates to the exceedance of the structure's load-carrying capacity [6], where the demand is a function of the forces caused by environmental loading and the capacity relates to the ability of the structure to withstand these loads. All structural components are exposed to this form of failure and should therefore be assessed by an analytical model including the: tower, monopile, transition piece and blades; see Section 4.2 for a longer discussion of OWT limit states.

### 3.3.4 Fragility analysis

Fragility functions express the probability that a damage state occurs for a level of hazard intensity (IM), typically as a conditional complementary CDF, $F[DS|IM]$ [59]. Damage states can range from minor damage to complete structural collapse and are typically defined in terms of EDPs, e.g. the stress in a component or hub displacement. They are used to assess the exceedance of calibrated EDP thresholds for each limit state of interest. In the case of OWTs, the environmental conditions are represented through an IM which generates structural loading, and ultimately an EDP.

A structural analysis model is typically used to estimate the probability of failure conditional on the IM. This is achieved by running simulations repeatedly over a discrete set of IM values, resulting in a set of analysis outputs

corresponding to each realization of the IM. Scatter in the fragility function parameters is caused by different wind and wave time-series causing different structural loading, and the effect of other random variables used to model structural demand and capacity. The probability of failure can be estimated as the mean number of structural analyses resulting in exceedance of the considered limit state (i.e., failures) at each IM value. The probability of failure can then be expressed as a functional relationship either by fitting a parametric distribution or directly using the output from structural analysis to generate an empirical fragility curve (e.g. [126]).

Fragility functions can be combined with a hazard model to compute the mean annual rate of damage state exceedance, $\lambda_{f,DS}$, of the considered asset, as in Eq. (3.3):

$$\lambda_{f,DS} = \int_{IM} F[DS|IM] \cdot |d\lambda(IM)| \approx \sum_{i=1} F[DS|IM_i] \cdot \Big(\frac{1}{MRP_i} - \frac{1}{MRP_{i+1}}\Big). \quad (3.3)$$

The term $d\lambda(IM)$ in Eq. (3.3) can be computed through the derivative of the hazard curve ($\lambda(IM)$); it can be approximated by converting each MRP into an annual rate of exceedance as shown in Eq. (3.3) and summing over a discrete set of MRP values, indexed by $i$. The fragility functions are calculated using a sample of structural simulations and are therefore associated with uncertainty. The effect of this statistical error can be quantified by resampling the chosen consequence metric (defined in the following section) using bootstrapping [127]. This method was developed during the 1990's computing power became widespread as it estimates standard errors and confidence intervals of a sample by repeated re-sampling [127]. The data samples are assumed to be representative of the population, and these are re-sampled with replacement, allowing standard errors within the sample to be calculated. The application of this technique is discussed in the case study, Section 4.6.1.

This calculation required a method for assessing wind- and wave-induced demands to the OWT structure. One applicable method is the IWWA proposed for OWTs by Wei et al. [119]. In this case, the OWT structural response is assessed at progressively severe environmental conditions, consisting of significant waves heights (i.e., the average trough to crest height of the highest one-third waves [128]) and mean wind speeds. However, the numerical model used to evaluate the structural response is associated with idealisations, and introduces uncertainty into prediction of the structural response. These effects are modelled as random variables, with a defined probability distribution, and need to be sampled at each environmental condition, i.e., corresponding to pairs of wind and wave conditions, for input to the numerical structural model. This results in a fragility calculation procedure that is very similar to the multi-stripe analysis method commonly used in earthquake engineering [129]. In IWWA, wind and wave conditions can be coupled using the MRP, or assessed jointly [119]. The output is the structural response to increasingly rare environmental conditions. MRP values can be used as a proxy for the environmental conditions at the site (either from site measurements or by using a climate model). Due to the low stiffness of OWT on monopiles in comparison to those on jackets, which were the focus of existing implementations of IWWA [18], and to explicitly capture the dynamic response to loads, IWWA combined with a coupled time-domain analysis [39] is used here for OWTs on monopile substructures.

The fragility calculation procedure which uses IWWA1 consists of the six steps listed in the flowchart in Figure 3.2. These include:

1. Select a suite of IMs which can be used as predictors of the considered EDPs; here the MRP is used with $N_{MRP}$ being the number of MRP evaluated at a given site.

2. Calculate mean wind speed ($V_w$) and significant wave height ($H_s$) from independent probability distributions, using the MRP to select events with equivalent severity. The probability distributions should be devel-

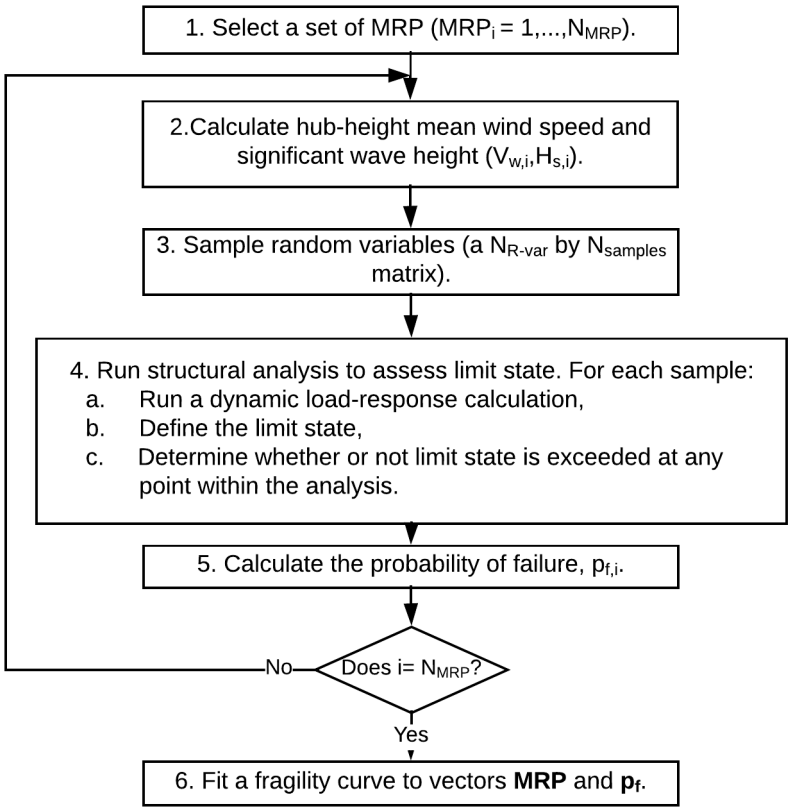


**Figure 3.2:** Flowchart describing the fragility calculation procedure.

oped for the OWF site-specific conditions.

3. Generate a Monte Carlo sample containing realisations of the environmental conditions (in terms of turbulent wind and wave time histories) and other random variables which influence the demand and capacity of the OWT (where $N_{samples}$ realisations of those random variables are generated at each MRP). This step is discussed in more depth in Section 4.3.3. The total number of random variables is $N_{R-var}$.

4. Run structural analysis and evaluate every limit state equation for each Monte Carlo sample at all MRP assessed; this employs a total of $N_{MRP} \cdot N_{samples}$ structural simulations.

5. Estimate the probability of failure at each MRP, as discussed in Section 4.3.3.

6. Fit fragility function to the pairs of MRP and probabilities of failure calculated in step 5.

### 3.3.5 Loss assessment

In general, for a system with a number ($N_{sys}$) of independent components, each of which has two discrete states (failure or operation), there is a finite number of permutations in the system state, where the total number of combinations of component events (leading to system events) is $2^{N_{sys}}$. These combinations of operating and failure states can be summarised in a matrix $\boldsymbol{A}$ [130], with elements $a_{ij} \in \mathbb{Z}$ and $[a_{ij}]$ is a $N_{sys} \cdot 2^N_{sys}$ matrix, Where the index $i$ refers to a component of the OWT and the index $j$ to an operational state. An entry of one indicates that the component fails or zero indicates that it remains operational. For a generic OWT with 11 components used in the case study are presented on Table 4.5), the matrix $\boldsymbol{A}$ will have elements $a_{ij} \in \mathbb{Z}^{11 \cdot 2048}$; the first column will read $[00000000000]^T$ indicating the case in which all components are functional, and the last $[11111111111]^T$ indicating the case where all components have failed. The intermediate columns will contain all other permutations of ones and zeros for different system states.

If each component has a deterministic cost, the discrete system failure events can be combined to assess the probability of incurring a total material cost ($c_r$). The matrix of the failure events $\boldsymbol{A}$ is converted into a failure cost matrix $\boldsymbol{A}_c$ by multiplying each column of $\boldsymbol{A}$ by a vector containing the repair cost of each component. This new matrix will contain the same number of elements as $\boldsymbol{A}$ but the values will equal the material costs as opposed to a logical value (1 or 0). Then $P_{sys}(c_r)$ can be defined as the probability that a set of components $\boldsymbol{a}^* \in \boldsymbol{A}_c$ fail whose combined material cost is equal to the target ($c_r$):

$$P_{sys}(c_r) = \sum_{\boldsymbol{a}^* \in \boldsymbol{A}_c} \prod_{i=1}^{N_{sys}} P_i^{a_i} (1 - P_i)^{1 - a_i}, \tag{3.4}$$

$P_{sys}(c_r)$ is evaluated over all the columns of the $\boldsymbol{A}$ matrix where the total

material cost of the components equals $c_r$, i.e., $\boldsymbol{a}^*$ is a subset of $\boldsymbol{A}$ containing all vectors of system status with an equal cost. The probability of each system material cost is the product of the individual component failure probabilities in the matrix of failure events $\boldsymbol{a}^*$. This assumes statistical independence between the different components and is discussed further in relation to a OWT system in the case study, Section 4.2. When an element of the $\boldsymbol{a}^*$ matrix $a_i$ is zero then the probability that the component survives is used, i.e., $(1-P_i)^{1-a_i}$; and if $a_i$ is 1, then the probability that the component fails is used, i.e., $P_i^{a_i}$.

In Eq. (3.5), the overall failure consequence, $C$ (Eq. (3.1) or total annual loss, can be calculated by multiplying the yearly probability of different failure costs occurring ($P_{sys}(c_r)$) by the failure consequence defined by direct material cost ($c_r$) and summing over all failure costs:

$$C_{storms} = Loss_{total} = \sum_{c_r} P_{sys}(c_r) \cdot c_r \tag{3.5}$$

## 3.4 Conclusions

This chapter proposed a probabilistic risk framework to quantify economic losses due to extreme environmental conditions for an OWT. This framework has been applied to a wide range of similar problems in civil engineering and therefore has a strong basis.

Resilience is simplified here to the estimation robustness through financial losses resulting from OWT failure. This allows the idea of resilience to be applied by practising engineers who will not have access to the full data required for an evaluation of resilience, which includes subsequent recovery phases. Robustness is a component of a full resilience calculation, the simplified method presented in this chapter could be used as an input to a more comprehensive resilience assessment.

A method for calculating fragility curves based on time-domain structural analysis is proposed. This is based on the robust IWWA methods developed for offshore Oil and Gas structures. This calculation is implemented in Chapter

4, which demonstrates a each step of a probabilistic risk framework.

# Chapter 4

# Implementation of ULS loss framework

## 4.1 Introduction

A new framework for evaluating financial losses associated with the components of an OWT was developed in Chapter 3. In this Chapter the framework is applied to an OWT located at two case study OWFs. The approach taken is to quantify financial losses using the material replacement cost of each OWT component. This provides a simple metric for OWT performance in the form of annualised material losses, allowing results from the two OWF to be compared directly.

The case study locations and OWT structure are introduced in Section 4.2. This includes failure data for the equipment and details of the analysis conducted to assess failure of the OWT structural components. Fragility curves are derived for the main structural components of the OWT using limit states defined in Section 4.3, and then presented in Section 4.4. These are used in combination with the mechanical and electrical component failure rates to produce annual loss estimates for the case study locations in Section 4.6. Finally the results of the case study and limitations in the framework are discussed in Section 4.7.

## 4.2 Case study offshore wind farm

Two locations, both suitable for OWFs, but experiencing contrasting environmental conditions, are investigated in this study. These sites were selected because wind farms have been built or are planned, meaning the case study is representative of real OWF sites. The Ijmuiden K13 site (referred to as Ijmuiden site in the rest of this chapter) [131] is located in Dutch waters between the Hollandse Kust Zuid and Noord wind farm development sites, and is exposed to extra-tropical cyclones. The other site is exposed to hurricanes and is located on the USA East Coast, offshore from Massachusetts [18] (at 40.5°N 69.3°W), an area proposed for future wind farm developments [24].

The environmental conditions associated with a set of different MRPs are plotted on Figure 4.1 (left). The MRPs for the Massachusetts site are selected to cover the mean wind speed range from 40m/s to 80m/s. High MRP at the Ijmuiden site are necessary to produce fragility functions that can capture failure of structural components, which are rare, as discussed in Section 4.4, and these require extrapolation far beyond measured environmental conditions. However, this will not affect the main conclusions of this study, which relate to the relative properties of the fragility functions derived for both sites and different modelling/analysis assumptions.

The water depth at the Ijmuiden site is around 20m, making it a suitable location for the NREL 5MW OWT on a monopile foundation. The Massachusetts site is deeper than 20m, but is assumed to have this water depth so direct comparisons can be drawn between the two sites. The main elevations of the structure are shown in Figure 4.1 (right). As indicated in the figure, the tower reaches a top elevation of MSL+87.6$m$. A more detailed description of the turbine is provided in Section 4.2.2.2.

### 4.2.1 Hazard model

The hazard intensity calculation is simplified in this study by combining the wind and wave conditions into a scalar IM, the MRP, as shown on Figure 4.1 (left). This approach conservatively assumes that the maxima of wind and

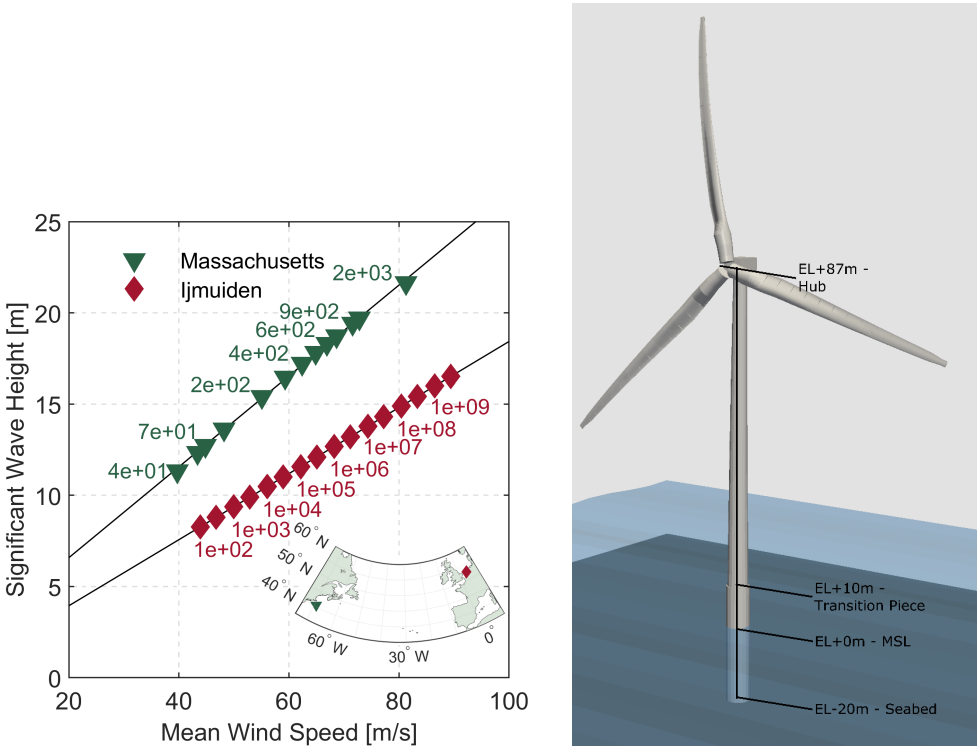


**Figure 4.1:** Comparison of the extreme wind and wave conditions associated with different MRPs at Massachusetts and Ijmuiden OWF sites (left) where the MRP is plotted beside the data points; the inset map shows the locations of both sites. The schematic figure of the case-study OWT used in this study, with main elevations highlighted (right).

wave occur simultaneously. It simplifies the analysis substantially, reducing the number of required structural simulations. Wei et al. [119] have found that using environmental conditions coupled through MRP values instead of their joint probability distributions has little impact on the computed probability of failure .

Mean wind speeds and significant wave heights are plotted against their corresponding MRPs in Figure 4.1 (left). Both sets of data were evaluated using site measured data, however different statistical model were found to represent the environmental conditions experienced at both sites best.

Ijmuiden has 22 years worth of wind and wave measurements [131]. A statistical model representing the occurrence of different mean wind speeds and significant wave heights [82] was developed by Fischer et al. [131] by applying linear regression with log correction to the recorded data:

$$H_s = 0.479 \cdot ln(MRP) + 6.063 \tag{4.1}$$

$$V_w = 2.645 \cdot ln(MRP) + 31.695. \tag{4.2}$$

In Eq.(4.1) and (4.2), $H_s$ is the predicted three-hour significant wave height in meters, and $V_w$ is the 10-minutes hub-height mean wind speed in m/s (10 minute averaging is a standard assumption based on the observation that mean wind speed is approximately static over this period of time [11]).

At the offshore Massachusetts site, hurricane conditions were estimated by Wei et al. [18] who simulated a stochastic catalogue of hurricanes over a 100,000 year period (the typical length of stochastic catalogues in CAT models) and fitted a Generalised Extreme Value (GEV) distribution to the calculated mean wind speed and significant wave height at different MRP. The model used in this study was calculated by fitting a GEV distribution to the points provided, the probability distribution ($f(x_{GEV}|k_{GEV},\sigma_{GEV},\mu_{GEV})$) is defined:

$$f(x_{GEV}|k_{GEV},\sigma_{GEV},\mu_{GEV}) = \frac{1}{\sigma_{GEV}}\left(1+k_{GEV}\frac{x_{GEV}-\mu_{GEV}}{\sigma_{GEV}}\right)^{(-1/k_{GEV})-1} exp\left(-\left(1+k_{GEV}\frac{x_{GEV}-\mu_{GEV}}{\sigma_{GEV}}\right)\right)^{1/k_{GEV}}, \tag{4.3}$$

where the model parameters are shape ($k_{GEV}$), scale ($\sigma_{GEV}$) and location ($\mu_{GEV}$). These are defined for the Massachusetts site using the values in Table 4.1. The $x_{GEV}$ variable represents either the yearly maximum 10-minute mean wind speed or significant wave height, depending on which set of parameters are used. The environmental condition associated with a desired return period can be calculated by evaluating the inverse CDF of each distribution independently using the parameters defined above. These distributions were fit to wind speeds converted from 10m to hub height values by a factor of 1.289 [18].

**Table 4.1:** GEV parameters for the environmental conditions at the Massachusetts (MA) wind farm site [18].

| **Parameter** | **Shape ($k$)** | **Scale ($\sigma$)** | **Location ($\mu$)** |
|---|---|---|---|
| $V_w$ | 0.0915 | 6.2898 | 12.2264 |
| $H_s$ | 0.0382 | 2.1172 | 2.9719 |

It is worth noting that a more detailed approach based on physics-based event generation may be more suitable to capture the correlation between wind and wave conditions at rare MRP [18]. However, the IEC guidelines [6] specify a method for estimating a joint probability distribution function of wind and wave conditions from basic site measurement data. At higher MRPs, the wave conditions become more complicated, as waves start to break, and therefore the maximum MRP has been limited to a value smaller than the one causing structural failure in some cases. A set of 16 MRPs are assessed here, as listed in Table 4.2. The corresponding wind and wave values have been calculated using the distribution assumptions from Eq. (4.1) and (4.2) for Ijmuiden, and Eq. (4.3) for Massachusetts.

Misalignment between the wind and wave conditions would also have an important impact on structural loading. This was not modelled in the present study as, at high mean wind speeds (above 30m/s), the misalignment was observed to reduce at the Ijmuiden site [131] and for the Massachusetts site this information was not available.

**Table 4.2:** MRP and corresponding environmental conditions at Massachusetts and Ijmuiden wind farm sites.

| **IJ MRP** | 1E+2 | 3E+2 | 1E+3 | 3E+3 | 1E+4 | 3E+4 | 1E+5 | 3E+5 | 1E+6 | 3E+6 | 1E+7 | 3E+7 | 1E+8 | 3E+8 | 1E+9 | 3E+9 |
|---|---|---|---|---|---|---|---|---|---|---|---|---|---|---|---|---|
| **MA MRP** | 4E+1 | 6E+1 | 7E+1 | 1E+2 | 1E+2 | 2E+2 | 2E+2 | 3E+2 | 4E+2 | 5E+2 | 6E+2 | 7E+2 | 9E+2 | 1E+3 | 1E+3 | 2E+3 |
| **IJ $V_w$ (m/s)** | 44 | 47 | 50 | 53 | 56 | 59 | 62 | 65 | 68 | 71 | 74 | 77 | 80 | 83 | 86 | 89 |
| **IJ $H_s$ (m)** | 8 | 9 | 9 | 10 | 10 | 11 | 12 | 12 | 13 | 13 | 14 | 14 | 15 | 15 | 16 | 17 |
| **MA $V_w$ (m/s)** | 40 | 43 | 45 | 48 | 51 | 53 | 56 | 59 | 61 | 64 | 67 | 69 | 72 | 75 | 77 | 80 |
| **MA $H_s$ (m)** | 11 | 12 | 13 | 14 | 14 | 15 | 16 | 16 | 17 | 18 | 18 | 19 | 20 | 20 | 21 | 21 |

### 4.2.2 Turbine mechanical model

#### 4.2.2.1 Environmental load

The sea-state is modelled as a random process, using a wave spectrum to represent the energy content of different frequency waves. The assumed spectrum is the JONSWAP [132] and a wave height time-series is then generated by using the inverse Fourier transform. The spectrum is calculated using the method recommended in IEC 61400-3 Annex B [6]. It is defined through the parameters:

- significant wave height, which determines the energy content of the spectrum.
- peak spectral period ($T_p$), the wave period at which the wave spectrum has a maximum [6].
- peak factor, which determines how peaked the spectrum is [132].

As the peak spectral period is an environmental variable, it can take on a range of values and can be defined statistically. However in this calculation it was defined deterministically using the range of $T_p$ values necessary to meet provisions in IEC-61400-3 specified by Myers et al. [14] as indicated in Eq. (4.4). In this work, only the lower bound value is conservatively used since it generates the largest loads, making the wave spectrum closest to the natural frequency of the OWT.

$$11.7 \cdot \sqrt{H_s/g} \leq T_p \leq 17.2 \cdot \sqrt{H_s/g}. \tag{4.4}$$

From the wave height time-series, the kinematics of individual water particles distributed along the monopile are calculated using the 2nd order wave model developed by Agarwal and Manual [133]. This time-series is converted into structural loads using Morrison's equation (implemented in the software package HydroDyn [134]).

The turbulent wind acting on the OWT is continuous but is commonly evaluated numerically at discrete points on a grid overlying the structure. Turbulent wind time-series are evaluated using the program Turbsim [135], which converts a Kaimal spectrum with turbulence type 'B' [128] into a stochastic wind velocity field using inverse Fourier transforms at each grid point. The correlation between the wind speed at different point is captured using an exponential coherence model as recommended in IEC 61400-1 [94]. Wind shear, changing mean wind speed with elevation, was include using a power-law profile with exponent 0.14 [128].

#### 4.2.2.2 Global structural analysis

Structural analyses are based on time-domain simulation with integrated wind and wave loading. Dynamic response of the structure to this loading is calculated using the aero-elastic computer-aided engineering software FAST [77] to run sets of time-domain analyses. Within FAST the tower, monopile and blades are modelled as Euler-Bernoulli beams. No below seabed foundation is included within the structural analysis.

The OWT considered in this study is based on the NREL 5MW reference turbine [42] with a monopile sub-structure, as shown on Figure 4.1 (right) and main properties listed on Table 4.3. The hub is supported by the tower and is located at Elevation (EL)+87.6m above the MSL. It is attached to a 126m diameter 3-bladed rotor, where the blades are labelled as blade 1, 2 or 3. The hub can rotate around the central axis of the tower, where any misalignment between the rotor axis and wind flow is referred to as yaw error. In this situation the inflowing wind is no longer perpendicular against the rotor plane and the loading on the structure tends to increase [136]. The blades rotate about a horizontal axis running through the centre of the rotor plane; the blade position is described by the azimuth angle: when azimuth is 0° blade 1 points directly upwards; as the azimuth angle increases, blade 1 rotates clockwise about the rotor-axis if observed while facing downwind. The monopile support structure spans from EL+10m to the mudline at EL-20m. At the base

of the tower, a transition piece connects the tower and monopile. A full list of dimensions and material properties of the turbine structure are provided by Jonkman et al. [42]. The dimensions of the material properties and the geometry of the NREL 5MW blades are provided by Resor [137]. Finally, the dimensions of the transition piece used in this study are taken from Lee et al. [138]; these are local geometrical properties and, as such, did not impact the global analysis but were used to evaluate the failure limit state.

The NREL 5MW turbine has a cut-off speed 25m/s, when this hub mean wind speed is exceeded, the rotor enters its parked state by pitching the blades into the wind to prevent damage. In all the analyses, the mean wind speed was well-above the cut-off as this work assesses mean wind speeds well above the prescribed 50-year extreme MRP.

#### 4.2.2.3 Model limitations

The assumptions used in this study introduce a number of simplifications into the load-response calculation, primarily: no foundation is modelled but the soil is flexible and behaves non-linearly at high loads [139]. The error that this assumption introduces into a dynamic analysis is discussed in Appendix A through the error in dynamic amplification. Additionally, the aero-elastic code FAST is based on small deflections and is not as accurate as non-linear aeroelastic methodologies [140] for capturing extreme and transient loading.

The 2nd order wave model cannot capture the loads caused by large or breaking storm waves. However, the aim of this analysis is to compare the relative features of the fragility functions dependent on different assumptions.

**Table 4.3:** Table of main dimensions for the NREL 5MW OWT.

| **Parameter** | **Value** |
|---|---|
| Mass of the rotor-nacelle assembly (kg) | 350,000 |
| Tower diameter bottom, top (m) | 6, 3.87 |
| Tower wall thickness bottom, top (m) | 35, 25 |
| Monopile diameter (m) | 6 |
| Monopile wall thickness (mm) | 60 |

Therefore, the use of a simplified analysis was judged sufficient for the purpose of this study. However this simplification could be overcome by inserting non-linear waves to replace the large waves linear wave theory, for instance, by using the approach proposed by Hallowell at al. [141].

The NREL 5MW OWT was not designed specifically for either site used in this study, therefore the fragility values should not be expected to match those derived for a OWT design based on the site hazard conditions, such as those derived by Hallowell et al. [114].

## 4.3 Fragility analysis

### 4.3.1 Random variables modelled

The uncertainty introduced into the response of the case study OWT by using numerical models is captured by defining the random variables shown in Table 4.4 and used in Eq. (4.5) to (4.12). For each random variable, Table 4.4 provides the probability model and its parameters, e.g., the mean value and the Coefficient of Variation (CoV) (the ratio of the standard deviation to the mean). The list includes variables associated with the models and materials. The distribution types and moments are taken from published studies, based on either engineering judgement or empirical data. The random variables denoted $X$ mostly take the form of multiplicative factors that are used to scale either the demand or capacity term in the limit state, as seen from Eq. (4.5) to (4.12) in Table 4.4. Other random variables relate to uncertainty in the material properties.

As discussed above, the simulation assumes that the wind turbine is parked; the initial azimuth angle of the rotor will therefore influence the loading on the blades, as the wind profile is not constant over the height of the OWT. However, it is not known what position the rotor will stop in, so azimuth is modelled as a random variable with a uniform distribution between 0° and 180° (an upper limit of 120° could also be used due to symmetry of the rotor). Additionally, misalignment between the incoming wind flow and

the turbine rotor will impact loading. The IEC recommends assessing up to 15° yaw error; and a recent study of Morato et al. [136] assessed 8° yaw misalignment. However, no data was available to determine a distribution; in its absence, a uniform distribution was assumed based on engineering judgement with limits -8° to 8° adopted here following [136]. The environmental load models utilise inverse Fourier transforms to convert stationary frequency spectra into random time signals. In this context the random variable is the random seed used to generate phase angles used in the transform. Unlike the multiplicative factors, these random variables directly impact the structural calculation and are inputs to FAST.

### 4.3.2 Limit-state definition

A limit state defines the conditions beyond which a component no longer satisfies one of its performance requirements. The focus in this chapter is on

**Table 4.4:** Random variables used to capture uncertainty in demand and capacity. The distribution properties for variables with a uniform distribution, in square brackets, are the upper and lower limits. *Note - an azimuth of 0° indicates that blade 1 is pointing directly upwards.

| Type | Parameter | Mean | CoV | Distribtuion | Ref |
|---|---|---|---|---|---|
| Model uncertainty | Structural dynamics ($X_{dyn}$) | 1 | 0.05 | Lognormal | [142] |
| | Simulation statistics ($X_{sim}$) | 1 | 0.10 | Normal | [105] |
| | Stress evaluation ($X_{str}$) | 1 | 0.03 | Lognormal | [105] |
| | Blade model uncertainty ($X_{\delta l}$) | 1 | 0.05 | Lognormal | [105] |
| | Critical load capacity ($X_{cr}$) | 1 | 0.10 | Lognormal | [105] |
| | Material model uncertainty($X_{mat}$) | 1 | 0.05 | Lognormal | [105] |
| Material | Steel yield strength, MPa ($F_y$) | 240 | 0.05 | Lognormal | [105] |
| | Steel Young's modulus, MPa ($E$) | $2 \times 10^5$ | 0.02 | Lognormal | [105] |
| | Concrete tensile strength ($X_{con}$) | 1 | 0.30 | Lognormal | [143] |
| Rotor | Blade 1 azimuth angle* ($X_{az}$) | [0°180°] | | Uniform | |
| | Yaw angle ($X_{yaw}$) | [-8°8°] | | Uniform | |
| Enviro-nmental | Wind phase angle ($X_{seed,wa}$) | [0 1] | | Uniform | |
| | Wave phase angle ($X_{seed,wi}$) | [0 1] | | Uniform | |

ULS failure of the OWT structural components, and to this end, failure of the tower, monopile, blades, or transition piece are assessed.

Failure in the ULS relates to exceedance of the maximum load carrying resistance [6]. These criteria are evaluated for the different OWT structural components independently, as described in the following sections. Failure is assumed to occur at the first exceedance of the structural capacity by the demand in an analysis time-series.

#### 4.3.2.1 Monopile and tower

Collapse of the monopile or tower is assessed using two different limit state models. The first is taken from the work of Sørensen et al. [105] where failure occurs when the maximum moment in the tower exceeds the cross-section plastic moment reduced by a factor calculated from the cross sectional properties and representing a linear relationship fitted to the Eurocode 3 buckling limit state [144] for a shell with normal quality fabrication tolerance:

$$G_{Mcr} = \frac{1}{6}\left(1 - 0.84\frac{\phi}{t}\frac{F_y}{E}\right)\left(\phi^3 - (\phi - 2t)^3\right)X_{mat}X_{cr}F_y - M_{ULT}\left(X_{az}, X_{yaw}, X_{seed}\right)X_{dyn}X_{sim}X_{str}. \quad (4.5)$$

Where $\phi$ is the component diameter $(m)$, $t$ is the thickness $(m)$, $F_y$ is the yield stress $(N/m^2)$, and $M_{cr}$ is the critical moment $(Nm)$. Additionally, $M_{ULT}(X_{az}, X_{yaw}, X_{seed})$ is the EDP, defined as the maximum bending moment obtained from the linear elastic structural analysis. The $X$ terms are variables which capture modelling uncertainty and $E$ is the Young's Modulus, both are defined on Table 4.4. For brevity the wind and wave seed variables have been combined into a single parameter $(X_{seed})$. Eq. (4.5) will be referred to as the $M_{cr}$ limit state for the remainder of the thesis.

The NREL 5MW is a large utility scale OWT, both the monopile and tower have a low thickness to diameter ratio and are non-compact according to the definition provided in DNVGL-OS-J101 Section 7.3.1 [145]. Additionally

they exceed the Eurocode Class 3 cross-section limits [146], indicating possible local buckling. As a result, the DNVGL steel buckling code [145] is used as the second limit state model, which uses von Mises stress as the EDP. The buckling resistance ($f_{cap,M}\left(F_y, \sigma_{VN,M}\right)$) is calculated using the provisions for local shell buckling in Section 3.4 of DNVGL-OS-J101 [145].

The column buckling check is only necessary in the case that a combination of the shell geometrical properties is larger than 2.5 times the ratio of the Young's Modulus to the yield stress:

$$\left(\frac{L_{ef} L_c}{i_c}\right) \geq 2.5 \frac{E}{f_y}. \tag{4.6}$$

Where $k$ is the effective length defined by the code (2.1 for a cantilever beam [145]), $L_c$ is the cylinder length and $i_c$ is the radius of gyration. For the monopile this limit was not violated as it is assumed to be fixed at the mudline, reducing the unconstrained length to the water depth. However, the tower does exceed this ratio, so the buckling resistance ($f_{cap,T}\left(F_y, \sigma_{VN,T}\right)$) is calculated using the provisions for column buckling in Section 3.8 of DNVGL [145]. These were found to be the most onerous provisions. Both capacity variables are time-variant because the buckling strength is dependent on the stress state within the component; however, it is demonstrated later in the chapter, that this variability is small. Structural demand is calculated by transforming the force and moment outputs from FAST at each time step into stresses using a membrane shell calculation [145]:

$$\sigma_{Mem} = \sigma_{Ax} + \sigma_{Bm} \tag{4.7}$$

$$= \frac{N_{Ax}}{2\pi\phi t} + \left(\frac{M_{FA}}{\pi\phi^2 t} sin(\theta_{CS}) - \frac{M_{SS}}{\pi\phi^2 t} cos(\theta_{CS})\right) \tag{4.8}$$

Where the membrane stress in the shell ($\sigma_{Mem}$) is a summation of the axial stress ($\sigma_{Ax}$) and the membrane stress due to bending moments ($\sigma_{Bm}$) acting on the cross-section. The axial stress is the applied axial force ($N_{Ax}$)

divided by the beam cross-sectional area. The stress due to bending moments is the fore-aft ($M_{FA}$) or side-to-side moment ($M_{SS}$) evaluated at a location around the beam cross-section ($\theta_{CS}$). This approach assumes that torsional and bending forces within the shell are negligible.

The DNVGL limit state is also considered for both the tower ($T$) and monopile ($M$), Eq. (4.9):

$$G_{DNV,T} = f_{cap,T}\Big(F_y, \sigma_{Mem,T}\Big) \cdot X_{cr} - \sigma_{Mem,T}\Big(X_{az}, X_{yaw}, X_{seed}\Big) \cdot X_{dyn} X_{sim} X_{str} \tag{4.9}$$

$$G_{DNV,M} = f_{cap,M}\Big(F_y, \sigma_{Mem}\Big) \cdot X_{cr} - \sigma_{Mem,M}\Big(X_{az}, X_{yaw}, X_{seed}\Big) \cdot X_{dyn} X_{sim} X_{str}. \tag{4.10}$$

The variables are the limit state functions ($G_{DNV,T}$ and $G_{DNV,M}$), the tower cross-section stress at each time step ($\sigma_{Mem,T}\Big(X_{az}, X_{yaw}\Big)$), and monopile cross-section stress at each time step ($\sigma_{Mem,M}\Big(X_{az}, X_{yaw}\Big)$).

It should be noted that the monopile limit state is evaluated at the mudline only, as the shell is uniformly thick, and the largest moment occur at this location. The tower code check is conducted along the height of the tower as the cross-section is tapered.

#### 4.3.2.2 Transition piece

A grouted connection is used to join the monopile to the transition piece. This transfers all moment, shear and dead weight forces acting on the tower/rotor into the monopile. Failure of the grout occurs at the interface between the grout and pile or transition piece and may result in the transition piece slipping relative to the monopile [147]. An analytical calculation for assessing grouted connections is provided by DNVGL [91]. The maximum grout tensile capacity ($f_{TP}$) can be calculated using the provisions in Section 4.5.1.13 of DNVGL-ST-C502. The maximum tensile stress demand ($\sigma_{TP}$) can be calculated using the analytical equation in DNVGL [91] Appendix C.1, the background to which is

provided by Lotsberg [147] (and includes experimental validation):

$$G_{TP} = f_{TP} \cdot X_{con} - \sigma_{TP}\Big(X_{az}, X_{yaw}, X_{seed}\Big) \cdot X_{dyn} X_{sim} X_{str}. \tag{4.11}$$

Where the $X$ terms are defined in Table 4.4. A tapered transition piece with no shear keys is assumed and, as discussed in Section 4.2.2.2, the structural properties were taken from Lee et al. [138].

#### 4.3.2.3 Blades

The blades convert wind flow into structural loading, and therefore failure of a blade would reduce the loads experienced by the other structural components. This effect has been observed in the failure of onshore wind turbines which have been exposed to typhoon winds [99]. The fragility of these components is noteworthy as it may impact the failure of the other structural components. However, the blades are complex, they are geometrically complicated and are usually made by composite materials. Detailed FEA models are typically used to assess failure of the blades [148]. In lieu of this analysis, a simplified limit state based on maximum blade root flapwise moment is used. The limit state is defined as the blade flapwise moment capacity ($M_{cap}$) minus the blade flapwise moment demand ($M_{dem}$):

$$G_{bld} = M_{cap} - M_{dem}\Big(X_{az}, X_{yaw}, X_{seed}\Big) \cdot X_{dyn} X_{\delta l} X_{str}. \tag{4.12}$$

The flapwise moment capacity is 15,310 kNm and was calculated by Resor [137] using a detailed FEA analysis for the NREL 5MW OWT blades. The moment demand is directly output from FAST for each blade.

### 4.3.3 Fragility function estimation

A total of 400 10-minute time-domain simulations with different seeds and samples were run for each MRP value on Table 4.2 at each site. The number of simulations (i.e., 400) was selected so that a probability of failure of 50% could

be predicted with a CoV of 0.05. A study presented in Section 4.6.2 assesses the error introduced by using a sample of 400, and demonstrates the number could be reduced if the framework were applied in practice, where computational power is a concern. This results in a series of limit state evaluations at a discrete number of MRPs. The probability of failure for each OWT component at different MRP can be estimated using the relevant limit state function. In plain Monte Carlo simulation, an estimate of the probability of failure is simply the mean value of an indicator function $I(G \leq 0)$ which takes a value 1 when the relevant limit state function associated with one analysis run is negative (i.e. the structure is assumed to fail during that simulation):

$$p_f\Big(MRP_i\Big) = P\Big[G_i < 0 | MRP_i\Big] = \frac{1}{N_{samples}} \sum_{k=1}^{N_{samples}} I\Big(G_{i,k} \leq 0\Big). \tag{4.13}$$

In Eq. (4.13), $p_f(MRP_i)$ is the probability of failure at discrete samples of the MRP indexed by $i$ and $N_{samples}$ is the number of samples, 400 in this case. Where the fragility function Eq.(4.13) is used in the system reliability calculation Eq.(3.4) by firstly calculating the mean annual failure rate using Eq.(3.3) .

A continuous fragility function ($p_f(MRP)$) is fitted to the discrete sampled data, assuming that a lognormal CDF is capable of representing the samples probability of failure calculated using Eq. (4.13). This assumption, commonly used in the field of earthquake engineering, is a suitable parametric model for several civil engineering structures [125, 149]. The lognormal assumption regarding the shape of the fragility curve was confirmed using a Chi-Square Goodness-of-Fit Test, and the results are only reported when the hypothesis test failed.

The fragility fitting provides the median ($\hat{\eta}$) and logarithmic standard deviation parameters ($\hat{\beta}$) of the fragility function from which estimates of the probability of failure are evaluated, conditional on the IM ($p_f(MRP)$):

$$p_f(MRP) \sim \Phi(\hat{\eta}, \hat{\beta}, MRP) \tag{4.14}$$

.

The sets of MRP and corresponding probability of failures provide sample data; the fragility function parameters are selected using Maximum Likelihood Estimation (MLE) [150]. Specifically, the lognormal CDF parameters are selected using a two-step procedure: (1) the method of least squares is used to provide an initial estimate of the fragility function parameters; then (2) the maximum likelihood method is applied to refine the parameter estimation, where the samples are assumed to be binomially distributed, and the optimal fragility function parameters maximise the product of the binomial Probability Mass Function (PMF) at each of the $N_{MRP}$ MRP samples:

$$Likelihood(\hat{\eta}, \hat{\beta}) = \prod_{i=1}^{N_{MRP}} \binom{N_{samples}}{n_i} \hat{p}_f(MRP_i)^{n_i} \left(1 - \hat{p}_f(MRP_i)\right)^{N_{samples} - n_i}, \tag{4.15}$$

where $\hat{p}_f(MRP_i)$ is the estimated probability of failure at a given MRP using the estimated fragility curve parameters, $N_{samples}$ is the number of analyses (i.e., 400) and $n_i$ is the number of observed failures. This two-step approach is necessary because the MRP samples where all seeds fail (or survive) have narrow binomial mass functions. If the initial parameter estimates are not in the approximate region of the maximum likelihood solution, the logarithm of likelihood equation becomes numerically unstable.

The fragility function derivation is run in batches, with five different random variable configurations:

- X1 - Only randomness in the process through wind and wave time-series (i.e. the random variables labelled as Environmental in Table 4.4); all other variables are modelled as deterministic using their corresponding mean values.

- X2 - X1 plus model and material random variables, but not rotor random variables.
- X3 - All random variables modelled explicitly.
- X4 - X1 plus rotor random variables, comprising the azimuth and yaw angle.
- X5 - X1 plus only azimuth random variable.

The full fragility analyses were run three times, because adding the rotor random variables required rerunning the structural analysis model, resulting in a total of 19,200 time-domain simulations, for each site. This is necessary because the X1/X2 conditions assume a fixed azimuth and yaw angle whereas the X3/X4/X5 conditions require yaw and or azimuth angle to be modelled as random variables.

## 4.4 Fragility results

### 4.4.1 Influence of analysis length

There is value in assessing the impact of analysis length on fragility functions as a wide range of values, from 1.6 minutes [110] to 60 minutes [90], have been used in the literature to derive fragility functions from time-domain analyses (regardless of the hazard model). Figures 4.2 and 4.3 show fragility functions produced by selecting different averaging periods for the Ijmuiden (IJ) and Massachusetts (MA) sites using the X1 random variable conditions. Fragility estimates for longer analysis periods were calculated by combining the required number of 10-minute simulations. The results presented are for the tower and monopile $M_{cr}$ limit states only, however similar results were obtained for the other limit states. Larger analysis lengths shifted fragility functions to failure at lower MRP, as shown in Figure 4.2 and Figure 4.3. For instance, the IJ tower (Figure 4.2 (left)), the median reduces from $1.017 \times 10^5$ to $0.332 \times 10^5$ while the standard deviation reduces by 33% (from 1.42 to 0.94) when the 10 and 70 minute fragility curves are compared. In the limit of increasing

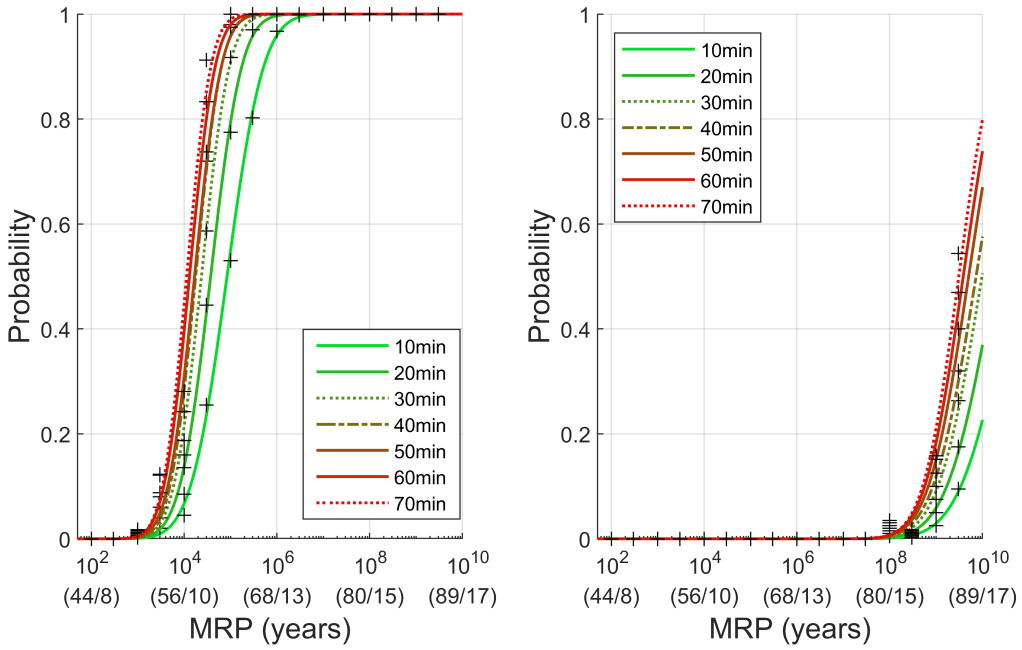


**Figure 4.2:** Comparisons of fragility functions produced for the tower (left) and monopile (right) of the NREL 5MW turbine at IJ. Different curves indicate different analysis lengths using the random variable condition X1. Brackets on the x-axis labels contain ($V_w$ (m/s) / $H_s$ (m)).

the analysis length the fragility function will approach a step function. If the environmental conditions are capable of inducing failure of the OWT this will be captured by every sample. The longer analyses therefore will have a smaller impact on the fragility function parameters as they approach this limit. Additionally, the proportional increase in the analysis length is much smaller for the long analyses. As the fragility function parameters are sensitive to the analysis length, one should explicitly account for the impact of analysis length on the fragility, otherwise bias will be introduced into the calculation of risk.

### 4.4.2 Influence of yaw and azimuth angles

The wind turbine enters its parked state at high wind speeds and the rotor stops rotating, but it is not known at what angle relative to the vertical position (for blade 1) the rotor will stop. Different rotor positions lead to different load patterns depending on whether a blade is pointing upwards (with increasing load along the length of the blade) or downwards (decreasing load along the

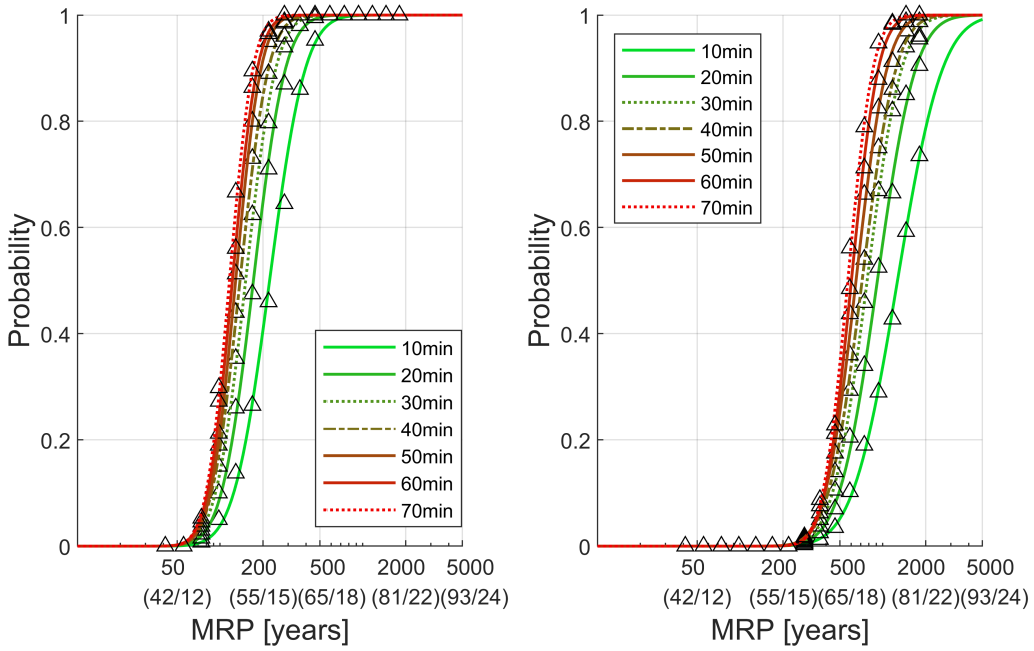


**Figure 4.3:** Comparisons of fragility functions produced for the tower (left) and monopile (right) of the NREL 5MW turbine at MA. The different curves indicate different analysis lengths using the random variable condition X1.

length of the blade) due to wind shear [82]. Additionally, there is the possibility of an error in the yaw mechanism, meaning that the control system will not be able to maintain a perpendicular angle between the plane in which the blades rotate and the direction of wind flow as it changes. Both of these effects have not been considered in existing wind turbine fragility studies, but have been observed to impact ULS loading [136]. Additional analyses were run to evaluate the the fore-aft bending moment at the tower base, mudline and blade root varies with these properties. The range of azimuth and yaw angles [-8° 8°] were split into a discrete series of 10-minute simulations repeated for 10 random seeds at each. The resulting changing loads are shown in Figure 4.4 (azimuth) and 4.5 (yaw) and are used to explain the fragility results.

When the azimuth angle is modelled as a random variable, using the X5 condition, changes in fragility function parameters are shown in Figure 4.6 (left). For example, comparing X1 to X5 conditions for the IJ monopile with DNVGL limit state leads to an unchanged location parameter and small

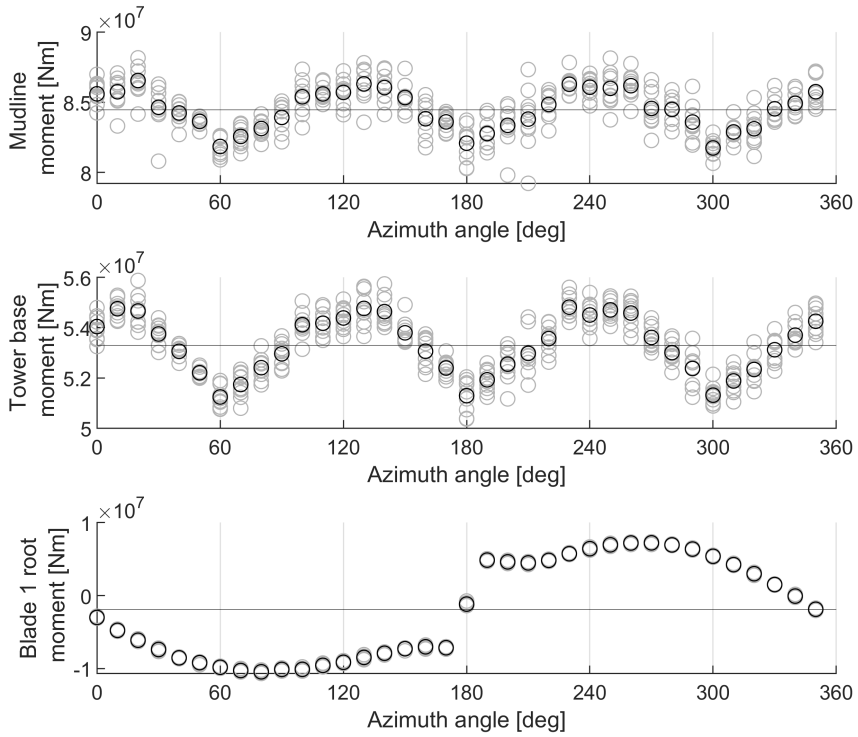


**Figure 4.4:** Comparison of load changing with azimuth angle at the mudline (top), tower base (middle) and blade 1 root (bottom). In each panel the mean moment is indicated by a horizontal line.

reduction in standard deviation (from 1.88 to 1.83, a 3% reduction). This can be understood from Figure 4.4, where the mudline and tower base moment are shown. A trend is visible whereby the moment is lowest when the rotor is in a position where one blade is pointing directly downwards (i.e., when blade 1 is at 60°, 180° and 300° from the vertical). The changing azimuth angle has a small impact on the coefficient of variation in loading which is 1.65% and 2.11% for the monopile and tower respectively, especially when compared to the $\sim 1\%$ caused by seed variability (shown as grey dots in Figure 4.4). This explains the small influence this parameter has on the fragility function. Azimuth angle has a larger impact on the blade loads, as shown in Figure 4.4 (bottom); only the results for blade 1 are presented for brevity (as the others followed the same trend with a 120° angle shift). A fixed azimuth means that each blade has the same load pattern for all seeds, whereas when azimuth is modelled as a random

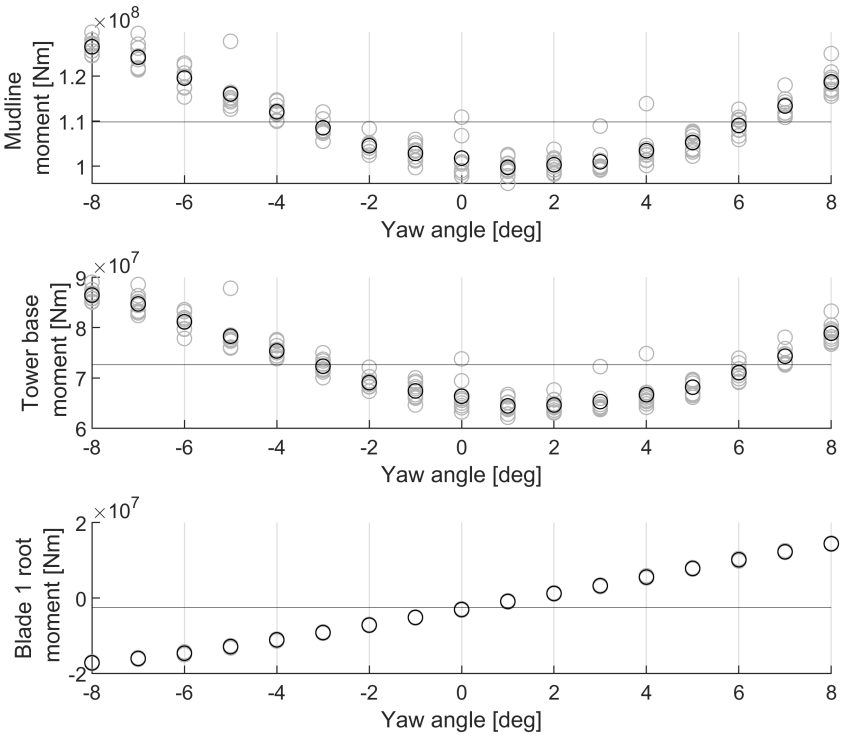


**Figure 4.5:** Comparison of loads changing with yaw angle at the mudline (top), tower base (middle) and blade 1 root (bottom). In each panel the mean moment is indicated by a horizontal line.

variable the load pattern changes. The loading will increase or decrease along the blade depending whether it is angled upwards or downwards relative to the hub. Therefore, over a sufficiently large random sample of the azimuth angle all blades experience approximately the same load pattern, because the azimuth angle is assumed uniformly distributed. As a result, the fragility functions for each blade in the X5 condition overlap, unlike the X1 fragility functions, Figure 4.6 (right). In this case a single fragility function could be used for the blades (i.e. which aggregates the individual results) whereas in the case where a single deterministic azimuth was used blades 1 and blade 2 & 3 have a distinct behaviour, see Figure 4.6 (right).

A similar deviation of changing load with azimuth angle was observed for the yaw error variable in the tower and monopile components, as in Figure 4.5. However, a continuous trend of increasing load with increasing yaw error

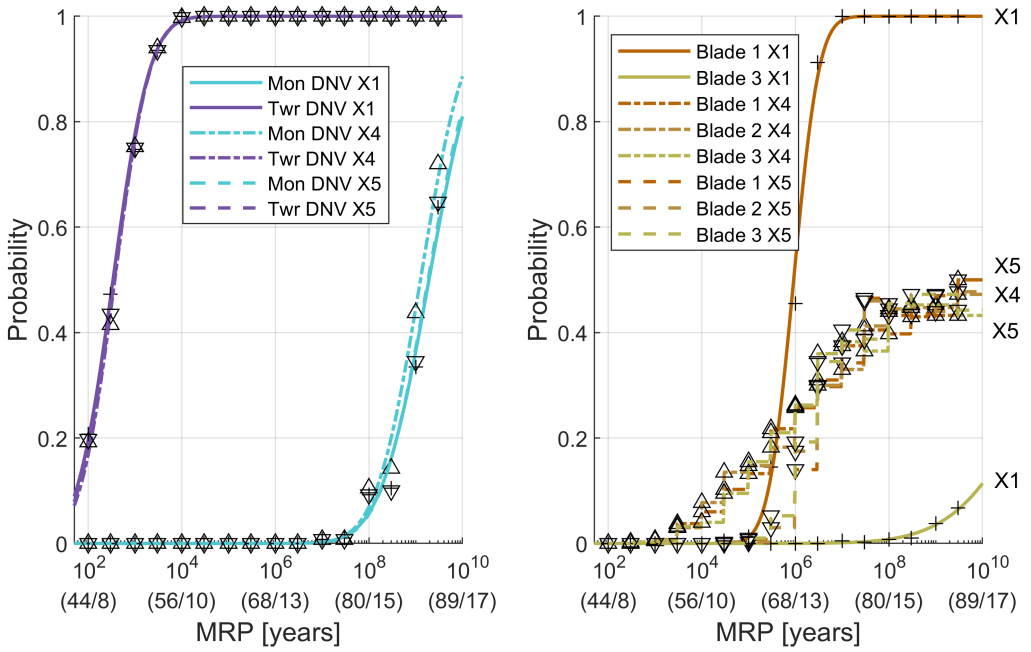


**Figure 4.6:** Fragility functions for the monopile and tower (left) and the blade (right) at the IJ site. Where the different random variable conditions are highlighted and 'Mon' represents the monopile and 'Twr' the tower.

is visible. The variation in loading only caused a small change in the tower and monopile fragility functions, see Figure 4.6 (left) for the X4 condition, e.g., for the monopile compared to the X1 condition the location parameter was constant and the standard deviation reduced (from 1.88 to 1.71, $\sim 10\%$). However, the limits on yaw error were enforced by applying the values from Morato et al. [136], and it would be expected that if a larger range of yaw error were used, the impact on the fragility function would be greater. In contrast, a noticeable impact was observed on the blade fragility, this is again a result of the larger impact yaw has on the blade root moment Figure 4.5 (bottom). For blades, inclusion of azimuth and yaw error increases the variation of the fragility function substantially in comparison to the case where neither is modelled (X1 condition) and this effect can be seen by comparing the X1, X4 and X5 fragility functions in Figure 4.6 (right). These results also suggest that an assumption of lognormal behaviour is not suitable for the blades when azimuth and yaw are modelled as random variable, this was confirmed by the results of

the Chi-Square Goodness-of-Fit Test which returned values in the range 0.21 to 0.53 (larger than the 0.05 significance threshold). In the remainder of this thesis they will be represented using an empirical CDF.

### 4.4.3 Influence of different random variables sets

The impact of including various random variables affecting OWT capacity (e.g., those representing material and modelling uncertainties, as summarised in Table 4.4) on the resulting fragility functions is investigated here. The results shown in Figures 4.7 and 4.8 demonstrate that, as expected, including model random variables changes the standard deviation of both limit states fragility functions by a similar amount, but has little impact on the location of the curve. Comparing the X1 to X3 condition for the $M_{cr}$ limit state at the IJ site results in a $< 3\%$ change in the mean and $\sim 22\%$ increase in the standard deviation (from 2.03 to 2.27). As discussed in the previous section, inclusion of the azimuth and yaw random variables have a small impact on the location of the tower and monopile fragility functions; this is visible in Figures 4.7 and 4.8 where the X1 and X4, and X2 and X3 conditions result in very similar fragility functions. For the blades, including model random variables (factors on the limit state equation) had very little impact on the fragility functions (see Figure 4.9). The yaw and azimuth variables are observed to dominate the response.

### 4.4.4 Site and component comparison

Comparing the results for different component limit states at the two sites allows an assessment of which are the most critical. The X1 conditions will be used in this section for clarity; however, findings are consistent across the various cases.

Due to the hurricane-type conditions, the Massachusetts site produces the most severe loading, resulting in relatively high probability of failure of the tower at low MRP. For instance, in Figure 4.8, probabilities of failure above 5% are observed between MRP of 50 and 200 years. At the Ijmuiden

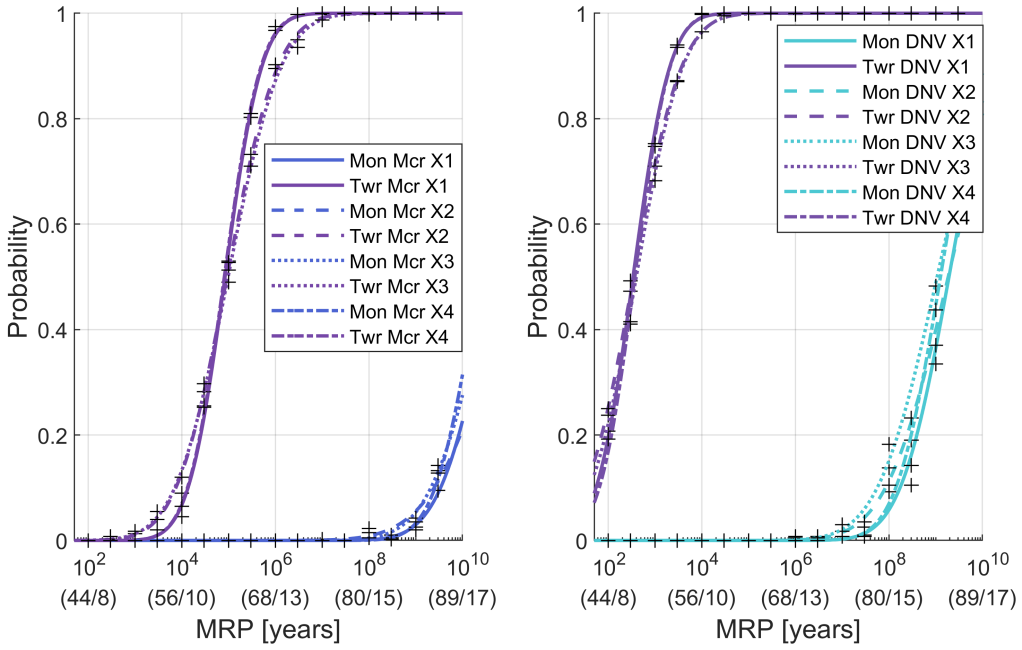


**Figure 4.7:** Comparison of the fragility functions produced for the tower and monopile of the NREL 5MW turbine at IJ using the $M_{cr}$ limit state (left) and the DNVGL limit state (right). 'Mon' represents the monopile, 'Twr' the tower.

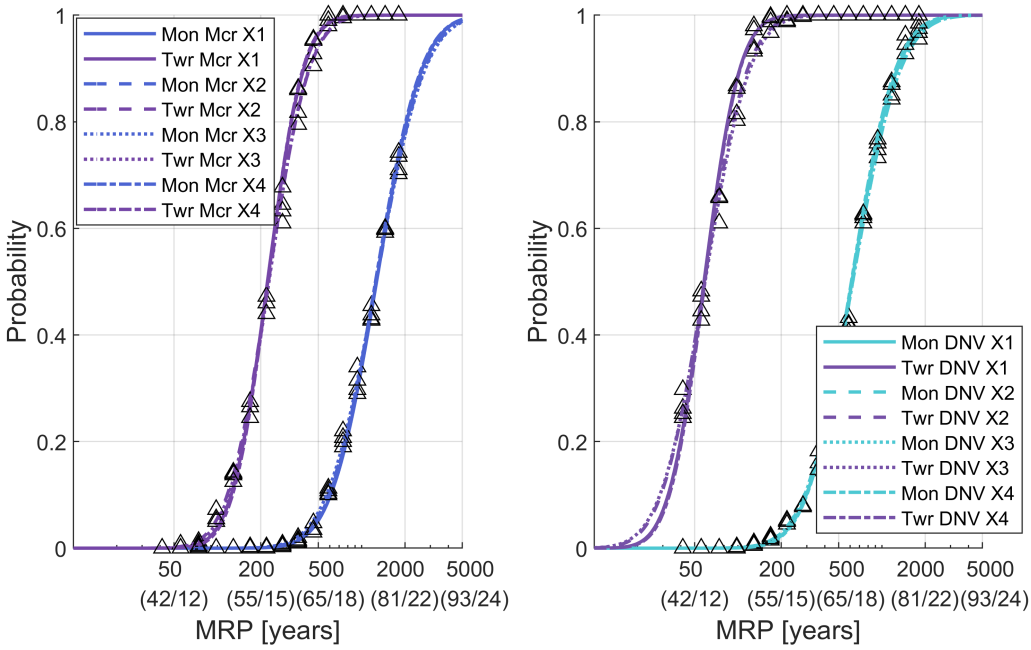


**Figure 4.8:** Comparisons of fragility functions produced for the tower and monopile of the NREL 5MW turbine at MA using the $M_{cr}$ limit state (left) and the DNVGL limit state (right). 'Mon' represents the monopile, 'Twr' the tower.

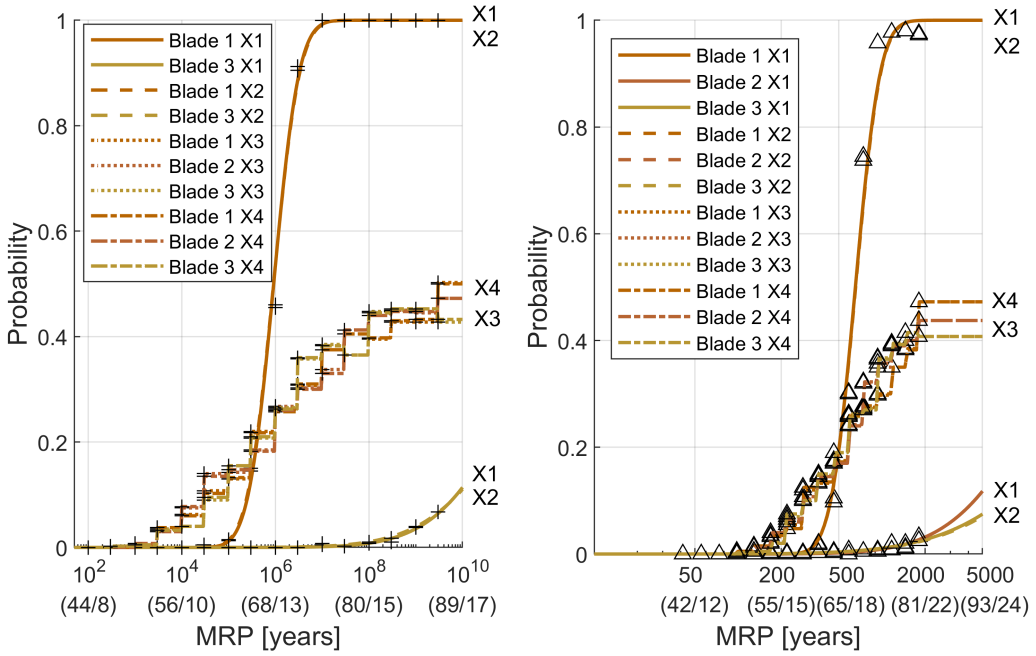


**Figure 4.9:** Comparisons of fragility functions produced for the blades of the NREL 5MW turbine at IJ (left) and MA (right) site.

site, the MRP range where most components fail with a probability of more than 20% is outside the bounds usually considered in a CAT model, which usually extend up to a MRP of 100,000 years.

The DNVGL and $M_{cr}$ limit states for the tower and monopile result in different fragility, with the $M_{cr}$ limit state causing failure at higher MRP than the DNVGL limit state. This is particularly visible in the case of the tower and monopile fragility for IJ site, Figure 4.10 (right), and can be justified by looking at the limit states in more depth. In Figure 4.11, the moment capacity predicted using different limit states are compared, with the DNVGL limit state converted into an equivalent bending moment using a membrane stress calculation. The small variations in DNVGL capacity are caused when the von Mises stress approaches 0, which affects the characteristic buckling stress. As discussed in Section 4.3, the $M_{cr}$ limit state is calculated by subtracting a factor from the cross-section plastic moment to provide a linear relationship approximating Eurocode 3 [144]. For the NREL 5MW OWT the reduction factor is approximately 0.1. Therefore, using the $M_{cr}$ limit state, failure of

the monopile will occur well above the point at which the outer fibre of the cross section first yields. On the other hand, the DNVGL local buckling limit state is calculated by dividing the yield stress by one plus the slenderness ratio to the power of 4, it will always be less than the material yield stress, and therefore represents a more conservative failure. The column buckling limit state is based on a similar process of reducing the buckling strength. This explains why the fragility function is shifted to lower MRP when the DNVGL limit state is used. It is notable that there is no overlap between the monopile and tower fragility functions for any of the random variable sets. This indicates that in all cases, the tower is observed to fail before the monopile.

Violation of the transition piece limit state was found to occur at MRP greater than 500 years, this is higher than both the tower and monopile for the MA site, Figure 4.10 (left). In contrast, no failures in this limit state were observed at the Ijmuiden site. This indicates that, particularly when using the more conservative DNVGL limit state, the transition piece is unlikely

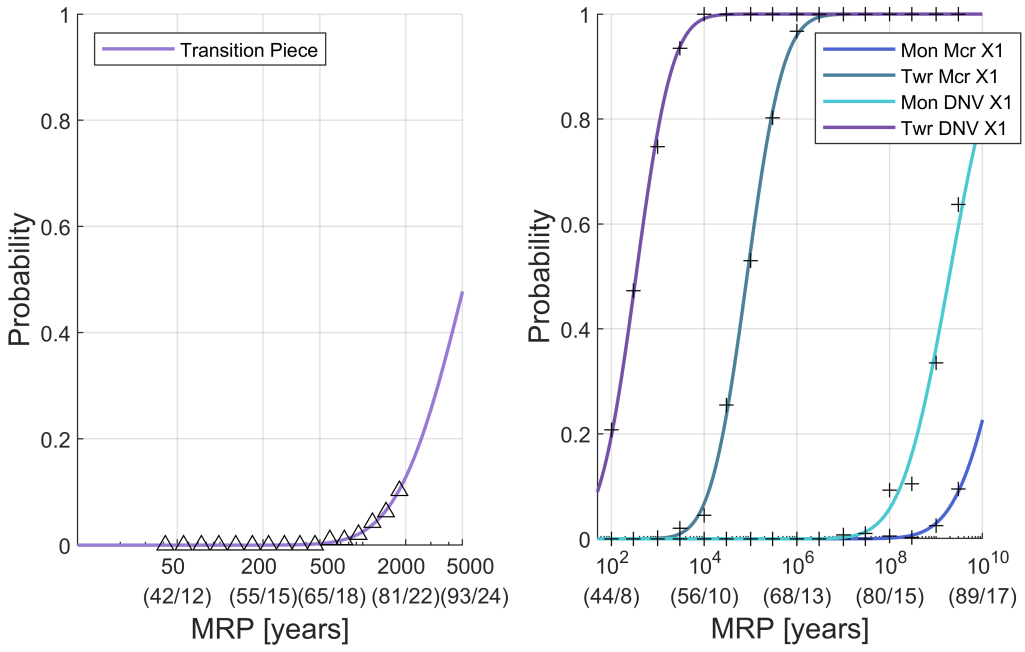


**Figure 4.10:** Fragility function for the transition piece at the MA site (left), and comparison of monopile and tower limit states at the IJ site (right). 'Mon' represents the monopile, 'Twr' the tower.

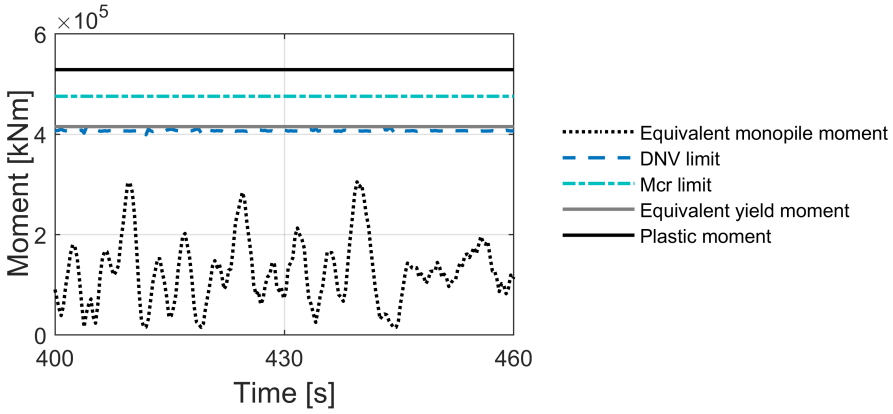


**Figure 4.11:** Comparison between the monopile limit states, all stresses converted into an equivalent bending moment. Graph is a segment from a full 600s time-series run at a MRP of $3 \cdot 10^7$

to contribute to failure of the OWT in the ULS, as failure in the tower or monopile limit states was observed to always occur first. However, it should be noted that only one OWT geometry is used in this work, and the transition piece geometry are taken from academic research, not current industry practice (where bolted transition pieces are sometimes used in preference to the grouted connection assumed in this study).

Fragility results for blade failure at both sites is shown on Figure 4.12 and indicate that failure of blade 1, the blade with largest demand (i.e. pointing upwards) for the X1 conditions, occurs at higher MRP than would cause failure of the tower. However, as discussed in Section 4.4.2, fragility of the blade is sensitive to modelling decisions. When azimuth and yaw are random variables the failure of all blades is equally likely and occurs at lower MRP than in the deterministic case. When using the rotor random variables there is overlap between the tower and blade fragility functions (visible in Figure 4.12). This indicates that the interaction between blade and tower failure hypothesised by Chen et al. [99] is plausible. Failure of the blade may reduce loading on the tower and therefore potentially prevent its failure. However, the tower fragility function are generally decisive as they occur at lower MRP, indicating that failure of the tower independently remains the most probable scenario.

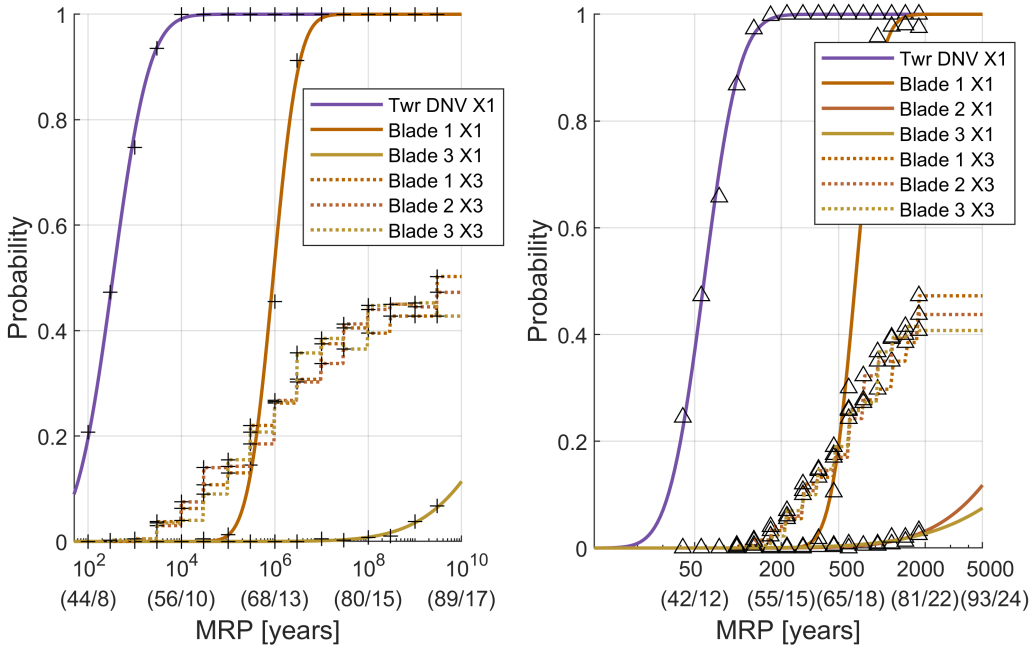


**Figure 4.12:** Fragility function for tower and blade limit states at the MA site (left), and fragility functions for tower and blade limit state at the IJ site (right). Where 'Twr' represents the tower.

### 4.4.5 Conclusion

The analysis length was found to effect both median and standard deviation of the fragility function for all components. However, this value should be selected to be consistent with the hazard model. The yaw and azimuth were found to only have a large impact on the blades, and modelling these effects is considered to be more realistic, as in reality the angle at which the blades stop will be unknown. In contrast the choice of other random variables in the limit state equation were found to have a small impact on the standard deviation of the fragility function for all components. Site and limit state were found to have the largest impact on fragility functions, this was particularly visible for the structural components where a large shift between the DNV and Mcr limit state was observed.

## 4.5 Loss analysis

### 4.5.1 Loss model

The structural components included in the loss calculation are the tower and blades, as the monopile and transition piece were observed to always fail after the tower had reached 100% probability of failure in Section 4.4. The replacement cost for the tower is estimated through a parametric equation described in Section 4.5.2. Data for the non-structural components of the OWT (and the replacement costs for the blades) are taken from the work of Carroll et al. [10]. They analysed data from maintenance records of ∼350 OWTs ranging from 2MW to 4MW in European waters and presented the results for different components. In this work, we focus on severe failures associated with either major repairs or full component replacement, and not on routine maintenance tasks. Only the failure rates for the top nine components in terms of replacement cost, out of a total of 19 sub-systems, are used in this work, shown in Table 4.5. The costs have been rounded to the nearest €1,000, to improve computational efficiency when evaluating Eq. (3.4) numerically, so that step sizes of €1,000 could be used.

The different failure conditions considered in this study are shown in Figure 4.13, which presents the scenarios considered through an event-tree diagram. The equipment is lumped together, as the failure of these components is assumed to have no impact on the failure of other components. Based on Figure 4.13, it is assumed that if the blades fail, the wind loads on the tower reduce (as blades are the main source of aerodynamic loading) and, as a consequence, the tower may survive. This simplified assumption tests observations about the failure of onshore wind turbines exposed to typhoon conditions [99]. However, it should be noted that a blade may impact the tower if it breaks first. If the blades survive but the tower collapses, it is assumed that all equipment and the blades fall into the sea and are damaged.

**Table 4.5:** Material cost for major replacement and failure rate of OWT components. [1]Eq. (4.16) with data - $[P_WT = 5\text{MW}]$.

| Source of cost data | Component | Major replacement (€) | Failure rate (/turbine/year) |
|---|---|---|---|
| Carroll [10] | Gearbox | 230,000 | 0.154 |
| | Hub | 95,000 | 0.001 |
| | Transformer | 70,000 | 0.001 |
| | Generator | 60,000 | 0.095 |
| | Circuit breaker | 14,000 | 0.002 |
| | Power supply | 13,000 | 0.005 |
| | Pitch system | 14,000 | 0.001 |
| | Yaw system | 13,000 | 0.001 |
| | Controller | 13,000 | 0.001 |
| | Blades (x3) | 270,000 | MA: $9.89 \cdot 10^{-4}$<br>IJ: $2.32 \cdot 10^{-5}$ |
| Parametric equations | Tower | 770,000[1] | MA: $4.97 \cdot 10^{-4}$<br>IJ: $8.36 \cdot 10^{-5}$ |
| | Total cost | 1,562,000 | |

### 4.5.2 Structural failure cost

Total OWT cost ($c_{WT}$) in k€, including blades and drive-train but excluding foundations, was estimated using a parametric equation. It represents a relationship between cost and the rated power of the turbine ($P_{WT}$) in MW which was fit to data from real OWT at seven different power ratings, 2MW through to 5MW [151]. This was converted into Euros (from Pound Sterling) by Dicorato et al. [152] resulting in:

$$c_{WT} = 2.95 \cdot 10^3 \cdot ln(P_{WT}) - 375.2. \tag{4.16}$$

Analysis by NREL [153] reported that the cost of an onshore wind turbines tower comprised 17.6% of the total turbine cost. The cost of the OWT tower is calculated by factoring down the wind turbine cost to 17.6% of $c_{WT}$, assuming consistency in the relative cost between onshore and OWT components. Information about the specific cost of OWT towers would improve this calculation. However, the comparison between structural and mechanical /

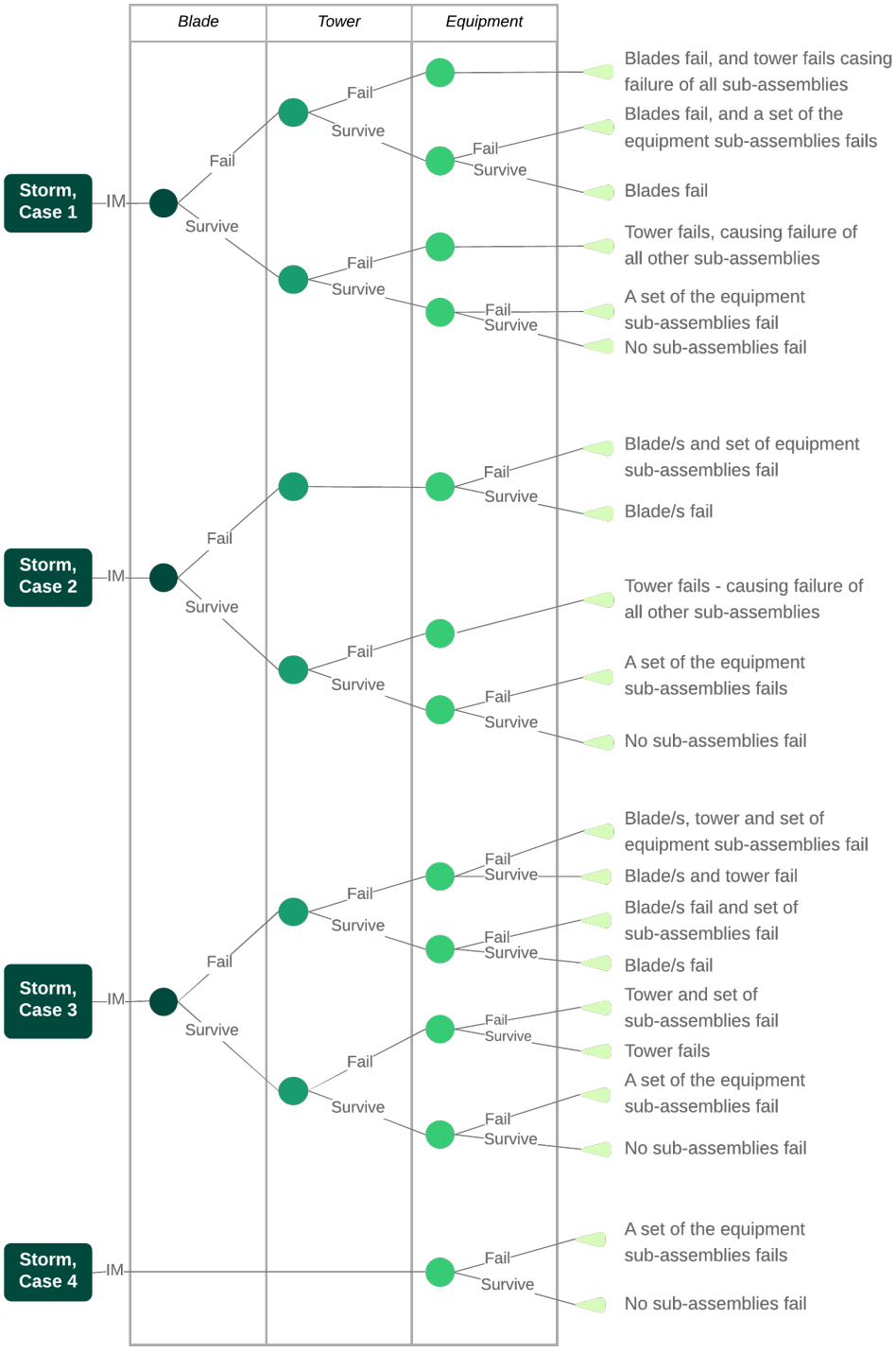


**Figure 4.13:** Event trees for an OWT that combines structural and equipment components. The analysis case corresponding to each event tree is labelled.

electrical components presented in this study only relies on the tower being more expensive than the other components.

## 4.6 Loss results

### 4.6.1 Fragility curves used in loss assessment

The fragility curve comparisons highlighted the impact of different modelling decisions on the fragility parameters at both sites. In the loss assessment the X3 random variable set is modelled. The tower component is represented using a parametric log-normal fragility curve and the blade using an empirical fragility curve (as the log-normal assumption was found to be a poor fit). All fragility curves used a total of 400 structural simulations ($N_{An}$) at each MRP to calculate the probabilities of failure in Table 4.6. These relationships are shown in Figure 4.14 for both sites.

The fragility calculation was implemented by assigning an indicator function to the output from structural analyses, run at each MRP. When the limit

**Table 4.6:** MRP with corresponding probability of failure and standard error for the monopile and tower.

| **IJ MRP** | **IJ $P_f$ Tower** | **IJ $P_f$ Blades** | **MA MRP** | **MA $P_f$ Tower** | **MA $P_f$ Blades** |
|---|---|---|---|---|---|
| 1.00E+02 | 0.000 | 0.000 | 4.13E+01 | 0.000 | 0.000 |
| 3.00E+02 | 0.000 | 0.002 | 5.55E+01 | 0.000 | 0.000 |
| 1.00E+03 | 0.003 | 0.005 | 7.40E+01 | 0.000 | 0.000 |
| 3.00E+03 | 0.013 | 0.034 | 9.79E+01 | 0.000 | 0.003 |
| 1.00E+04 | 0.100 | 0.059 | 1.29E+02 | 0.000 | 0.011 |
| 3.00E+04 | 0.370 | 0.113 | 1.68E+02 | 0.000 | 0.032 |
| 1.00E+05 | 0.803 | 0.143 | 2.19E+02 | 0.000 | 0.062 |
| 3.00E+05 | 0.975 | 0.204 | 2.82E+02 | 0.000 | 0.109 |
| 1.00E+06 | 1.000 | 0.265 | 3.63E+02 | 0.013 | 0.142 |
| 3.00E+06 | 1.000 | 0.323 | 4.63E+02 | 0.038 | 0.178 |
| 1.00E+07 | 1.000 | 0.366 | 5.88E+02 | 0.160 | 0.253 |
| 3.00E+07 | 1.000 | 0.394 | 7.43E+02 | 0.428 | 0.291 |
| 1.00E+08 | 1.000 | 0.428 | 9.34E+02 | 0.778 | 0.338 |
| 3.00E+08 | 1.000 | 0.443 | 1.17E+03 | 0.958 | 0.379 |
| 1.00E+09 | 1.000 | 0.442 | 1.46E+03 | 0.998 | 0.400 |
| 3.00E+09 | 1.000 | 0.468 | 1.81E+03 | 1.000 | 0.439 |

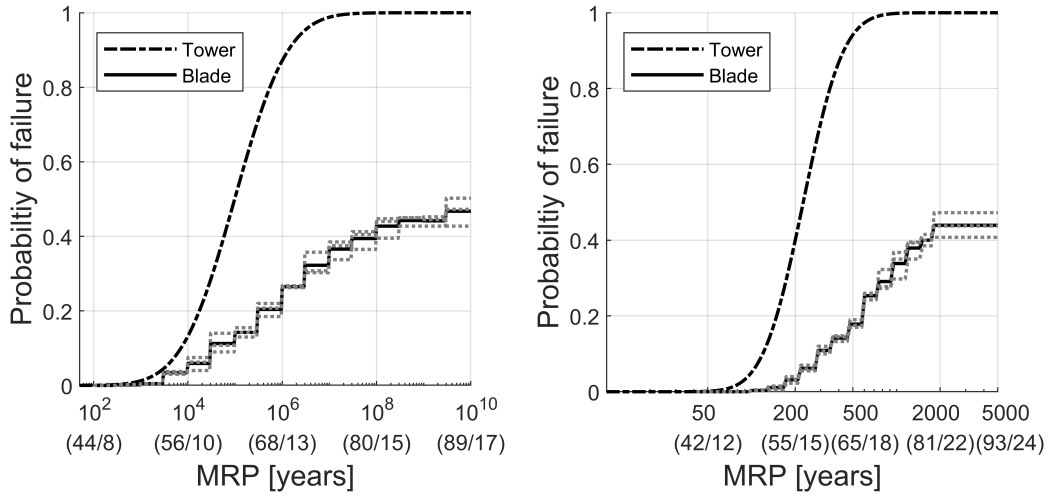


**Figure 4.14:** Fragility curves for the tower and blade at the IJ (left) and MA (right) site. The grey lines indicate the empirical fragility curves for individual blades and the black line indicates the expectation over the three blades.

state ($G$) was violated i.e., $I(G \leq 0)$, a value of one indicated that the structural component (tower or blade) failed during the simulation. A fragility function was fitted to discrete data providing a continuous prediction of the probability of failure conditional on the IM. In the case of the tower MLE was used to predict best-fit parameters of the lognormal distribution, the the lognormal mean $\mu_{LN}$ and lognormal standard deviation $\sigma_{LN}$. In the case of the blades, an empirical fragility curve (non-parametric) used previous neighbour interpolation between the 16 MRP analysed.

The results in the previous section were based on estimating the fragility function parameters through MLE based on a sample of structural simulations. This estimation is naturally associated with statistical error, and therefore there is uncertainty in the prediction of fragility function parameters, i.e. they will vary depending on the sample size. For this reason, a large number of samples were used in Section 4.4 (a single fragility curve requiring $N_{MRP} \cdot N_{An} = 6,400$ simulations). This is a fairly large number for many practical applications and therefore the loss assessment uses statistical resampling to assess the error introduced by using a reduced structural simulation

size. Epistemic uncertainty is assessed by sampling new sets of fragility data, with replacement, from the original set of analysis results. The impact of the uncertainty caused by a smaller sample size can be evaluated by quantifying the scatter in failure rates that results from scatter in the resulting fragility curve parameters.

The original set of indicator functions at each IM (size $N_{An}$) can be resampled with replacement for new, reduced number of analyses ($N_{An,Red}$). The impact of analysis sample size can then be evaluated by quantifying the scatter in the failure rate that results from scatter in the fragility curve parameters. An example of the variability in the fragility curves is shown in Figure 4.15 for the OWT blades at the MA site, comparing the original $N_{An}$ of 400 to a $N_{An,Red}$ of 50. It can be observed that for the larger sample, the scatter in the curves is reduced, however the mean prediction (bold black line) does not vary significantly.

### 4.6.2 Structural component yearly failure rates

The integral in Eq. (3.2) is solved numerically, over the range of MRP values bounded by the limits $MRP_i = [10, 10^6]$ and using a step size of 1 year. The failure rate is then calculated using each of the resampled fragility functions

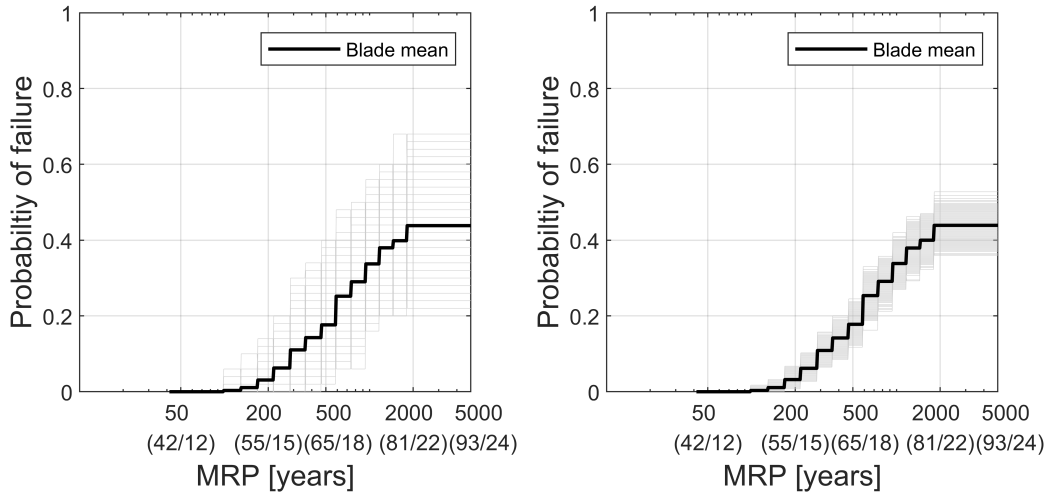


**Figure 4.15:** Resampled fragility curves shown in grey for the blades at the MA site. The number of samples used to calculate the probability of failure at discrete IM is 50 (left) and 400 (right).

(over a set of $50 \geq N_{An,Red} \leq 400$), resulting in scatter in the fragility function parameters. The mean annual failure rates are presented in Table 4.5, and the individual samples through histograms in Figure 4.16 for the IJ site and in Figure 4.17 for the MA site, using a small subset of the $N_{An,Red}$ sampled. These figures show the reduced scatter as the number of samples increases. The $N_{An,Red}$ sample size of 100 is used in remainder of this work (by fitting a lognormal distribution to the histogram using MLE) as the maximum coefficient of variation is around 0.5% (for the IJ tower).

### 4.6.3 Combined loss assessment

Loss estimation is initially implemented using the mean failure rates from Table 4.5. As discussed in Section 4.2, if any blade fails the loading pattern on the OWT will change (as the blades are the main source of aerodynamic loading). A simplified interpretation of this event is that if the blades fail the tower will be protected from failure through reduced loading. Conversely, if the blades survive but the tower collapses, it is assumed that all equipment and the blades fall into the sea and are damaged. To gain insight into the impact of these possible failure scenarios, four assumptions relating to failure of the OWT components are tested here:

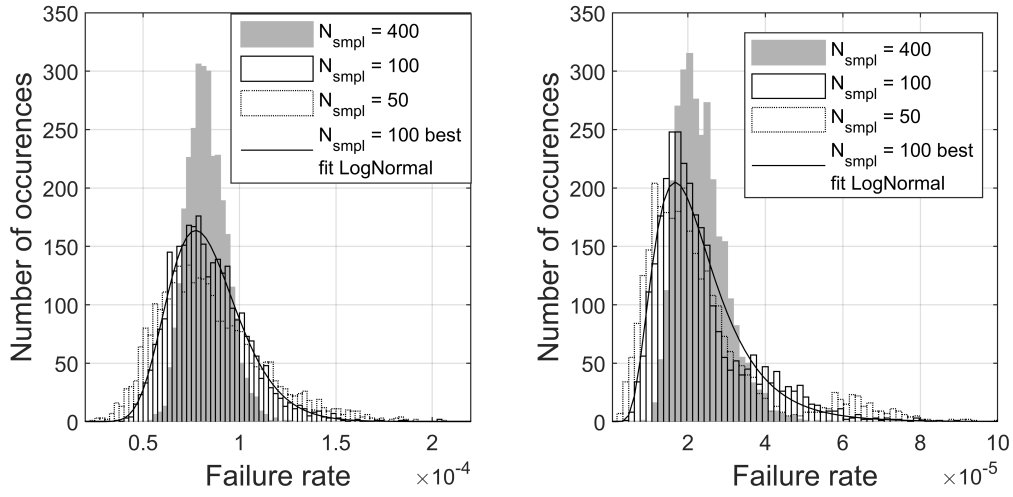


**Figure 4.16:** Histograms of failure occurrences for tower (left) and blades (right) for the IJ site.

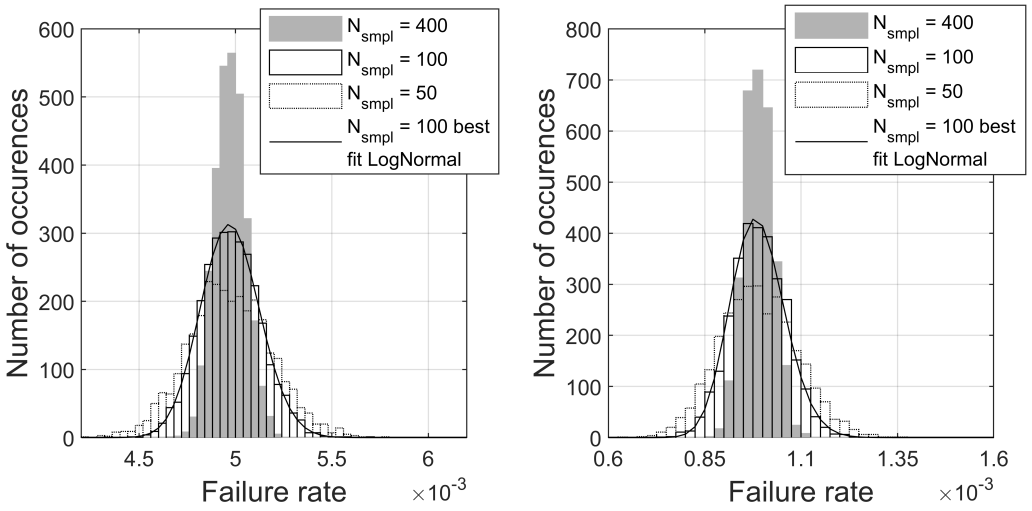


**Figure 4.17:** Histograms of failure occurrences for tower (left) and blades (right) for the MA site.

- Case 1: Tower and other failures are perfectly correlated - a new matrix $\boldsymbol{K}_1$ is generated where failure of the tower results in the failure of all other components.

- Case 2: Blade failure prevents failure of the tower - a new matrix $\boldsymbol{K}_2$ is generated. Firstly, failure events that include the blades are modified to prevent failure of the tower. Then the remaining cases where the tower fails (but the blades do not) cause the failure of all other components.

- Case 3: Uncorrelated components - the $\boldsymbol{K}$ matrix left unchanged.

- Case 4: No structural failure, only equipment components fail, and empirical failure rates from Table 4.5 are used.

These assumptions about the dependency between OWT components are encoded within the loss calculation by creating an updated matrix of failure events ($\boldsymbol{K}$). The updated matrix is used to evaluate which subset of failure events are used $\boldsymbol{k}^* \in \boldsymbol{K}_c$ at each cost level in Eq. (3.4). Events that include failure of the tower can be identified, and the indices relating to all other components modified to correspond to a failure state. In the case where blade failure prevents failure of the tower, events where the tower and blades fail

are first identified, then the tower component index is changed so that it survives. In the equipment only case, the probability of failure of the structural components is set to zero.

The annual loss Complementary Cumulative Distribution Function (CCDF) is shown in Figure 4.18 (left) for the IJ site and (right) for the MA site. These show that losses of individual OWT occur with relatively large probability driven by the more frequently occurring equipment failures, with annual probability of occurrence around 22% at both sites. Losses that also include structural components occur with annual probability of around 0.008% at IJ and 0.5% at MA, indicating the large difference in hazard between the two sites.

The failure case which excludes structural components predicts a maximum material costs well below €1M, which is the sum of all equipment material costs. All material costs higher than this include one of the structural components. Using independent components (Case 3) results in a range of failure costs that involve the tower, whereas the correlated failure cases only predicts a material cost that is the sum of all equipment and tower costs, €1,562,000 (Table 4.5). This is more accurate, as collapse of the tower will have consequences for all equipment in the hub. Differences in assumptions

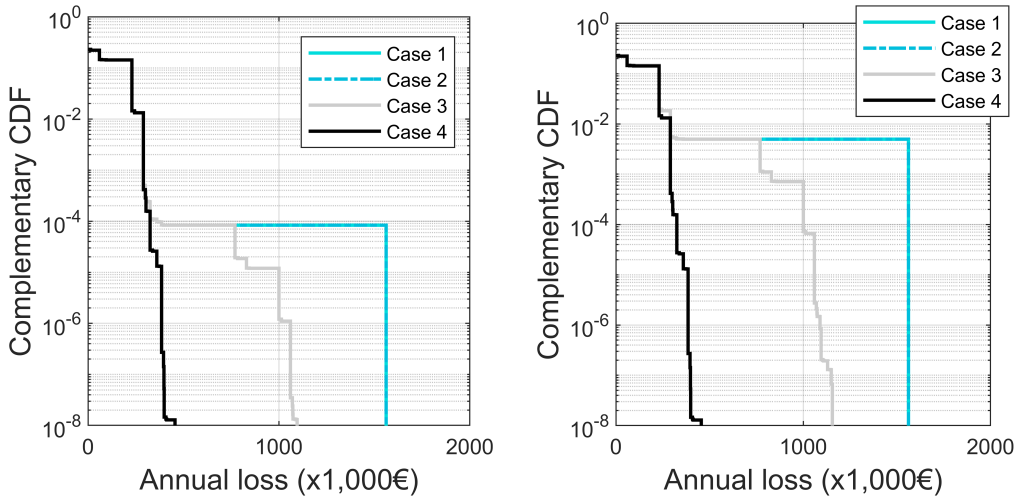


**Figure 4.18:** Loss CCDF comparing the four assumptions used in calculating loss at the IJ site (left) and MA site (right).

about blade failure (Case 1 and 2) do not have a visible impact, due to the rarity of blade failures in comparison to the tower at both sites. This is explained by Eq. (3.4), as for each set of failure events the yearly probability of occurrence is the product of the probability of failures (for components that fail) and probability of survival (for components that survive).

### 4.6.4 Annual loss distribution

Loss for the OWT is estimated using Eq. (3.5). Uncertainty in the structural failure rates can be included in the loss calculation by sampling the distributions describing failure rates of the blade and tower (i.e., Figure 4.16 and Figure 4.17) and using the random samples as input to Eq. (3.2). The resulting distribution of annual losses is shown in Figure 4.19. For IJ, little difference visible in the two cases where perfect correlation in the failure cases is assumed, the mean annual loss of both is €$3.87 \times 10^4$. The uncorrelated case is not conservative, because the average annual losses are lower, however the difference is only marginal as the mean Case 3 annual loss is €$3.86 \times 10^4$. Results for the MA site, Figure 4.19 (right), indicate that the structural components have a more important impact on annual loss. The Case 1 and 2 histograms both have mean annual loss of €$4.62 \times 10^4$, whereas the Case 3 (independent results) has a lower mean annual loss of €$4.25 \times 10^6$. This is due to the hurricane type conditions at the site, these differences emphasise the need for a site-specific approach to the structural components of OWT. This calculation can be scaled to the OWF by multiplying the losses from a single OWT by the number of OWT in the farm, assuming that all act independently.

The specific numerical results should be considered with caution, given the simplifying assumptions used in the illustrative application. However, the relative importance of the different analysis cases suggests that Case 1 provides a conservative estimation of annual losses.

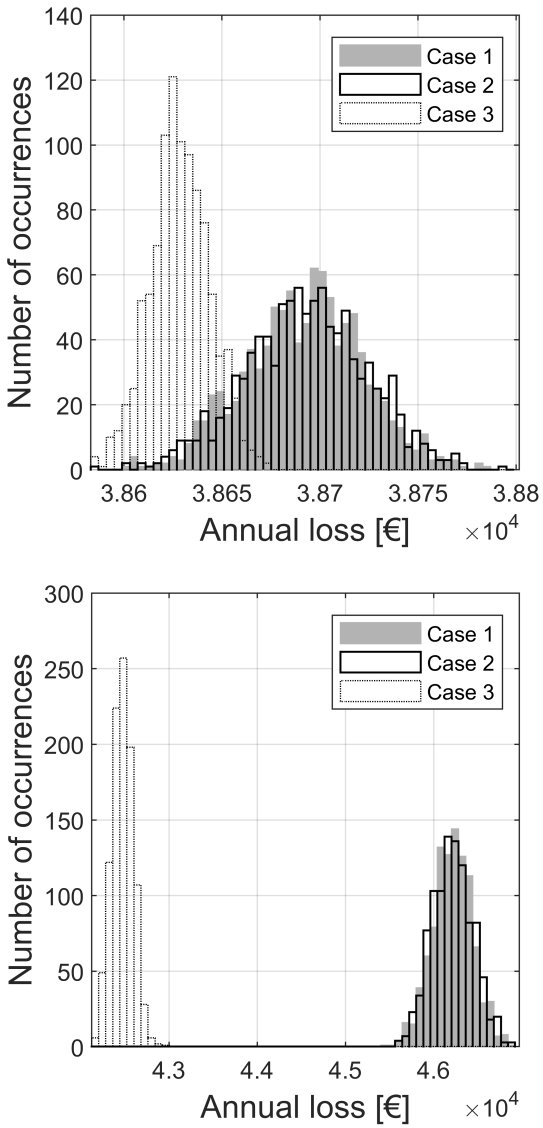


**Figure 4.19:** Histogram of annual loss for IJ (top) and MA (bottom) when uncertainty in the fragility function parameters is modelled.

## 4.7 Conclusions

The framework proposed in Chapter 3 for calculating financial losses associated with an OWT in the structural ULS was implemented for two case study OWTs. Uncertainty in the definition of fragility curves was explicitly included in this analysis by resampling the fragility function parameters. The resulting distribution of structural component failure rates was then included in the loss calculation using Monte Carlo sampling.

The fragility functions for the tower and monopile were found to depend on the limit state equation used to model failure. Consequently, the choice of a limit state that accurately describes the problem being investigated is important. For a large diameter utility scale OWT, the DNVGL limit state was found to be more conservative. Additionally, model uncertainties were found to have an important impact on all limit states, while the azimuth and yaw variables were only important for the blades. Other conclusions relating to the fragility curves include:

- The hazard model should explicitly account for the impact of analysis length on the fragility, otherwise as demonstrated, bias will be introduced into the risk calculation due discrepancy between analysis length and environmental averaging period.

- Overlap between the fragility functions for the blades and tower was observed, indicating that, in some instances, the blades may fail before the tower reducing loading. However in the loss calculation this was found to be of little consequence because of the low failure rate of the blades compared to that of the tower.

- The monopile and transition piece were found to fail at much higher return periods than the tower (or not at all in the case of the transition piece assessed at the Ijmuiden site), indicating that for the OWT geometry assessed these components are robust.

- For the Ijmuiden site, representative of European conditions, the OWT

was found to fail in the ULS at very high MRPs, which are out with the values typically included within a CAT model.

The case-study assessed an OWT comprised of both generation equipment and structural components. Although structural failure rates were low in comparison to the mechanical / electrical components, they are associated with very high financial losses (especially when it is assumed that structural failure also results in loss of the equipment). For this reason, they were found to have a notable impact on the annual loss at the MA site, where severe hurricane conditions occur. This highlights the site specific nature of the structure and emphasises the need to include details of site loading into risk calculation. The following chapters describe and approach for analysing the structural FLS, which may be the driving failure mode for OWT in European waters.

# Chapter 5

# Fatigue limit state loss framework

## 5.1 Introduction

The design of OWT sub-structures is currently specified by prescriptive codes, e.g., the IEC 61400-3 [6] or the DNVGL-ST-0126 [91], as summarised in Chapter 2. These codes implement the LRFD approach to attain a certain level of safety in the structural components. This is ensured by prescribing a wide range of load cases encompassing all environmental and operating conditions expected during the 20-25 year design life. Moreover, uncertainties affecting structural demands and capacities are accounted for by using partial safety factors, that are typically calibrated to ensure a desired level of structural reliability [154]. However, the current generation of partial safety factors used in the design of OWTs are a combination of those used in the offshore Oil & Gas industry and those used to assess onshore wind turbines [95]. They have not been specifically calibrated for OWTs and so the implied reliability level is unknown.

An essential step in understanding the suitability of the current partial safety factors is to perform explicit reliability assessment of OWT structural components, as this can help understanding the implied reliability levels. Additionally, this could allow OWT (sub-)structures to be optimised through an

explicitly probability-based design approach. Such a probabilistic-based design would provide a more rational and consistent design approach for fatigue assessment. To date, most reliability studies have assessed the OWT ULS, including the development and use of statistical surrogate models to improve computational efficiency of the assessment [155]. These studies have utilised fully-coupled time-domain simulations [95], which is considered the state-of-the-art technique for both design and assessment of OWTs [39]. Indeed, a method for assessing ULS failure using a probabilistic risk framework was developed in Chapter 3 and implemented for a case study location in Chapter 4. However, there is a limited number of studies employing reliability techniques to assess the FLS, which often drives the design of OWT sub-structures in European waters [156]. In fact, OWTs are especially vulnerable to fatigue damage. Highly irregular wind and wave loading combined with variable material properties make design against fatigue a challenging task, as fatigue damage is accumulated throughout the life of an OWT. An assessment of this limit state should include all the wind and wave conditions that are expected to be encountered during OWT operation and, therefore, should encompass a wide range of environmental conditions, requiring in the order of >50,000 time-domain simulations [39]. Current code provisions, such as IEC 61400-3 [6], allow the mean wind speed to be discretised into 2m/s bins and the analysis of a single combination of significant wave height and peak spectral period for each wind speed bin. However, this is a simplification, as the environmental parameters are better described by a joint-PDF, resulting in complex inter-dependencies between parameters [156]. Additionally, the code requires performing time-domain analyses, with at least 60-minutes of simulated time, for each set of environmental conditions; this is to ensures a stable estimation of damage accumulating over an OWTs design life. The large number of environmental conditions (and the need for time-domain analyses) makes the assessment of an OWT in the FLS computationally expensive and often prevents a full structural reliability assessment. Different approaches to managing

this computational burden are summarised in Section 5.1.1.

Motivated by the need to improve the computational efficiency of evaluating the FLS, this chapter introduces a probabilistic risk calculation for fatigue that relies on a surrogate modelling technique. This approach allows financial losses to be estimated for the FLS, thereby quantifying robustness. This approach follows the general framework shown on Figure 5.1. The specific steps are introduced in this chapter.

The fatigue limit state is introduced in Section 5.2, describing the uncertainties characterising fatigue life. The proposed approach also allows quantification of the variability introduced by modelling fatigue material parameters as random variables. GP regression is the selected surrogate modelling technique, and its characteristics are described in Section 5.3. An illustrative application, combining case-study environmental conditions with a representative OWT model is described in Chapter 6.

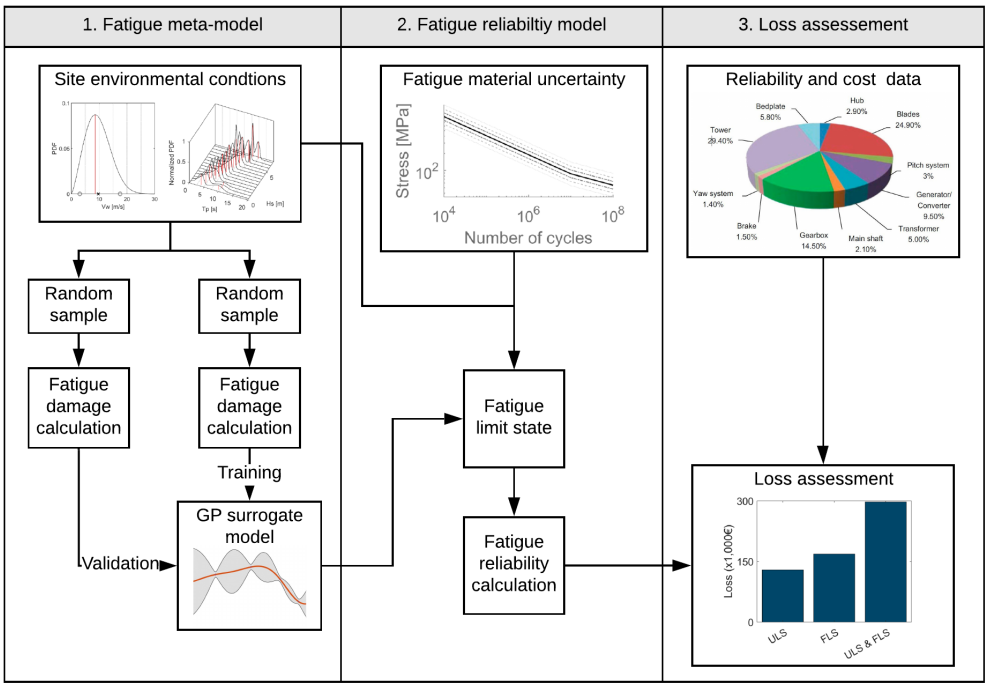


**Figure 5.1:** Framework for calculation of financial losses when the structural FLS combined with equipment components.

### 5.1.1 Analysis reduction for the fatigue limit state

The structural response of an OWT to environmental loading is commonly calculated using computer-based models or simulators, which are specified using a set of input parameters unique to the OWT and location specific environmental conditions. The response is predicted through a series of well established numerical relationships [11]. From a general, high-level perspective, a simulation tool for an OWT can be considered a "black box" which takes a vector of unique inputs ($\mathbf{x}$) and produces an output ($\mathbf{y}$) described by the relationship:

$$\mathbf{y} = h(\mathbf{x}) \tag{5.1}$$

The simple form of Eq. (5.1) means that the simulator can encompass a wide range of specific analysis procedures, i.e., any model that predicts the OWT response. In practice, time-domain simulations are most commonly used [39], where the response to various loads is evaluated at a series of discrete consecutive time-steps [157]. This technique can assess transient conditions caused by the turbine control system [80]. However, time-domain simulations are computationally expensive. Long simulation times are required by the current design codes - 60 minutes or more for each load case. Additionally, small time-steps are needed to ensure numerical stability and convergence in the time-stepping algorithm [17], further increasing the computational burden.

As discussed in the introduction, Section 5.1, current design codes for OWTs [6, 158] require assessment of a large number of load cases consisting of different environmental conditions, in an attempt to comprehensively assess all conditions that an OWT is expected to experience during its operating life. It is not computationally feasible to explicitly evaluate each load-case in the time-domain and also quantify uncertainty in the response through common sampling-based reliability analysis techniques (e.g., plain Monte Carlo method). This requires a method to reduce the computational burden of evaluating the FLS. Different solutions to this problem have fallen into two broad categories, either making the analysis more computationally efficient or reduc-

ing the total number of simulations required using:

- Load-case reduction;
- Surrogate models (simple and complex), also commonly referred to as meta-models or emulators;
- Simplified mechanical models, based on frequency domain simulations.

Load-case reduction attempts to mitigate the computational burden of evaluating the FLS, by reducing the number of load cases combining those producing similar outputs. This avoids using a statistical model to directly predict the response; but it means that the full set of structural simulations required to compute the FLS is required to calibrate the reduced set of load cases. This approach was first developed for application to OWTs by Kuhn [159]. It was based on a unidirectional scatter chart, originally consisting of 200 load cases, which were condensed into a reduced set of 21 load cases. The reduction was achieved by combining fatigue load cases resulting in similar damage estimates and linearly scaling the results of the new, composite, load case. A similar approach was used by Damgaard et al. [85], but the technique was extended to encompass multi-directional environmental conditions including wind and wave misalignment. Using a similar reduction criteria to Kuhn [159], a set of 1584 load cases was reduced to 200 with a reported error of less than 1% in terms of damage equivalent load (Design Equivalent Load (DEL)) [85]. Hafele et al. [160] reported similar results, reducing 2048 load cases into 210 equivalent load cases for an OWT located at a different site. In all the above examples, the number of load-cases were significantly reduced, by up to a factor of 10. However, the computational burden still remains large as the full set of load cases need evaluated in the first step of the procedure.

Surrogate models approximate complex systems, attempting to mimic their behaviour while being computationally cheaper to evaluate. Different surrogate models have been used to represent the output from complex structural analysis packages for OWTs by using a simple statistical model. Simple

linear meta-models are suitable for expressing a structural response quantity that is linearly related to the set of input variables $\mathbf{x}$. A simple model can also be adapted to non-linear problems by fitting multiple linear models over pre-defined ranges of the non-linear variable. Toft et al. [161] used models based on linear interpolation and linear regression to estimate the fatigue response of onshore wind turbines. Non-linearity arising from response of the turbine controller at different mean wind speeds was mitigated by fitting a separate interpolation function at 11 pre-defined wind speed bins. Zwick and Muskulus [103] fitted both a piece-wise linear regression and a linear statistical model to predict a fatigue damage curve for OWT (i.e., fatigue damage against increasing wind speed). The analysis was simplified by using a set of load-cases that had already been simplified with the load-case reduction technique developed by Kuhn [159]. However, the case of OWTs is different as they additionally respond non-linearly to wave loading [39]. Fitting separate surrogate models to wind and wave parameters may not be feasible.

Complex linear surrogate models can capture a large range of behaviours at the cost of complexity and specificity (i.e., the model may accurately fit the observed training data but not a new set of validation data). One highly-flexible type of surrogate model is regression built on the use of a GP, which provides a localised prediction of a simulators response based on the input training data. For instance, in the case of OWTs, Huchet et al. [162] found that a GP model was suitable for estimating the FLS using two input environmental variables, mean wind speed, and wind-wave misalignment. Similarly, Brandt et al. [163] used a GP model using wave height, wave peak spectral period, mean wind speed, wind turbulence, wind direction, and wave direction with small bias as model co-variates (i.e., predictors). A different approach was applied by Hafele et al. [164] who used a GP regression to represent post-processed fatigue damage against different geometrical parameters in an optimisation procedure for OWTs on jacket sub-structures. The GP regression has therefore been used in two different contexts: (1) direct representation of time-domain output

against environmental conditions; and (2) to represent analysis output post-processed into design-life fatigue-damage against properties of the turbine. The proposed GP models have been fitted to all parameters of a conventional scatter chart without introducing large model uncertainty.

Replacing the expensive aero-elastic time-domain model with a simplified mechanical model means that assessment of the OWT is much faster, allowing evaluation of each environmental load-case. One common approach is frequency domain calculation. The theoretical background to these models is summarised comprehensively by Baltrop [165] and Tempel [38], and so only a brief overview of the application to OWTs is provided here. Kuhn [159] developed an early simplified approach, where analysis of the OWT response to wind and waves is carried out separately, with the fatigue damage arising from both processes summed in the final stage. Tempel [38] developed a different approach by combining the separately evaluated response spectra directly before estimating fatigue damage. Similarly, Yeters et al. [116] and Ziegler et al. [166] developed variants based on decoupled frequency domain models. This approach has been applied in FLS reliability assessment by Marquez-Dominguez and Sørensen [167], Dong et al. [117] and Oest et al. [168]. These past studies all assessed the FLS using simplified mechanical models to estimate reliability of different OWT components. Muskulus and Schafhirt [90] developed a fatigue reliability model for OWTs on jackets sub-structures. This study included uncertainty in both the environmental loading (e.g., wind and waves) and material properties, but was not based on a fully-coupled simulation which are the current state-of-practice.

Based on the discussion above, load-case reduction does not provide sufficient savings in terms of computational effort to allow numerical sampling of structural analysis random variables. Simplified frequency-domain models are not commonly used in detailed design [80] as they do not capture the complex non-linear, coupled relationships that characterise OWT response, such as between the control system and mean wind speed. Surrogate models offer a

possible solution, by representing the structural response through a statistical model which is computationally efficient to sample. They also allow the use of advanced, detailed time-domain simulation techniques. Hence, these advanced statistical models are particularly relevant as they can represent various non-linearities in the structural response.

## 5.2 Fatigue damage limit state

### 5.2.1 Fatigue life estimation

Fatigue damage is cumulative [16], increasing over a structures operating life as it responds to randomly varying loads. In structural assessment, fatigue damage is commonly estimated by assuming that the number of load cycles to fatigue failure resulting from constant-amplitude loading ($N$) is a function of the applied stress range ($\sigma_r$); this relationship is described by an SN-curve [16]:

$$N = K_\mu \cdot \sigma_r^{-m} \tag{5.2}$$

The $m$-parameter is the slope of the SN-curve and $K_\mu$ is a constant determining the location of the $x$-axis intersection (i.e., on the number of cycles to failure axis). The ratio between the number of applied cycles and the tolerable number of cycles ($n/N$) is assumed "to consume" a fixed proportion of the fatigue life. Stochastic environmental conditions cause variable-amplitude loading comprised of multiple load cycles with different stress ranges. The total fatigue damage is assumed equal to the sum of the damage caused by each stress cycle, also known as Miners rule [16]. These assumptions result in the following equation,

$$D_j = \sum_{i=1} \frac{n_{ji}}{N_{ji}} = \frac{1}{K_\mu} \sum_{i=1} \frac{n_{ji}}{\sigma_{r,ji}^{-m}}, \tag{5.3}$$

in which Eq. (5.2) has been substituted for the $N_{ij}$ term, and $D_j$ is the total fatigue damage calculated over all the stress ranges (indexed by $i$)

occurring during a time-domain analysis conducted at a set of environmental parameters (indexed by $j$). The fatigue damage is then linearly scaled from the time-domain analysis length ($T_{analysis}$) to the life of the structure ($T_{life}$):

$$D_{j,life} = \frac{T_{life}}{T_{analysis}} \cdot D_j. \tag{5.4}$$

Fatigue damage can also be evaluated using the DEL:

$$DEL_{j,life} = \frac{K_\mu}{N_{eq}} \cdot (D_{j,life})^{1/m}, \tag{5.5}$$

which is the constant-amplitude stress causing the same fatigue damage as the variable amplitude loading at a reference number of tolerable cycles ($N_{eq}$) over the assessed time period.

A given structural component is assumed to fail when the fatigue damage reaches a pre-specified threshold, typically assumed equal to one. Equivalently, failure in terms of DEL occurs when the equivalent constant amplitude stress is larger than the SN curve stress at $N_{eq}$. For structures assessed using the DNVGL fatigue assessment code [100], failure predicted using the SN-curves corresponds to crack a growing through the thickness of the structures cross-section.

In order to calculate the stress range ($\sigma_{r,ji}$) and the number of applied cycles ($n_{ji}$) terms in Eq. (5.3), a structural simulation is run at a specific combinations of environmental parameters, from which the mudline stresses are extracted as time-series, as discussed later in Chapter 6. A rainflow counting algorithm is then used to post-process the time series [165] by extracting number of stress cycles at given magnitudes. These can be distributed into bins of a specified stress range, and the corresponding number of cycles in each bin can be counted, allowing fatigue damage to be predicted using Eq. (5.3) and Eq. (5.4).

### 5.2.2 Limit state definition

Assessing whether or not a structural component of an OWT is expected to fail due to fatigue during its operating life can be achieved by introducing a limit state (or performance) equation [64]. This is a relationship describing whether or not a structural component, or a structure, satisfies the performance objective defined by the limit state being assessed. It is assumed that failure occurs if the limit state function ($G$) assumes negative values. A fatigue limit state is defined in Eq. (5.6), where the performance of a structural component is parametrised through a capacity (or resistance, $R$) term and a structural demand (or load, $S$) term. Both demand and capacity depend on a set of random variables ($\mathbf{X}$), e.g., material properties, geometry and modelling uncertainty. The time dependence of fatigue loading ($t$) can be simplified by considering only the accumulated damage at the structures design life, making the problem time-invariant:

$$G(t,\mathbf{X}) = R(t,\mathbf{X}) - S(t,\mathbf{X}) \Rightarrow G_{Dlife}(\mathbf{X}) = R_{Dlife}(\mathbf{X}) - S_{Dlife}(\mathbf{X}). \quad (5.6)$$

In this case, structural demand and capacity are formulated directly in terms of fatigue damage; therefore, $R_{Dlife}$ is simply the tolerable fatigue damage before failure and $S_{Dlife}$ is the damage caused by stress cycles occurring over the structures life, across all environmental conditions, weighted by their probability of occurrence [169]. Lange [170] expressed $S_{Dlife}$, for onshore wind turbines, as a double integral of damage across an environmental variable ($e$) and stress ranges ($\sigma_r$), as in Eq. (5.7):

$$S_{Dlife}(\mathbf{X}) = \int_{e=0}^{\infty}\int_{\sigma_r=0}^{\infty} \frac{f_{\Sigma_r|E}(\sigma_r|e,\mathbf{X})}{N(\sigma_r,\mathbf{X})} f_E(e,\mathbf{X}) \cdot d\sigma_r \cdot de, \quad (5.7)$$

which includes the probability of an environmental variable ($f_E(e,\mathbf{X})$), for instance mean wind speed, and the probability of stress levels conditional on the environmental variable ($f_{\Sigma_r|E}(\sigma_r|e,\mathbf{X})$) divided by the number of cycles

to failure at each stress range ($N(\sigma_r, \mathbf{X})$).

For an OWT, a large number of environmental variables need to be considered within the limit state; this expands the order of the integral in Eq. (5.7). Calculation of the $f_{\Sigma_r|E}(\sigma_r|e, \mathbf{X})$ term requires reference to a dynamic structural calculation to estimate the occurrence of various stress cycles. The dependence of $f_{\Sigma_r|E}(\sigma_r|e, \mathbf{X})$ on $\mathbf{X}$ is also problematic as it means that the structural model will need to be rerun over the full limits of the integral with different samples of $\mathbf{X}$.

The limit state used in this study takes the same general form as Eq. (5.6) and Eq. (5.7). However, the load parameter, $S_{Dlife}(\mathbf{X})$ in Eq. (5.7), is computed numerically using Monte Carlo simulations across all environmental parameters and expressed as a single sum in Eq. (5.8) for simplicity. The integral over stresses in Eq. (5.7) is contained within the damage term $D_{j,life}$, which is estimated using GP regression:

$$G(X_\delta, X_{SN}) = X_\delta - X_{SN}\left[\frac{1}{N_{smp}}\sum_{j=1}^{N_{smp}} D_{j,life} \cdot Pr_j\right]. \tag{5.8}$$

The resistance term ($R_{Dlife}$) is simply equal to the damage tolerance ($X_\delta$) which is modelled as a random variable [100]. The GP surrogate model estimates the damage term ($D_{j,life}$) calculated assuming a continuous 20-year exposure to the environmental conditions over all samples of these conditions ($N_{smp}$). The predictions are weighted by the joint probability distribution over the environmental parameters ($Pr_j$) in order to evaluate the composite damage occurring throughout the operating life of an OWT.

An SN curve is typically fitted to measured data from experimental tests, which includes large variability. In fatigue design, the $10th$ percentile of the experimental data is typically used as a "design curve" and, therefore, designs according to this method include a large degree of conservatism, as indicated in Figure 5.2. This graph also shows SN curves resulting from taking different quantiles of the $x$-axis intersection, described by the assumed distribution ($X_K$). The $X_K$ distribution parameters are provided by DNVGL [100]. The

design curve $x$-axis intersection ($K_\mu$) is used in Eq. (5.3). The fatigue damage evaluated in Eq. (5.8) is normalized through multiplication by $K_\mu$ and then re-weighting by the random variable $X_K$. In Eq. (5.8) the notation is simplified by including the re-weighting inside the random variable $X_{SN}$ by: (1) calculating the reciprocal of $X_K$ and (2) evaluating the parameters of this distribution multiplied by a constant ($K_\mu$).

Additionally the tolerable damage, $x_\Delta$, is modelled as a random variable, as indicated in Table 5.1.

### 5.2.3 Reliability calculation

Uncertainty introduced by the considered random variables into the limit state equation, Eq. (5.8), can be evaluated using plain Monte Carlo simulation [171]. The estimate probability of failure, $P_f$, is the average over all the randomly

**Table 5.1:** Statistical properties of the random variables used to model the fatigue material behaviour.

| Random variable | Reference | Distribution | Mean of logarithm | Standard dev of logarithm |
|---|---|---|---|---|
| Tolerable damage ($x_\Delta$) | [100] | Log-normal | 0 | 0.3 |
| SN intersection ($x_K$) | [100] | Log-normal | 27.99 | 0.46 |
| SN uncertainty ($x_{SN}$) | N/A | Log-normal | -0.90 | 0.46 |

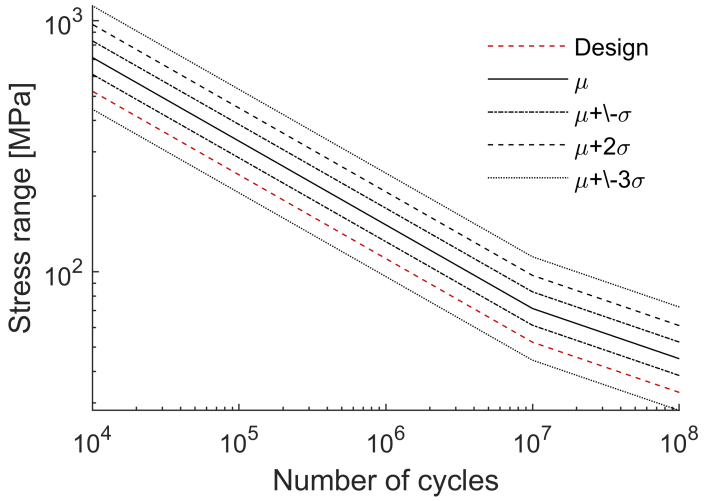


**Figure 5.2:** Scatter in SN curve when the full distribution of x-axis intersections are utilised. The 10th percentile curve, used in structural design, is highlighted as the mean curve minus two standard deviations.

generated samples, as expressed in Eq. 5.9:

$$P_f = \frac{1}{N_{LSsmp}} \sum_{i=1}^{N_{LSsmp}} I\Big(G_i(X_\delta, X_K)\Big), \tag{5.9}$$

where $N_{LSsmp}$ is the number of samples generated from the limit state equation and $I\Big(\cdot\Big)$ is an indicator function which takes a value of one if the limit state sample $G_i(X_\delta, X_K)$ is negative (i.e. the structural component/structure fails).

## 5.3 Gaussian process surrogate model

### 5.3.1 Surrogate models

As introduced previously, surrogate models mimic the behaviour of complex systems by predicting the value of some target variable given a combination of the input variables. The parameters defining the relationship between target and input variables are not known in advance. They are estimated from a training set of (observed) data, containing pairs of input (covariates) and output data. In the context of the FLS, the assumed target variable for this study is the fatigue damage (i.e., $D_{j,life}$) which depends on input variables ($\hat{\mathbf{x}}$), which include environmental variables such as mean wind speed or significant wave height. An estimate of the complex series of relationships represented by Eq. (5.1) is developed, which also includes some prediction error ($\epsilon$):

$$\hat{y} = \hat{h}(\hat{\mathbf{x}}, \mathbf{w}) + \epsilon, \tag{5.10}$$

where $\hat{h}(\hat{\mathbf{x}}, \mathbf{w})$ is a statistical model fitted to the outputs from structural analyses (for the training set) by finding the set of model parameters $\mathbf{w}$. The statistical model can be sampled directly, avoiding the need to refer back to the computationally-expensive time-domain structural simulations.

The surrogate model must fulfil two criteria. Firstly, it should accurately predict the fatigue loading of an OWT under a wide range of conditions that could be experienced during its operational life. Secondly, the error in the

surrogate model predictions should be quantifiable and small, so that minimal model uncertainty [172] is introduced into the subsequent reliability calculation.

The model must also be sufficiently adaptable to encompass all the variables that are important for predicting the OWT response. Previous sensitivity analyses by other authors on onshore and offshore wind turbines have identified a number of parameters that are relevant. The response of an OWT to wave loading was investigated by Ziegler et al. [173] for a monopile-supported OWT in 35m deep water. This study emphasised the importance of mean sea level and peak spectral period in fatigue damage. Hubler et al. [174] applied a four stage sensitivity analysis starting with 100 parameters - that covered a wide range of wind, waves, soil and geometrical properties - and concludes by ranking the 14 which have the greatest impact on FLS response. Each of the four successive steps filtered variables and used a more complex sensitivity analysis. This allows a full variance-based sensitivity analysis (with non-linearities and interaction effects) to be conducted in the final step on a reduced subset of parameters. For an OWT on a monopile substructure, mean wind speed ($V_w$), peak spectral period ($T_p$), significant wave height ($H_s$), wind direction ($\theta_{wind}$) and wave direction ($\theta_{waves}$) were the main parameters identified by the study and were not ranked in order of importance. Then, soil properties, marine growth thickness, pile dimensions and water depth were found to be important. Interestingly, turbulence intensity ($T_i$) was not on the final list of important parameters, but has been consistently highlighted as a critical environmental parameter in studies of onshore wind turbines [161, 175]. Brandt et al. [163] conducted a global sensitivity analysis for an OWT on a jacket and identified similar main environmental parameters to Hubler et al. [174], but found the FLS was insensitive to $\theta_{wind}$, $\theta_{waves}$ and yaw error, but was sensitive to $T_i$.

A number of parameters have been consistently identified as effecting the FLS and will therefore be used in this study. The main parameters from Hubler

et al. [174] were $V_w$, $H_s$ and $T_p$ with $T_i$, $\theta_{wind}$ and $\theta_{waves}$ are included in the proposed surrogate model as site environmental conditions.

### 5.3.2 Gaussian process regression

Regression techniques assume that observed data can be modelled using some mathematical function. Often, the shape of this underlying function is unknown, or the function might be hard to evaluate analytically. GP regression assumes this function takes the form of a stochastic process in which the target variables are jointly-Gaussian. In other words, a GP is a probability distribution over possible functions. This is a localised technique estimating responses as a weighted combination of the surrounding training points. It is a non-parametric Bayesian approach towards regression problems. It can capture a wide variety of relations between inputs and outputs by utilising a theoretically infinite number of parameters and letting the data determine the level of complexity through the means of Bayesian inference.

A GP defines a prior distribution over functions, which is converted into a posterior by conditioning on the training data. The act of conditioning allows a practical, finite-dimensional, model to be extracted from the infinite-dimensional process because the surrogate model reduces to a multi-variate Gaussian distribution through the marginalisation property of GPs. This is how, in a GP, the posterior can be derived from the prior and to observations. Consequently, estimates of the functions values ($\hat{y}$) corresponding to a new set of input variables ($\hat{\mathbf{x}}$) can be obtained by drawing samples from the obtained conditional distribution [176]. This multivariate conditional Gaussian distribution is fully defined by a mean vector ($\mu_{\hat{\mathbf{x}}}$) and a covariance matrix ($\Sigma_{\hat{\mathbf{x}}}$):

$$Pr\Big(\hat{y}|\hat{\mathbf{x}},\mathbf{x},\mathbf{y}\Big) \sim \mathcal{N}(\mu_{\hat{\mathbf{x}}},\Sigma_{\hat{\mathbf{x}}}), \tag{5.11}$$

$$\mu_{\hat{\mathbf{x}}} = \mathbf{k}_{\hat{\mathbf{x}},\mathbf{x}}\Big(\mathbf{k}_{\mathbf{x},\mathbf{x}} + \sigma_n^2\mathbf{I}\Big)^{-1}\mathbf{y}, \tag{5.12}$$

$$\Sigma_{\hat{\mathbf{x}}} = \mathbf{k}_{\hat{\mathbf{x}},\hat{\mathbf{x}}} - \mathbf{k}_{\hat{\mathbf{x}},\mathbf{x}}\Big(\mathbf{k}_{\mathbf{x},\mathbf{x}} + \sigma_n^2\mathbf{I}\Big)^{-1}\mathbf{k}_{\mathbf{x},\hat{\mathbf{x}}}, \tag{5.13}$$

where $\sigma_n^2$ models the variability in the function value at an input location, allowing covariates with the same value $\mathbf{x}$ to produce different values $y$. The identity matrix $\mathbf{I}$ assigns this noise term to diagonal terms in the covariance matrix ($\mathbf{k}_{\mathbf{x},\mathbf{x}}$). Both components depends on partitioned elements of the full covariance matrix $\mathbf{k}$:

$$\mathbf{k} = \begin{bmatrix} \mathbf{k}_{\mathbf{x},\mathbf{x}} + \sigma_n^2 I & \mathbf{k}_{\mathbf{x},\hat{\mathbf{x}}} \\ \mathbf{k}_{\hat{\mathbf{x}},\mathbf{x}} & \mathbf{k}_{\hat{\mathbf{x}},\hat{\mathbf{x}}} \end{bmatrix}. \tag{5.14}$$

The value of each entry is defined by evaluating a kernel function at the corresponding training or test input vector. The form of the kernel function is variable and encodes assumptions about the spatial correlation between the response at different input locations. One common choice is the Squared-Exponential (kernel function) (SE) which depends on the magnitude of the distance between two vectors in input space $\Big|\mathbf{x}-\mathbf{x}'\Big|$ as:

$$k_{SE}(\mathbf{x},\mathbf{x}') = \sigma_f^2 \exp\left(-\frac{1}{2l^2}\Big(\mathbf{x}-\mathbf{x}'\Big)\Big(\mathbf{x}-\mathbf{x}'\Big)^T\right). \tag{5.15}$$

The parameters $\sigma_f$ and $l$ define the variance and length scale of the kernel function respectively. These parameters are referred to as hyper-parameters because they apply equally to all entries in the covariance matrix. They are unknown in advance and can be estimated from the training data using maximum likelihood estimation [176]. When applied to regression through Eq. (5.11), the SE kernel assumes that response estimates vary smoothly with changing input. However, other kernel functions can provide different forms of response, for example functions that aren't smooth, as discussed in Chapter 6.

The form of the conditional Gaussian distribution given in Eq. (5.11) assumes the unconditioned GP has a constant mean equal to zero. If prior information is known about the relationship being estimated, this assumption can be altered, for example, fitting the GP to an underlying linear function to capture general trends in the data [176]. This technique is also applied under the name kriging in the field of geostatistics [177]. Two types of GP model are relevant for this work: prediction using only the mean function (simple kriging) and using the full GP to model uncertainty in the predictions (standard or universal kriging). Indeed, the suitability of GP regression for application to OWTs has already been demonstrated by others [162, 163]. However, they have not yet been applied to the full range of random variables that drive fatigue loading nor to reliability assessment.

## 5.4 Fatigue loss calculation

The review of fatigue damage assessment in Section 5.2.1 highlighted that evaluating total fatigue damage requires predictions of damage for every environmental condition weighted by the probability of occurrence (i.e, the hazard). The disaggregation of risk into hazard and fragility used in a CAT modelling framework, described in Section 3.3 can be used for this calculation. However using this approach directly is computationally inefficient as calculating fragility requires the limit state function to be computed, by Monte Carlo sampling, for all environmental conditions. A more efficient procedure involves evaluating the lifetime fatigue damage first, then solving the limit state equation. Consequently, the fatigue limit state in Eq. (5.8) is solved directly in a single step, yielding the probability of fatigue failure. The structural failure rates from the FLS can be combined with those from the ULS and other non-structural components using the loss calculation procedure described in Section 3.3.5.

This calculation is split into three distinct elements, shown on Figure 5.1. It utilises the GP surrogate model described in Section 6.3 to enable high

fidelity assessment of fatigue damage. The individual steps are:

1. A GP surrogate model is fitted, this replaces the computationally expensive structural analysis package FAST with a statistical model that can be sampled rapidly. Fitting the model is achieved by sampling from the site environmental conditions and running a structural analysis for each sample. The samples are split into two sets, one for model fitting, and one to validate the quality of the model (cross validation).

2. The FLS reliability is evaluated by drawing fatigue damage predictions from the surrogate model, which are combined with probability distributions describing the site environmental conditions. The fatigue material properties are sampled separately and used to solve random variables in the to solve Eq. (5.8) using Monte Carlo simulation.

3. The probability of failure from fatigue is combined with the reliability of other components in an assessment of financial loss using cost data, similarly to the ULS case.

## 5.5 Conclusions

A method for evaluating FLS risk was proposed. This is particularly important as fatigue is often the limit state that drives structural design in European waters. A similar approach can also be used for the calibration of code-based partial safety factors to be used in the design of OWTs. The proposed model allows for the rapid evaluation of monopile fatigue failure based on time-domain structural analysis. This will allow an accurate analysis of the fatigue damage using the full site probability distribution of environmental conditions. Other techniques for reducing the computational burden of this same problem would not have yielded the same benefits. A simplified model would not include the accurate analysis and load-case lumping still requires the full FLS analysis to define the reduced set of load cases.

The same approach for combining losses from the structural and equipment components as used in the ULS, Chapter 3, was proposed. This will

allow combined ULS, FLS and equipment loss assessment, as is implemented in Chapter 6 for a case study OWF located in European waters. This assessment compares losses resulting from the FLS with those evaluated using the ULS in Section 4.

# Chapter 6

# Implementation of FLS loss framework

## 6.1 Introduction

In Chapter 5 a framework was developed for calculating FLS risk and then combining this with the loss calculation described in Chapter 3. The present chapter implements the FLS calculation for a series of case study locations. In Section 6.2 the case study sites and structural model are introduced, then the GP model developed is described in Section 6.3. The output from the model is discussed in Section 6.4, focusing on the accuracy of different GP modelling assumptions. The number of samples necessary to estimate OWT reliability and the applicability of a surrogate model trained at one site to others with different environmental conditions is also evaluated. The FLS reliability is combined with the electrical and mechanical components in Section 6.5 to estimate annualised losses. In Section 6.6, losses arising from the ULS, FLS and equipment are compared in order to assess which are relevant to the assessment of OWT.

## 6.2 Case study definition

### 6.2.1 Site and environmental conditions

This study uses environmental data measured by three met-masts which are part of the FINO project to record environmental conditions in the North and Baltic Seas [19]. They are located in the German North Sea (FINO1 and FINO3) and the Danish sector of the Baltic Sea (FINO2) as indicated in Figure 6.1. Each site has between 7 and 13 years worth of continuously recorded environmental data. The environmental data used for the ULS loss calculation, Section 4.2, is not used for this case study as Ijmmuiden K13 only provide scatter charts, and do not provide recorded site data, nor the full site probability distributions required for a FLS assessment. In contrast, all data recorded by the FINO met-masts has been published, making it more suitable for fatigue analysis.

The FINO3 met-mast is the main focus of this study. The variables used in this study (as discussed in Section 5.3) are summarised in Table 6.1 and are modelled as random variables with assigned probability distributions. The

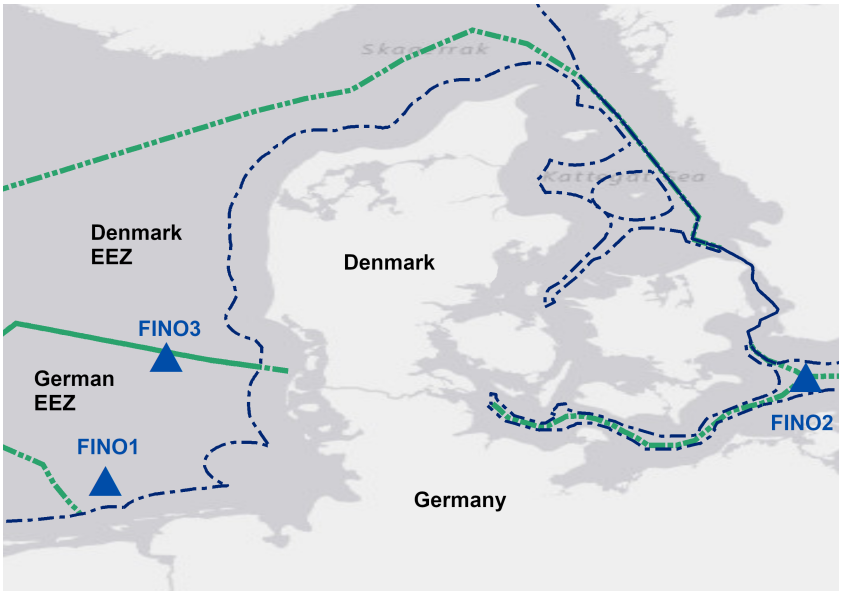


**Figure 6.1:** Location of the three FINO met-mast sites. Territorial waters are shown with a dashed line and exclusive economic zones using a double-dashed line.

only independent parameter is the mean wind speed; all other parameters are modelled by conditional distributions with dependencies indicated in Table 6.1. The wind and wave direction variables are modelled through non-parametric Kernel Density Estimator (KDE), because the measured site data was found to have multiple peaks caused by different prevailing directions. The dependencies are visible by plotting the conditional probability distributions for the FINO3 site, where the relationships become clear. Figure 6.2 and 6.3 show the discrete bins into which the continuous environmental variables were segmented. Full details of this calculation and details of the conditional probability distributions at the other FINO sites are provided by Hubler et al. [19]. Similar distributions were provided for the FINO1 and FINO2 sites [19], but are not shown here to save space. The distribution of wave angle is not plotted as it is dependent on three variables.

The water depth at the FINO3 met-mast is 22m (the site depth varies between 22m and 30m).

## 6.2.2 Fatigue damage calculation

### 6.2.2.1 Structural model

The 3-bladed NREL 5MW OWT on monopile sub-structure [42] is used as the reference structure in this study. The structural analysis is conducted in FAST, which is an aero-elastic simulation package. Both the structural model and the simulation package are described in detail in Section 4.2.2.2.

The below mudline foundation has been found to significantly influence

**Table 6.1:** Probability distributions used to model environmental conditions at the FINO3 site, showing the conditional dependencies defined by Hubler et al. [19].

| Parameter | Variable | Distribution | Dependencies |
|---|---|---|---|
| Mean wind speed | $V_w$ | Weibull | N/A |
| Turbulence intensity | $T_i$ | Weibull; Gamma | Mean wind speed |
| Significant wave height | $H_s$ | Gumbel; Weibull | Mean wind speed |
| Peak spectral period | $T_p$ | Bimodal Gumbel | Significant wave height |
| Wind direction | $\theta_{wind}$ | Non-parametric KDE | Mean wind speed |
| Wave direction | $\theta_{wave}$ | Non-parametric KDE | Significant wave height; Wind direction |

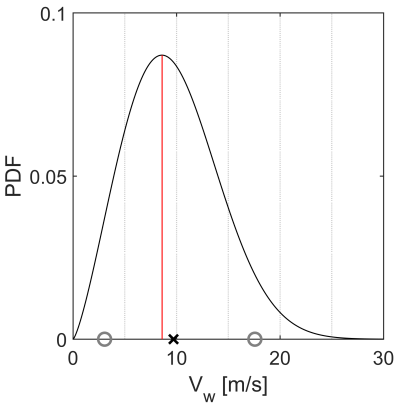


**(a)** Mean wind speed.

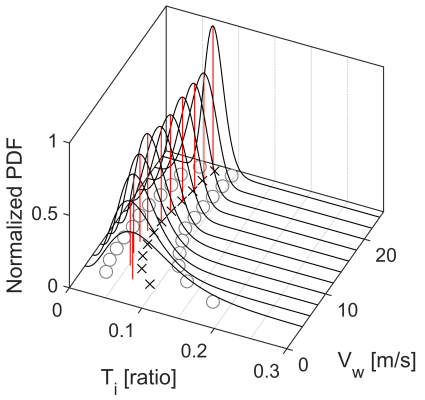


**(b)** Turbulence intensity dependent on mean wind speed.

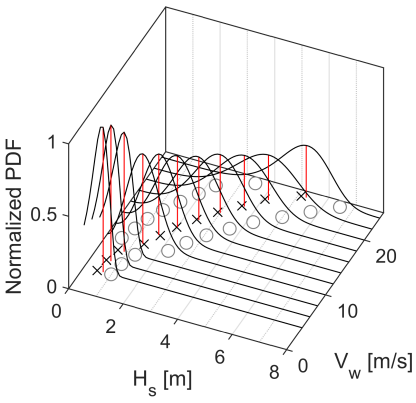


**(c)** Significant wave height dependent on mean wind speed.

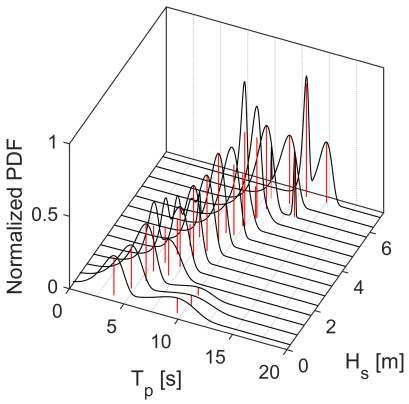


**(d)** Peak spectral period dependant on significant wave height

**Figure 6.2:** Probability distributions of environmental conditions at the FINO3 met-mast. The mean of each distribution is identified by an 'x', the 0.05 and 0.95 quantiles by a circle, and the mode by a red line. The normalised values are calculated such that the highest mode occurs at a PDF value of 1.

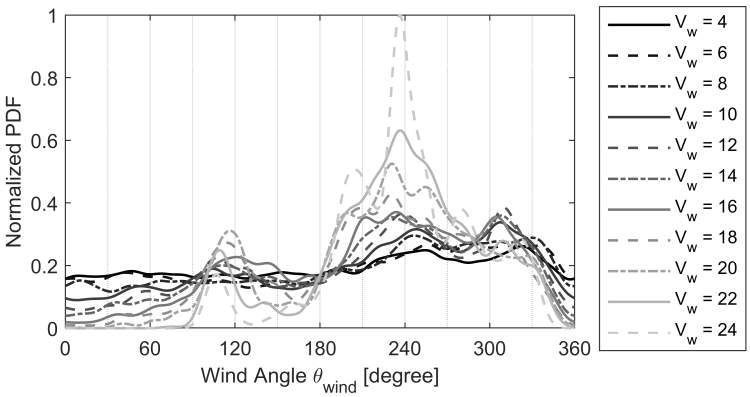


**Figure 6.3:** PDFs of wind angle dependent on the mean wind speed, increasing wind speed is indicated by lighter coloured line.

the structural response in dynamic analysis of OWTs [178]. In this study the foundation is modelled using the AF method [179], with the fixity length selected to match the first natural frequency between the AF supported OWT and an OWT with a linear-elastic foundation model, described in Appendix A. The soil properties were taken from Damgaard et al. [85]. Individual analyses of 11-minute length were conducted and the first minute was deleted to remove transient effects [120]. The IEC 61400-3 load case DLC 1.2 [6] was used to represent general analysis conditions. However, instead of simplifying the environmental variables the full joint-probability distributions described in Section 6.2.1 are used to calculate loads on the OWT.

In a post-processing step, the mudline bending moment time-series is extracted and converted into stresses. Assuming that the stresses in the wall of the monopile behave in-plane (with no bending moments) a membrane stress calculation can be used. This negates the need for complex finite-element analysis and can be implemented using a simple set of membrane stress equations.

#### 6.2.2.2 Fatigue damage

Fatigue damage is calculated for a single weld located at the mudline. The weld is a transverse butt weld with no weld toe grinding (DNVGL class D [100]) and is assumed to be protected from corrosion by cathodic protection. The DNVGL SN curves [100] are bi-linear in the log scale; to simplify the limit state calculation, only the initial part of the SN curve is used. Fatigue damage is estimated using this method at 12 locations equally distributed around the mudline cross-section, with the largest value extracted for use in the fatigue life calculation.

Hubler et al. [19] observed that fatigue damage increased with the simulated duration of a time-series analysis. This was due to the effect of un-closed cycles in the rainflow counting algorithm, the proportion of which reduce with an increased time-series length. One solution is to append copies of the time-series, producing a long composite time-series. Following the recommendations of Hubler et al. [19] the stress time-series is duplicated 35 times, generating a

six-hour long time-series. The rainflow counting algorithm [165] is then used to extract the magnitude and number of different stress ranges occurring within the six-hour stress time-series allowing fatigue damage to be estimated using the equations in Section 5.2.1.

## 6.3 Development of the surrogate model

### 6.3.1 Training and validation data sets

As discussed above, GP regression is used here to approximate the OWT response in terms of 20-year fatigue damage. This is done by fitting the proposed surrogate models to the results obtained from the structural analysis. Training sets are used to fit the surrogate model and a validation set is used to assess the goodness of fit. The number of dimensions in the input vector matches the number of parameters in the environmental model, with the only difference being that the wind and wave angle are combined into a single variable, $\theta_{mis}$.

The first training set is generated using a sample of 1000 analyses, selected as a representative large number, the accuracy of which will be tested in the results section. For each sample 6 stochastic seeds are used, following the recommendations in IEC 61400-3 [6]. The sample is drawn randomly from the input environmental parameters at the FINO3 site, resulting in a total 6000 structural simulations. The sample is constructed sequentially by taking 1000 uniformly distributed random numbers from the Inverse Cumulative Distribution Function (iCDF) of each environmental variable at the site. The sequence of the sampling is defined by the dependency structure from Table 6.1: $V_w$ is sampled first followed by conditional $T_i$, $\theta_{wind}$ and $H_s$, then finally the $T_p$ and $\theta_{wave}$ distributions.

Site-specific conditional distributions are truncated to prevent unrealistic environmental conditions. This is achieved by scaling the uniformly distributed random numbers to produce acceptable range of environmental conditions values after being converted using the iCDF. The mean wind speed is truncated to values occurring between 3m/s and 25m/s, conditions in which the turbine

is operational [42]. Additionally, the significant wave height (at low mean wind speeds) and peak spectral period are both represented by extreme value distributions which support negative values. However, numbers less than zero are not permissible as inputs into the spectral equations which are used to generate environmental conditions, described in Section 6.2.2.1, and therefore the distributions were truncated to avoid negative numbers.

A second training set is generated using a common Design of Experiment (DOE) approach by defining an upper and lower bound for each input parameter then by splitting this range into evenly spaced intervals for the FINO3 site. The bounds and the criteria for selecting them for each variable are summarised in Table 6.2. A grid is generated from these sets of points, leading to $6 \times 5 \times 5 \times 6 \times 7 = 6300$ sample points (only three seeds are run at each to save computational effort).

The same approach used to generate the first (random) training set is also used to generate a separate random validation set for each FINO site. The site-specific probability distributions of the environmental variables are sampled with 1000 new points and a new set of 6 random seeds were used as input to the structural model. This set of data is used to compare the goodness of fit between different models which are trained on the random and DOE training data sets.

**Table 6.2:** Input range of each environmental variable in the GP model. The upper and lower bounds were used to generate the DOE sample.

| Variable | Lower bound | Upper bound | Number of DoE samples | Criteria |
|---|---|---|---|---|
| $V_w$ | 4 | 24 | 6 | Range of $V_w$ where the OWT is operational |
| $T_i$ | 0.01 | 0.18 | 5 | The upper limit is two standard deviations above the mean $T_i$ of the lower $V_w$ bin; the lower limit is selected above 0 (for turbulence spectrum equation). |
| $H_s$ | 0.01 | 7 | 5 | The upper limit is two standard deviations above the mean $H_s$ of the largest $V_w$ bin; the lower limit is above 0 (for wave spectrum equation). |
| $T_p$ | 1 | 15 | 6 | The upper limit is the mode of 2nd peak in the largest $H_s$ bin. |
| $\theta_{mis}$ | 0 | 180 | 7 | Full range of misalignments, given the symmetry of the OWT. |

### 6.3.2 Statistical models

GP models are fitted to the training set observations by selecting values of noise ($\sigma_n$) and kernel hyper-parameters minimising the log marginal likelihood. This is achieved using a gradient descent algorithm, which iterates from a set of assumed, initial conditions to the optimal combination of parameter values. Different assumptions concerning the form of the GP were tested, as described by Rasmussen and Williams [176], including:

- Kernel function: SE, Matern 3/2, Matern 5/2 and rational quadratic.
- Underlying function on which the GP is fit: none and linear function.
- Inputs: not standardized and standardized (i.e. the inputs are transformed from their natural distribution to a standard normal distribution).

The squared exponential kernel has been introduced in Eq. (5.15), and results in a GP that is smooth (infinitely mean square differentiable). The Matern kernel has more parameters and can model functions that are not infinitely smooth. The kernel has two commonly used variants of parameter, the 3/2 ($k_{MT,3/2}$) and 5/2 ($k_{MT,5/2}$), which simplify the kernel functions to:

$$k_{MT,3/2}(\mathbf{x},\mathbf{x}') = \left(1+\frac{\sqrt{3\Big(\mathbf{x}-\mathbf{x}'\Big)\Big(\mathbf{x}-\mathbf{x}'\Big)^T}}{l}\right)exp\left(-\frac{\sqrt{3\Big(\mathbf{x}-\mathbf{x}'\Big)\Big(\mathbf{x}-\mathbf{x}'\Big)^T}}{l}\right), \tag{6.1}$$

$$k_{MT,5/2}(\mathbf{x},\mathbf{x}') = \left(1+\frac{\sqrt{5\Big(\mathbf{x}-\mathbf{x}'\Big)\Big(\mathbf{x}-\mathbf{x}'\Big)^T}}{l}+\frac{5\Big(\mathbf{x}-\mathbf{x}'\Big)\Big(\mathbf{x}-\mathbf{x}'\Big)^T}{3l^2}\right) exp\left(-\frac{\sqrt{5\Big(\mathbf{x}-\mathbf{x}'\Big)\Big(\mathbf{x}-\mathbf{x}'\Big)^T}}{l}\right), \tag{6.2}$$

where $l$ is the length scale.

The rational quadratic covariance function decays less quickly with distance than the squared-exponential:

$$k_{RQ}(\mathbf{x},\mathbf{x}') = \left(1 + \frac{\left(\mathbf{x}-\mathbf{x}'\right)\left(\mathbf{x}-\mathbf{x}'\right)^T}{2\alpha l^2}\right)^{-\alpha} \tag{6.3}$$

where $\alpha$ is a positive-valued scale-mixture parameter, and the rational quadratic converges to the squared-exponential when $\alpha \to \text{inf}$.

All kernel functions are of the automatic relevance detection type [176], meaning that they allow different length scales for each input dimension. The parameter values are calibrated to the training data using the maximum likelihood method.

### 6.3.3 Fitting Gaussian process

The Gaussian process can be fitted computationally using the algorithm presented by Rasmussen and Williams [176]. This has been encoded into packages for both Matlab (through the Statistics and Machine Learing Toolbox) and Python (through the scikit-learn package). These make it simple to fit a GP model, as indicated on Figure 6.4 which shows the code required to fit a model to a series of $X$ input variables and damage predictions $y$. The "fitgp" function calculates the MLE prediction of the kernel parameters for the kernel function selected. It should be noted that to keep the figure simple the full text input options for the "fitgp" function have not been quoted.

### 6.3.4 Metrics for goodness of fit

The accuracy of different meta-models is compared using three metrics:

- Bias, $Bias = E\left[\hat{y}_i - y_i\right]$
- Mean squared error ($MSE$), which is the a combination of the bias and sum of squared error ($SSE$), $MSE = Bias^2 + SSE = \frac{1}{n-p}\sum_{i=1}^{n}\left(\hat{y}_i - y_i\right)^2$
- Coverage of the 50%, 90% and 95% confidence intervals

These metrics all rely on: the meta-model prediction at the $i$th $\in [1,n]$ test point ($\hat{y}_i$), predicted by the GP, and the observed value at same location

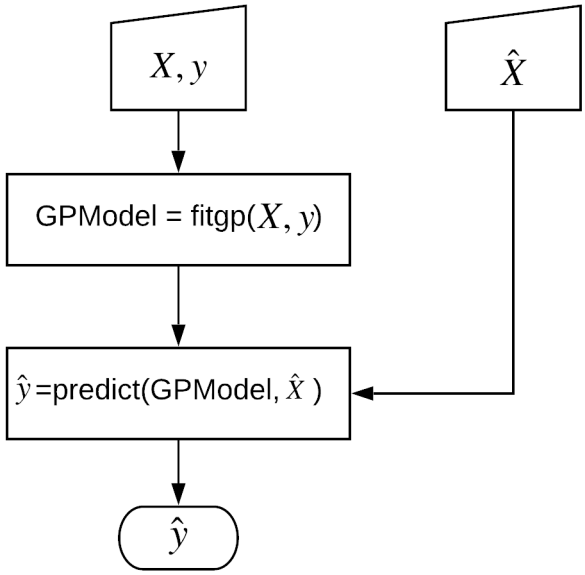


**Figure 6.4:** Flowchart showing code used to fit the GP.

($y_i$), computed using structural analysis. The number of dimensions of the predictor is denoted $p$, which is 5 per Section 6.2.1.

The bias is the expected value of the difference between GP predictions and the structural analysis outputs, indicating whether the predictor consistently under or over-estimates the training values. $MSE$ gives the expected error, by combining bias and sum of square error (the expected deviation of the predictor about its mean value), therefore estimating the goodness of fit [180]. The coverage measures the proportion of test samples falling within a set of confidence intervals: if the 95% confidence intervals are well estimated, then approximately 95% of the data should fall within these bounds. It therefore measures how well the model estimates scatter in the underlying data. It also identifies whether the statistical model introduces a large magnitude of model uncertainty, as the confidence bounds in the GP prediction would become much larger than the validation data.

## 6.4 Fatigue reliability analysis results

### 6.4.1 Comparison of surrogate models

#### 6.4.1.1 Random and DoE training data sets

Various GP models (as detailed above) are fitted to the DOE and the random training set analysis results. In advance the DOE model is expected to perform worse than the random sample as these models are unable to capture high frequency variation the behaviour of a function due to the uniform placement of sample points [66]. In this section, the GP models fitted to the full DOE and random sample sets are compared, these comprised 18900 and 6000 analyses respectively. The GPs fitted using the DOE training data is found to estimate the FINO3 validation set poorly in comparison to those fitted using the random sample training data. The best fitting GP model in the case of the DOE training set is shown against the best fitting GP model in the case of the random training set using the same kernel function (i.e., squared exponential) in Figure 6.5 (in terms of DEL). The DOE-based GP model results in greater scatter and tends to underestimate test values as indicated by the mean trend-line. The quality of the DOE-based surrogate model is worse, even if a larger number of samples has been used to fit the GP, because the samples are sparsely distributed. In the case of the DOE-based training set, the selected training points are evenly distributed over the input space - as opposed to being clustered around the mean values of the site-specific (conditional) probability distributions of environmental conditions as in the random sample. Observation around the mean values of each environmental variable have a much larger contribution in estimating fatigue damage. These findings are confirmed using the goodness of fit metrics reported in the first three columns of Table 6.3, where the DOE training data produces a model that has much higher uncertainty than the underlying data, with 100% coverage observed at all confidence levels. In contrast, the GP fitted to the random training set has much better coverage, although it tends to underestimate scatter at all cover-

age quantiles. Therefore, in the remainder of this chapter, only the random sample training set will be used.

The GP fit using the FINO3 random training is compared with the validation sets from the FINO1 and FINO2 site data in Table 6.3. This indicates that, while the bias and $MSE$ increase when the GP model trained at FINO3 is validated against fatigue damage predicted at other sites, the errors are not large. As the environmental probability distributions change between the sites, the observed differences are not large, especially as the FINO1 and FINO3 met-masts are close (both in the North Sea) whereas the FINO2 met-mast is in the Baltic sea. This explains the reduced accuracy of the GP when validated against the FINO2 data. This is visible by comparing the $T_p$ parameter from all sites; the FINO1 and FINO3 distributions are broadly similar while the FINO2 distribution is more peaked.

The relatively high accuracy of the GP surrogate model suggests that a single GP model could be developed across multiple sites experiencing similar environmental conditions, even if the model is trained against data sampled using single-site joint-probability distributions.

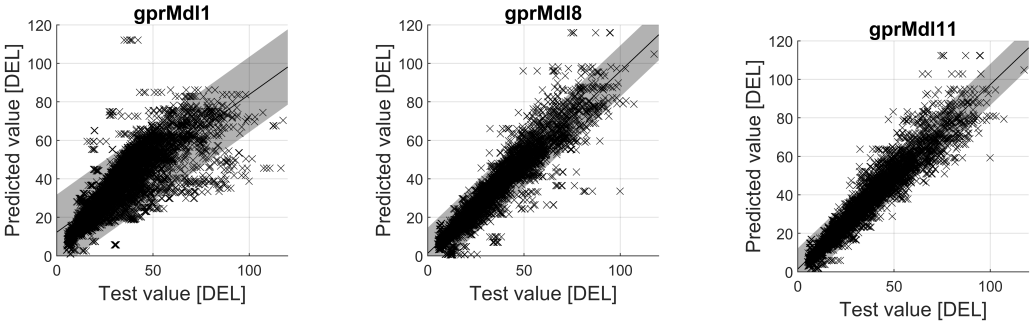


**(a)** Validation plot for DOE sample with squared-exponential kernel.

**(b)** Validation plot for random sample with squared-exponential kernel.

**(c)** Validation plot for random sample with Matern 5/2.

**Figure 6.5:** Validation plots for two representative GP models. The line shows the result of a simple linear regression fitted to the data and the shaded areas show the 95% confidence intervals.

**Table 6.3:** Kernel parameters and goodness of fit metrics for kernel functions fitted to different training sets across the FINO sites. Sigma refers to noise (prior covariance) in the GP regression and SigmaF is the factor applied to the kernel function (see Eq. (5.13)).

| **No Samples** | $6300 \times 3$ | | | $1000 \times 6$ | | | |
|---|---|---|---|---|---|---|---|
| **Site** | **FINO3** | | | **FINO1** | | **FINO2** | |
| Gaussian Proccess type | std input; SE kernel [gprMdl1] | std input; SE kernel [gprMdl8] | std inputs; matern 5/2 kernel [gprMdl11] | std input; SE kernel [gprMdl8] | std inputs; matern 5/2 kernel [gprMdl11] | std input; SE kernel [gprMdl8] | std inputs; matern 5/2 kernel [gprMdl11] |
| Sigma | 59.366 | 4.128 | 3.412 | | | | |
| LengthScale1 ($V_w$) | 48.367 | 2.428 | 4.745 | | | | |
| LengthScale2 ($T_i$) | 2.797 | 0.513 | 0.848 | | | | |
| LengthScale3 ($H_s$) | 1.945 | 1.823 | 2.930 | | | | |
| LengthScale4 ($T_p$) | 2.189 | 0.946 | 1.705 | | | | |
| LengthScale5 ($\theta_{mis}$) | 134.653 | 55.194 | 75.197 | | | | |
| SigmaF | 239.940 | 32.382 | 35.309 | | | | |
| LogLikelihood | -11224 | -6312 | -6036 | | | | |
| Bias | 2.157 | -0.455 | 0.059 | -0.6429 | -0.0592 | -1.1305 | -0.139 |
| $MSE$ | 127.598 | 45.322 | 29.513 | 65.6129 | 46.3912 | 131.4006 | 76.6152 |
| Coverage: | | | | | | | |
| 95% | 1.000 | 0.935 | 0.931 | 0.9102 | 0.9057 | 0.8415 | 0.8775 |
| 90% | 1.000 | 0.909 | 0.907 | 0.8706 | 0.8715 | 0.7868 | 0.8335 |
| 50% | 0.991 | 0.669 | 0.682 | 0.5787 | 0.593 | 0.4904 | 0.5214 |

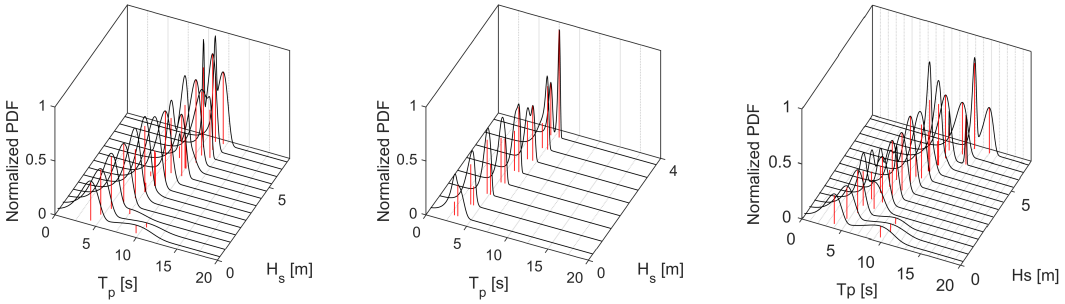


**Figure 6.6:** Probability distribution of $T_p$ parameter across the FINO1 (left), FINO2 (middle) and FINO3 (right) sites.

#### 6.4.1.2 Optimal gaussian proccess kernel

All combinations of kernel function, basis function, and standardization listed in Section 6.3.2 are tested, with a summary of the key results listed in Table 6.4. Validation predictions from the SE and Matern 5/2 kernels, are shown in Figure 6.5b and 6.5c, confirming the slightly reduced bias and scatter observed with the Matern kernel; however, the coverage metrics are slightly worse. The Matern 3/2 has slightly lower $MSE$, but higher bias. Including standardised variables and/or a linear basis function make the fit worse but slightly improved the bias. The same results are found when different kernels were tested against the FINO1 and FINO2 validation sets, as shown in Table 6.4 where the SE and Matern 5/2 kernels are compared.

Based these findings, the random sample data sets with a Matern 5/2 kernel and zero basis function will be used in the remainder of this work; as it provides a good trade off between bias, $MSE$ and coverage. These findings agree with Hafele et al. [160] who found a Matern 5/2 kernel to be best for representing joint fatigue loads for a OWT on jacket substructure.

**Table 6.4:** Kernel parameters and goodness of fit metrics for different kernel functions at the FINO3 site using 300 samples and two seeds. Sigma refers to noise (prior covariance) in the GP regression and SigmaF is the factor applied to the kernel function (see Eq. (5.13)). The rational quadratic kernel has an additional parameter $\alpha$ following Eq. (6.3), so the length scales are not reported.

| **No Samples** | **300*2** | | | | | | |
|---|---|---|---|---|---|---|---|
| Gaussian Proccess type | std input; SE kernel [gprMdl8] | std inputs; matern 3/2 kernel [gprMdl10] | std inputs; matern 5/2 kernel [gprMdl11] | std inputs; rational quad kernel [gprMdl12] | std input; standardised; matern 5/2 kernel [gprMdl14] | std input; basis function; matern 5/2 kernel [gprMdl15] | std input; standardised; basis function; matern 5/2 kernel [gprMdl16] |
| Sigma: | 4.297 | 3.429 | 3.830 | 3.290 | 3.830 | 3.439 | 3.191 |
| LengthScale1 ($V_w$) | 29.949 | 66.325 | 39.538 | | 9.659 | 30.533 | 0.760 |
| LengthScale2 ($T_i$) | 0.704 | 1.095 | 0.809 | | 30.391 | 0.490 | 0.002 |
| LengthScale3 ($H_s$) | 2.115 | 2.321 | 1.963 | [ N/A ] | 1.928 | 0.933 | 0.542 |
| LengthScale4 ($T_p$) | 1.291 | 2.596 | 1.849 | | 1.202 | 1.118 | 0.276 |
| LengthScale5 ($\theta_{mis}$) | 52.879 | 98.203 | 78.049 | | 1.740 | 44.711 | 117.778 |
| SigmaF | 34.303 | 31.323 | 29.726 | 58.929 | 29.726 | 15.562 | 14.693 |
| LogLikelihood | -1891 | -1855 | -1871 | -1857 | -1871 | -1853 | -2113 |
| Bias | -0.354 | -0.246 | -0.246 | -0.192 | -0.246 | -0.153 | 0.644 |
| $MSE$ | 41.270 | 37.012 | 36.515 | 40.064 | 36.515 | 39.471 | 204.410 |
| Coverage: | | | | | | | |
| 95% | 0.925 | 0.927 | 0.927 | 0.930 | 0.927 | 0.925 | 0.949 |
| 90% | 0.892 | 0.897 | 0.898 | 0.901 | 0.898 | 0.896 | 0.917 |
| 50% | 0.627 | 0.642 | 0.639 | 0.649 | 0.639 | 0.639 | 0.643 |

#### 6.4.1.3 Number of training samples

The computational burden required to run 6000 time-domain structural simulations is large. The random sample-based GP models derived in the previous sections are relatively accurate, partly as a result of the high sample density. In practice, this computational burden may be infeasible on a standard workstation. Any reduction in the required number of samples has a benefit on computational efficiency. Moreover, GPs need to take into account the whole training data each time they make a prediction. This means not only that the training data has to be kept at inference time but also means that the computational cost of predictions scales with the number of training samples. Hence, the impact of reducing the number of analyses on the model goodness of fit is investigated in this section.

Generally, it is not clear in advance whether reducing the number of samples or seeds will have a greater impact on the accuracy of the surrogate model. The number of seeds will affect the number of analyses at a specific set of input conditions and may affect the coverage metrics (as the scatter at each input point will be defined better). Reducing the number of samples will affect the sampling quality over the input conditions, which should, in turn, effect the mean square error.

Different numbers of random samples and seeds are tested by drawing sets of 1000 bootstrapped samples from the full set of analysis results ($1000 * 6$); the consequent scatter in the goodness of fit metrics are assessed for these reduced analysis sets. The results, presented in Figure 6.7, suggest that both the number of samples and seeds can be reduced without a large impact on the mean squared error and the coverage. It is noted the MSE reported on Table 6.4 are relatively large, even for the Matern 5/2 kernel, which was found to be the best fitting. The lifetime fatigue damage was calculated using the sample of environmental conditions used in the validation set, allowing direct comparison between the GP prediction and structural analysis output. The results are presented on Table 6.5, and demonstrate that the surrogate model

results in predictions of fatigue life damage similar to that predicted using a structural simulation. The relative error is comparable to those reported by Huchet et al. [181] who found a 4.43% error between an adaptive Kriging algorithm (requiring only 174 simulator calls) and aero-elastic analysis.

The apparent improvement over the MSE error results is because the fatigue lifetime damage is weighted by the probability of occurrence of the environmental conditions, meaning that the rare but high damage events that skew the MSE are averaged out using this metric.

The absolute value of damage predicted on Table 6.5 should be interpreted with caution as it is predicted using only 1000 samples. Whereas the values used in the reliability analysis use a much larger sample.

In the remainder of this study 300 samples and 2 seeds $(300 * 2)$, will be used because this provides the best trade off in terms of $MSE$. For this analysis set the standard deviation in coverage is under 5%. This reduces the computational difficulty of fitting the GP by a factor of 10, from 6000 to 600 analyses. It also improves the speed at which the FLS meta-model can be sampled, as the conditional GP is computed using a reduced training set.

### 6.4.2 Fatigue reliability analysis

FLS reliability assessment is finally implemented using a plain Monte Carlo approach, Eq. (5.9), in combination with the limit state equation defined in Eq. (5.8). The Matern 5/2 kernel trained using $300 \times 2$ samples is used to evaluate damage - as it combined the most accurate kernel function with an appropriate number of samples, as discussed above. In Eq. (5.8), the 20-year damage predictions are weighted by the site environmental joint probability distribution.

**Table 6.5**

| | Validation | GP 1000x6 | GP 300x2 |
|---|---|---|---|
| DEL $(N/m^2)$ | 36.380 | 36.731 | 36.555 |
| Damage | 0.829 | 0.853 | 0.841 |
| Difference Damage (%) | | 2.90 | 1.45 |

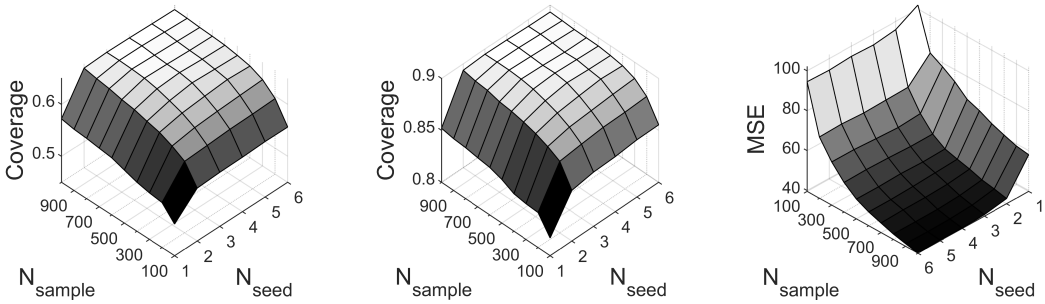


**(a)** 50% coverage. **(b)** 90% coverage. **(c)** Mean squared error.

**Figure 6.7:** Impact of different combinations of samples and seed on the GP accuracy metrics, these estimates were generated by taking the mean of 1000 bootstrap samples drawn from the full set ($1000 \times 6$) of random samples.

The fatigue damage is calculated numerically using a Monte Carlo integration with $1 \times 10^6$ samples from the joint PDF of environmental conditions (with the upper and lower boundaries in Table 6.2). The finite sample of the GP is associated with some error and the accuracy of the prediction is assessed by rerunning the integration 1000 times for each site using the mean GP. The resulting histograms of fatigue damage are shown in Figure 6.8. A normal probability distribution is fit to the histograms and this distribution assumption was confirmed using the Anderson-Darling normality test at a 5% significance level. The low CoV of 6.3% indicates that the $1 \times 10^6$ Monte Carlo samples are sufficient to provide a consistent estimate of fatigue damage.

The fully probabilistic GP was also sampled at the FINO3 site. The resulting histograms of fatigue damage are shown in Figure 6.8. The resulting distribution of the lifetime fatigue damage is the same as that generated when using the GP mean function, as shown in Figure 6.8. Therefore, when evaluating the fatigue limit state in the reliability assessment, damage can be modelled using the mean function value from Figure 6.8. In the subsequent analysis fatigue damage is predicted using the GP mean estimates for each of the FINO sites.

The mean values of lifetime damage calculated for the respective sites are 0.366 (FINO1), 0.175 (FINO2) and 0.427 (FINO3). The similarity between

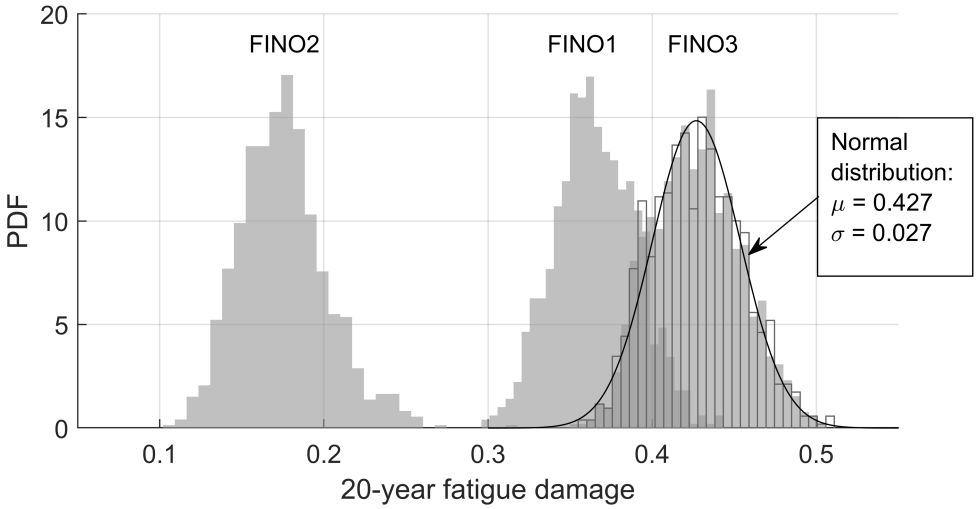


**Figure 6.8:** Histograms of fatigue damage samples calculated for the three FINO sites (in block gray). The FINO3 site calculation was also run using the fully probabilistic GP with results shown in gray lines and the best-fit normal distribution in black.

fatigue damage using the FINO1 and FINO3 met-masts is consistent with the findings in Section 6.4.1 due to similar environmental conditions between the two sites. However, the damage predicted at the FINO2 site is much lower than the others primarily as a result of lower significant wave heights [19].

The probability of failure is finally evaluated by drawing a Monte Carlo sample from the limit state equation and solving Eq. (5.9). A sample size of $2 \times 10^6$ was because it was larger than the sample size of $3.996 \times 10^5$ necessary to achieve a CoV of 5% for a probability of failure of 0.001 calculated using the theoretical equation for error in the Monte Carlo estimator [171]. Limit state samples are plotted in the histogram on Figure 6.9, which also shows the best fit GEV distribution. The resulting probability of failure over a 20-year design life is $1.03 \cdot 10^{-3}$. Comparing this value to code target reliability levels seem to suggest that the NREL 5MW located at the FINO3 site has a non conservative level of safety. DNVGL Classification Note 30.6 [182] recommends a probability of failure of $10^{-4}$ if significant warning is visible before failure and $10^{-5}$ if there is no warning of failure for non-redundant structures with a low consequence. However, the NREL 5MW has not been specifically designed for

the FINO site-conditions and therefore a direct comparison between calculated and code-based failure rates is only illustrative.

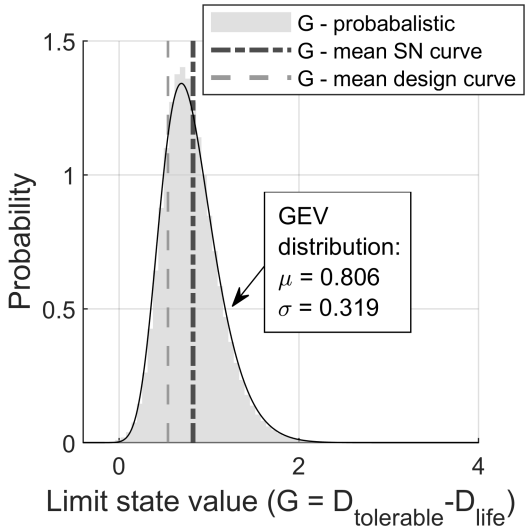


**Figure 6.9:** Histogram of the Monte Carlo limit state evaluations with a GEV distribution fit using MLE. The limit state evaluated using the mean SN curve and design SN curve with a damage threshold of 1 are also shown.

Scatter in the limit state is caused by uncertainty in the SN curve and tolerable damage variables. The GEV distribution has a CoV of 0.394, indicating the high uncertainty introduced by modelling the tolerable damage as a random variable. Within the limit state equation, the two random variables act against each other. Modelling the SN curve as random increases capacity (as the design curve is conservative), whereas modelling tolerable damage as random reduces capacity (because the median of random variable is below one). When the limit state equation is evaluated using the design SN curve and a fixed tolerable damage the limit state is 0.557 and when the mean SN curve is used 0.8236. When both random variables are modelled 22% of the limit state samples fall below the value predicted using the design SN curve and damage tolerance of one.

## 6.5 Fatigue loss

A comparison between the losses caused by different modelling assumptions for the structures FLS is presented in Figure 6.10. In Section 4.6.3 the monopile cost was not modelled, as the probability of failure of this component was found to be low. However, failure of the monopile is observed as a consequence of fatigue. The cost of the monopile is estimated using the equation proposed by Dicorato et al. [152]:

$$c_{mon} = 320 \cdot P_{WT} \cdot (1 + 0.02(h_{water} - 8))(1 + 8 \times 10^{-7}(h_{hub}(0.5\phi_R)^2 - 10^5)), \tag{6.4}$$

where the cost estimate depends on: $P_{WT}$ the rated capacity (MW), $h_{water}$ the water depth (m), $h_{hub}$ the hub height above mean sea level (m) and $\phi_R$ the rotor diameter (m). The equation originated from a 2003 feasibility study into OWT, and was validated against actual foundation costs from five real OWF. The average error was large, at 8.7%, but Eq. (6.4) was found to predict foundation cost better than two other cost models. Monopile cost was calculated using parameters for the NREL 5MW OWT, with: $P_{WT} = 5MW$, $D = 20m$, $h = 87.6m$, $D = 20m$; the resulting cost was €$2.38 \cdot 10^6$.

The analysis cases are the same as in Section 4.6.3, where, in Case 1 tower failure causes failure of other components, in Case 2 blade failure prevents that of the tower, in Case 3 the components are modelled independently and Case 4 structural failure is not modelled (and includes only equipment).

The bar chart Figure 6.10 (right) indicates that when structural failures are included (as in Case 1) there is a marginal increase in the loss over just modelling the equipment (Case 4) of around 10%. Modelling the components as independent caused small, 2%, reduction in loss.

The equipment only assessment (Case 4) resulted in a relatively large loss €$3.86 \cdot 10^4$, this is a consequence of the high failure rate of some expensive pieces of equipment, particularly the gearbox. However, it should be noted

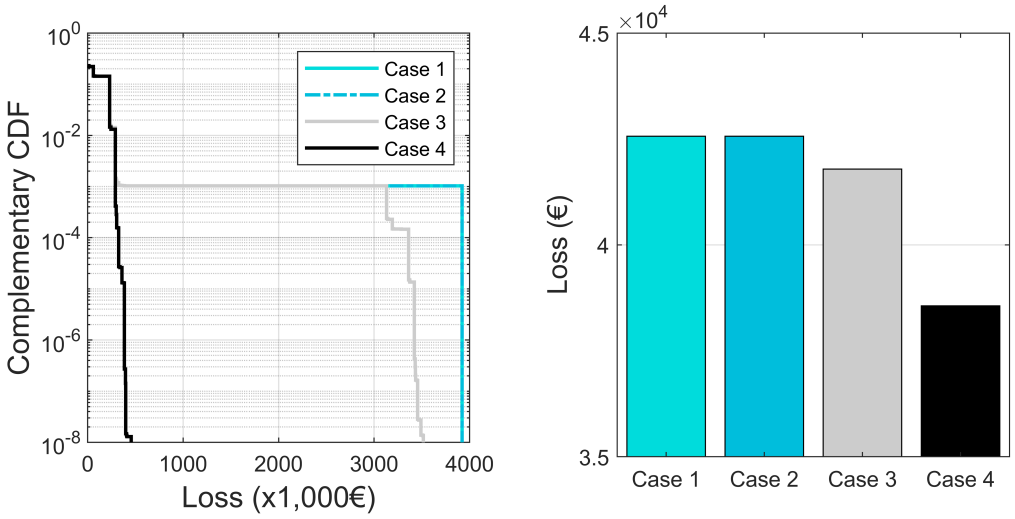


**Figure 6.10:** Loss CCDF comparing the OWT loss evaluated using the FLS and the equipment components (left). Bar chart comparing annual loss (right).

that the fatigue failure rate is equivalent to some of the equipment commonly included in empirical databases such as: controller, yaw system, transformer in Table 4.5 but causes much larger losses. The difference is that fatigue damage is cumulative over the life of the structure.

Preventative blade failure was not found to change the loss, as show by the minimal difference the loss bars for Case 1 and 2. This is due to low failure rate of the blade ($8.36 \cdot 10^{-5}$) in comparison to that of the structure ($1.00 \cdot 10^{-3}$).

## 6.6 Ultimate and fatigue loss comparison

The combined loss expected from an OWT can be predicted by merging the ULS and FLS structural limit states with failure of the equipment. Using the same procedure as described previously for evaluating the annual financial losses. The ULS losses are included using the results derived for the Ijmuiden K13 site in Section 4.6. The FLS losses are evaluated at the FINO3 site, as described in the previous sections. The loss data comes from different locations, however both are in the Dutch and German sectors of the North Sea, so the environmental conditions are expected to be broadly similar.

The results are presented as a CCDF in Figure 6.11 (left) and as loss in Figure 6.11 (right). The CCDF indicates that there is little change is observed when the ULS is modelled in addition to the FLS structural failure. This is confirmed by the aggregated loss in the bar chart, where modelling ULS in addition to the equipment results in a less than %1 increase over the case where only equipment is modelled. However, assessing the combined structural and equipment failures increases the annual loss by 11.2% over the equipment only case. The reason for this large difference is the larger failure rate and much higher cost of failure in the FLS, as the monopile is more expensive than the sum of all other equipment (including the tower).

In the design stage loss analysis applied in this thesis, only material costs are modelled, and the difference may be expected to be substantially larger if costs associated with vessel hire, required to implement repairs, had been included. Additionally, the failure of the structure would have a substantial additional impact on power production (i.e., through business interruption) which as not been modelled. The low impact of the ULS suggests that it might be able to be neglected in assessment of OWT structures.

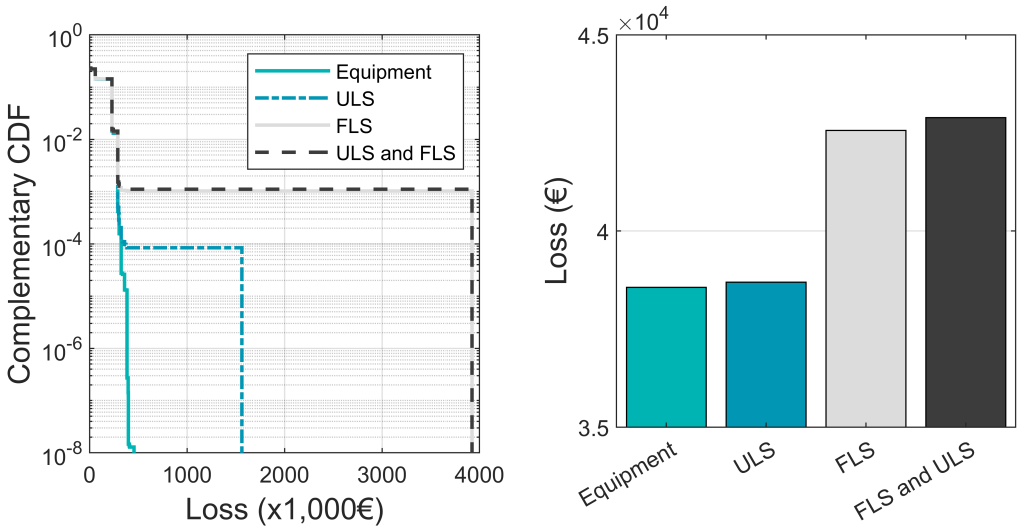


**Figure 6.11:** Loss CCDF comparing the OWT loss evaluated using the FLS and ULS (left). Boxplot comparing financial losses when ULS and FLS structural failure is included in the damage calculation (right).

## 6.7 Conclusions

The study presented in this chapter demonstrated that a surrogate model based on GP regression can enable calculation of fatigue reliability using detailed environmental conditions. The number of structural analysis samples required for a given level of error in the damage calculation was evaluated by statistical resampling. The sample could be reduced to 600 structural analyses, resulting in an acceptable scatter in fatigue damage, with a CoV of 6.3%. The use of GPs allowed a comprehensive assessment of the FLS, above what is achievable through standard analysis because it utilised a full joint-PDF of environmental conditions. The SN uncertainty and tolerable fatigue damage were modelled as random variables, and were shown to cause large scatter in the fatigue limit state, introducing a CoV around 40%.

The probability of failure for the case study NREL 5MW OWT was found to be $1 \cdot 10^{-3}$. This is a relatively large probability of failure compared to values recommended by design codes. However the dimensions of the NREL 5MW OWT had not been optimised for the site environmental conditions, and therefore the calculated probability of failure cannot be taken as representative of a real OWT at the site. Other OWT with different properties could be assessed as the approach taken in this chapter is flexible. Situations where the turbine is not operational, such as wind speeds above and below the operating range, can be assessed by fitting another GP to models representing those conditions.

Extending the fatigue calculation to other sites in European waters demonstrated that a surrogate model developed for a single site may be usable at other locations. This suggests that further computational savings would be possible if a representative GP was generated for a OWT model which is used across multiple locations.

The loss framework, developed in Section 3.3.5, was combined with FLS reliability to predict financial losses arising from failure of the OWT. This analysis indicated that the FLS is important to the reliability of the OWT. When

combined with the ULS loss from Section 4.6, the FLS was found to cause substantially larger financial losses. However, this analysis was conducted for an OWT located at a European site with relatively mild extreme environmental conditions.

# Chapter 7

# Conclusions

## 7.1 Summary

This thesis presented a novel decision-support framework to quantify risk for OWTs in a probabilistic manner. The framework enables an OWT to be treated as a system comprised of integrated structural and mechanical components, for which financial losses can be estimated. This allows identification of the components that contribute most to the total system loss. For example, based on a case study, the high failure rates of the equipment meant that these components dominated financial losses. However, the structural FLS was found to provide an important contribution due to its large financial consequence coupled with relatively high failure rates. The loss calculation provided in this thesis is an advancement towards enabling full resilience analysis for OWTs, and nearer to integrated design by evaluating overall system loss.

The majority of the work presented in this thesis was focused on the structural components of OWTs, as these had been neglected in the existing literature, but were found to represent potentially large financial losses. Additionally, databases of empirical data, which record failures of real OWTs, were found to be insufficient for the structural components. These databases only contain historical data, and therefore cannot be taken as representative of any changed design which reduces cost by optimising the currently conservative structural capacity. Hence, a numerical approach was used to model

the fragility of OWT structural components following a PBE approach. The focus of this analysis was the ULS and FLS of the primary structural components. The financial losses due to failure in both limit states were quantified and compared to financial losses from the equipment components.

The main contributions provided by this thesis are described in detail in the following paragraphs, and can be summarised as:

- For the ULS - a novel probabilistic risk assessment framework was developed by proposing a computational approach to evaluate structural fragility of OWTs. The probability of failure was evaluated computationally, through a series of limit states which were identified for the important structural components. This analysis used state-of-the art aero-elastic simulation and included uncertainties in the structural demand and capacity. Then a combinatorial method was implemented to evaluate the joint failure of the structure and the equipment that could model the dependencies between components.

- For the FLS - a computationally efficient method for fatigue damage assessment was developed, allowing structural reliability analysis of the structural FLS to be conducted using the full site joint-PDF of environmental conditions.

- A series of case studies were provided, demonstrating applicability of the proposed framework in practice. These evaluated the integrated financial losses arising from failure of the structural and equipment components allowing the identification of those that contributed most to financial loss. This is an essential step towards quantifying resilience by assessing the robustness of an OWT.

The  was assessed by modelling extreme conditions that occur during tropical and extra-tropical cyclones, and that can damage OWTs through large wind speeds and high wave heights. These events have had a devastating impact on some onshore wind turbines [99], but the current design codes for

OWTs only assess environmental conditions up to a 50-year MRP. This is especially low, as equivalent marine structures like oil and gas platforms are commonly assessed using a maximum MRP of 10,000 years.

The study developed a method for calculating the probability of failure of OWT structures exposed to extreme environmental conditions. It was observed that a full calculation of resilience would be difficult to apply at the design stages of an offshore wind project. A practical solution was to assess resilience through the robustness, which could then be used in a later evaluation of resilience. Probabilistic risk modelling was suitable for the ULS, where risk is decomposed into independent components that are combined using total probability theorem and can be used to predict financial losses. Limit states were developed to quantify performance of the main OWT structural components including: the tower, monopile, blades and transition piece. These included a series of random variables which were specified to capture uncertainties in modelling and material properties. This study focused on deriving fragility curves for a reference OWT located at two sites: one in Europe, and one on the East Coast of the USA. Hurricane conditions were experienced at the USA site, meaning that structural failures were observed at relatively low MRP, around 200 for the monopile. However, the relatively mild conditions at the European site meant that structural failures were observed very rarely. Modelling recommendations for the fragility of offshore wind turbine were highlighted through a parametric study. Specifically, the scatter in fragility curve parameters was estimated using statistical resampling, indicating that if the calculation were to be implemented in practice the burden of structural simulations could be reduced.

In European waters, fatigue loading accumulated during operational conditions often drives design of OWTs structural components [156]. However, it is challenging to assess this mode of failure due to the need for computationally expensive time-domain analysis combined with a large number of environmental conditions (i.e, the structural analysis needs to be run a large

number of times). This makes evaluation of FLS complicated, and difficult to implement in a full structural reliability assessment. State-of-the-art design methods simplify the environmental conditions, leading to a granular, and potentially inaccurate, assessment of the fatigue damage [156]. However, surrogate models offer a flexible and computationally tractable solution by allowing assessment of fatigue damage using the full probability distributions of environmental conditions fit to site measured data.

A GP surrogate model was proposed to represent fatigue damage experienced by an OWT monopile. This replaced the computationally expensive structural analysis with a statistical model that was simple to evaluate. The proposed surrogate model was able to include the relevant wind and wave environmental conditions and was found to represent the fatigue damage well on verification analyses run at the site of the three FINO met-masts. A range of different GP kernels were compared and the Matern 5/2 was found to represent fatigue damage best, in agreement with other research [183]. A sensitivity analysis highlighted the acceptable number of samples and seeds, emphasising the potential computational saving in comparison to standard approaches, which may require in the order of 100 times more structural simulations [39].

However, the ULS probabilistic risk modelling approach, of decomposing risk, as used in the ULS assessment, was not used for the fatigue damage estimation. In the FLS, hazard is integral to the prediction of loading, and it was found to be more computationally efficient to evaluate the damage once, than solve the limit state repeatedly for different environmental conditions. Consequently a fatigue limit state equation was developed that included the large material property uncertainty inherent in fatigue damage prediction. This limit state was solved in a single step using Monte Carlo sampling. The reliability assessment indicated a relatively large probability of failure when this calculation was applied to the NREL 5MW OWT at the FINO3 site.

OWTs are systems comprised of multiple components, each of which is necessary for the production of electricity. A method for estimating financial

loss was proposed which can incorporate those caused by structural failure as well as those resulting from failure of the equipment. This approach avoided the need for detailed information about maintenance routines, which may not be available at early stages of the design process.

Additionally, the proposed approach allowed for comparison between failure consequence resulting from the ULS with that from the FLS. For an OWT located in the North Sea, the FLS was found to drive structural financial losses, with the ULS contributing less than 1% to the estimated annual losses. This was primarily a result of the greater probability of occurrence and consequence (cost) of fatigue failure in the monopile. These results suggest that the ULS may be neglected in situations where FLS is found to drive structural loads, such as for OWFs in European waters. However, for an OWF located in a site that is exposed to tropical cyclones, such as on the USA East Coast, the ULS limit state may become critical.

## 7.2 Limitations and future work

### 7.2.1 Ultimate limit state

The case study derived fragility curves which used the MRP as the measure of environmental intensity (IM). This is a metric which combines the wind and wave climate into a single measure of environmental severity, however it assumed that environmental conditions with the same MRP occur simultaneously. This assumption is conservative because in practice a lag between the most severe wind and wave conditions during a storm has been observed [184]. To further advance the framework, a vector IM, which uses multiple parameters, could be utilised to provide a more accurate expression of the environmental hazard.

The fragility curves were based on a simplified structural model, which did not include foundations below the mudline. These have a large influence on the OWT stiffness and a modest impact on OWT loading in the parked state [179]. Additionally, the linear Airy wave model was used to evaluate wave

kinematics for extreme storm waves. This wave model is suitable for assessing small sea-states, such as those experienced during normal operation, but has been found to represent the peaked waves observed during storms poorly [83]. Both of these limitations could be removed by using a different structural model that includes a more suitable foundation [89] and load calculation utilising a different wave model [114]. Both of these factors would have the effect of increasing the fragility of the OWT in its ULS, as the non-linear wave models add additional load and the foundation model would add additional flexibility (however also increasing the damping).

The NREL 5MW OWT is a reference structure commonly used in academic studies. It was designed for a specific site in the Dutch sector of the North Sea, however its dimensions have not been fully optimised. This means that failure rates for the NREL 5MW cannot be taken as representative of structures designed to the current generation of codes for the two case study sites.

The purpose of the case study was to demonstrate the ULS calculation framework and to provide a comparison against the FLS. For both of these objectives the NREL 5MW OWT is a suitable structure. In a future project a spring foundation model will be added into the OpenFAST software [185] framework, allowing simulation of foundation flexibility.

### 7.2.2 Fatigue limit state

The fatigue case study utilised the same structural model as in the ULS study and consequently, the same limitations carry through to the FLS assessment. However, this study added a linear foundation model, in the form of the AF foundations to allow flexibility below the mudline. Misalignment between the wind and wave conditions were modelled, however, only the maximum fatigue loading around the monopile cross-section was extracted for damage calculation. This is a conservative assumption, as multiple fatigue cracks can grow simultaneously around the circumference of the monopile.

The reliability calculation did not include periodic inspections, instead fo-

cusing on assessing the fatigue reliability. Inspections may be able to identify fatigue cracks before they propagate sufficiently to cause failure of the structure, allowing preventative maintenance to take place. However detection of these cracks is difficult, especially for the mudline weld analysed in this study, and therefore it is not certain that they would be identified before reaching a size that threatened the structural integrity of the OWT. The loss calculation focused only on quantifying financial losses in terms of replacement cost. However, for the structural elements, vessel hire would make up a substantial proportion of the repair cost, and would further magnify the importance of the FLS.

Future work could mitigate these limitations by developing more detailed structural models. The structural risk analysis could be used alongside techniques for inspection planning to quantify the trade off between structural reliability and different inspection regimes. However, this would require substantial input from OWF operators regarding their inspection techniques, e.g., what vessels they sent on inspection campaigns.

### 7.2.3 Combined resilience of offshore wind turbines

This study focused on quantifying resilience through robustness and it didn't attempt to quantify resilience over time. Additionally, the work presented in this thesis considered a single OWT whereas multiple OWTs are located in farms comprised of many similar structures. Future work should move from assessing single structures to considering the resilience (robustness, redundancy and recovery characteristics) of OWFs. As OWTs are not designed in isolation, rather they comprise a network of structures exposed to similar (correlated) conditions. Scaling from a single structure to a OWF can be achieved by applying structural analysis combined with advanced probabilistic techniques (including machine learning) at the farm scale. This would allow a rational characterisation of OWF performance and reduce the risk associated with OWT failure through a decision-making tool, which rigorously incorporates uncertainties. Specific tasks that would improve OWT design and allow

assessment of the feasibility of life-extension include:

- From OWT to OWF risk and resilience models: investigating (1) the spatial distribution of site conditions across an OWF, including water-depth and geotechnical properties [166] and, (2) the influence of wake and shielding effects caused by interaction between adjacent OWTs. This could utilise a quantitative sensitivity analysis to rank the conditions that vary across the OWF which have a large impact on structural fragility, risk and resilience of OWTs.

- Structural resilience of an OWF: Through resilience analysis of OWTs located at a small number of different locations across the OWF. The correlation between the fragility of OWT at different locations can be modelled using machine learning techniques, allowing extrapolation to locations not explicitly assessed. It will result in a tool which can define optimal structural properties at different locations across the OWF using a system-level approach, resulting in a consistent level of structural resilience across the farm.

- Cost models for OWFs: This task will develop a parametric model for the cost of different OWT structural components, based on published material costs [156]. This will provide a general plug-in framework to estimate the annual yearly losses across an OWT. Business interruption due to the unavailability of OWT will also be modelled. Monetary loss and business interruption represent easily interpretable metrics for the communication of project risks to stakeholders.

- Economic feasibility of life-extension: Update the OWT / OWF design models with information obtained during the operation of the OWF, e.g., data from inspections and structural monitoring. These will be combined using a Bayesian framework which provides a rational method for updating prior information (the design model) with structural monitoring data

from actual OWTs. Different scenarios, such as continuing full or partial operation, will be used to quantify different end-of-life strategies.

# Appendices

# Appendix A

# Foundation model

## A.1 Introduction

Utility scale OWTs on monopile foundations are supported by large diameter piles which are driven around 30m to 50m into the seabed [186]. The comparatively low stiffness of soil compared to the steel (from which the OWT are constructed) means the upper segment of the pile is not fully restrained, however, for ease of computation foundation flexibility is sometimes neglected in dynamic analysis of OWT. This is especially true in reliability studies where a structural model needs to be run a large number of times where a fixed foundation is commonly assumed [117, 187, 168] for ease of computation. However, including a foundation model has a large impact on the modal properties of the turbine [178] and therefore also on fatigue loading [85]. Although it is still not clear the extent to which the large uncertainties in the soil properties propagate through into variability in the probability of failure of the OWT [85].

Aero-hydro-elastic calculations allows for fully coupled analysis of all relevant OWT degrees of freedom (DOF), including those related to the blades, control system and structure [39]. However, some popular analysis packages, such as FAST [77], do not currently provide integrated analysis of the below seabed foundations. To include the effect of foundation flexibility, the software would need to be modified or a work around solution developed. A further com-

plication is that the number of DOF in aero-elastic codes is limited to around 22 to prevent long analysis run times. Inclusion of a detailed finite element based foundation model would add a large number of DOF and therefore be computationally expensive.

In the existing literature a number of different models to represent foundation flexibility have been implemented into aero-elastic codes including: apparent fixity [179, 188], mudline springs [188, 189, 190], distributed springs [188] and lumped parameter models [191, 192]. Of these the AF is the simplest to implement within FAST, as the foundation simply involves extending the pile below the seabed a predetermined length and can be implemented without any changes to the source code. Selection of the length to extend the pile is problematic, the natural frequency of the OWT substructure is found to be sensitive to this parameter [193] and it is not a physical quantity, but rather simulates flexibility. Two methods for selecting fixity length are: matching the first natural frequency of the OWT with AF to the natural frequency with a real foundation model [193] or changing the pile cross sectional properties to match the average mudline motion under the expected loading [188]. The lumped parameter model (LPM) simplifies the foundation into number of DOF at the mudline, this include springs, damping and internal DOF all of which are linear, but would require source code modification. Using the first method for selecting fixity length Damgaard [179] noted the AF model produced fatigue loading closer to his LPM foundation model than the fixed foundation assumption and therefore provides an improved prediction of the OWT dynamics.

Soil properties are inherently variable and complex, however it is noted that under low strain conditions soil behaves in a visco-elastic manner [194]. Using this assumption soil can be modelled as a linear isotropic material with its behaviour described fully by a stiffness (shear modulus) and damping (loss factor) parameter. However, both these properties are correlated and vary with the mean load level, e.g., Damgaard used mean wind speed [85]. Effects

of cyclic loading on soil stiffness over time is neglected in the current work.

This appendix summarises a linear foundation model developed in Abaqus and how it fits within a broader framework for FLS analysis of an OWT using FAST. The model was verified by (1) matching pile tip displacements to published results and (2) matching the natural frequency to an analytical case which assumes very stiff soil properties, so the pile is effectively fixed at the mudline. At this stage the aim is to include foundation flexibility within FAST using the AF method, a framework for achieving this is proposed. Then the foundation model is included within a larger calculation used to evaluate a FLS equation, which can be run on a high performance computing cluster without an Abaqus license.

## A.2 Foundation models

### A.2.1 Abaqus foundation model

A procedure for creating a FEM of single piles in a soil matrix was proposed by Abdel-Rahman [139], who conducted FEA of soil-structure interaction by embedding a steel pile in a larger cylinder comprised of 3D brick elements. Material properties were selected to represent (the elasto-plastic) behaviour of soil and soil-structure interaction was modelled explicitly through friction interface elements. A similar procedure was used by Mardfekri [112] but the pile was represented using shell elements and the soil had linear-elastic properties with contact between the pile and soil modelled using ties, not friction, resulting in a linear model.

The FEM presented in this report is intended to represent foundations under operational loading, where shear strains are expected to be low [195], in this situation linear-elastic model to represent the soil may be justified as soil behaviour approaches visco-elastic at strain levels below $10^{-4}$. This was modelled using standard 8-noded 3D solid elements. Shell elements (4-noded) were selected for the pile, as opposed to beam elements, so that soil located inside the pile could be explicitly modelled. Contact was modelled by tie

elements, due to the low shear stains non-linearities in the response of the soil were expected to be low. In modal analysis these act as fixed constraint between the pile and soil unless an initial load or displacement is applied which causes a change in the contact stiffness.

The FEM model shown on Figure A.1 the soil matrix has a 90m radius, the pile is embedded 30m and an additional 15m of soil is modelled below the pile toe [139]. The geometrical and material properties of the pile are shown on Table A.1.

### A.2.2 Arany foundation model

A simplified hand calculation for estimating the natural frequency of an OWT was proposed by Arany et al. [196]. A brief outline of the main equations is provided in this section and full details of the calculation can be found in the original paper [196]. The approach is based on simplifying the wind turbine

**Table A.1:** Geometry and material properties of the pile.

| | Pile diameter $(m)$ | Pile thickness $(m)$ | Pile density $(kg/m^3)$ | Pile poisson ratio | Young's modulus $(N/m^2)$ |
|---|---|---|---|---|---|
| Verification | 7.5 | 0.09 | 8050 | 0.200 | $2 \cdot 10^{11}$ |
| NREL 5MW | 6.0 | 0.06 | 8500 | 0.238 | $2 \cdot 10^{11}$ |

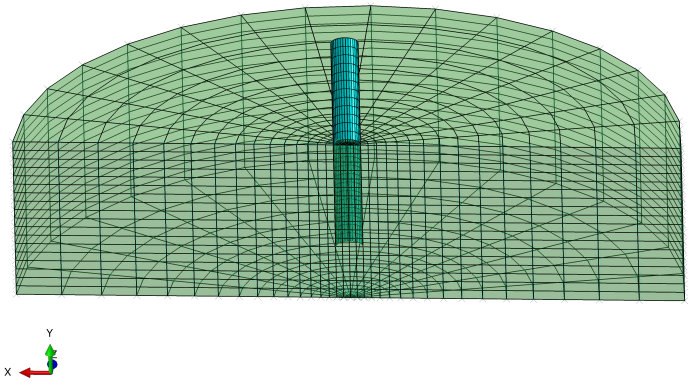


**Figure A.1:** Layout of Abaqus foundation model.

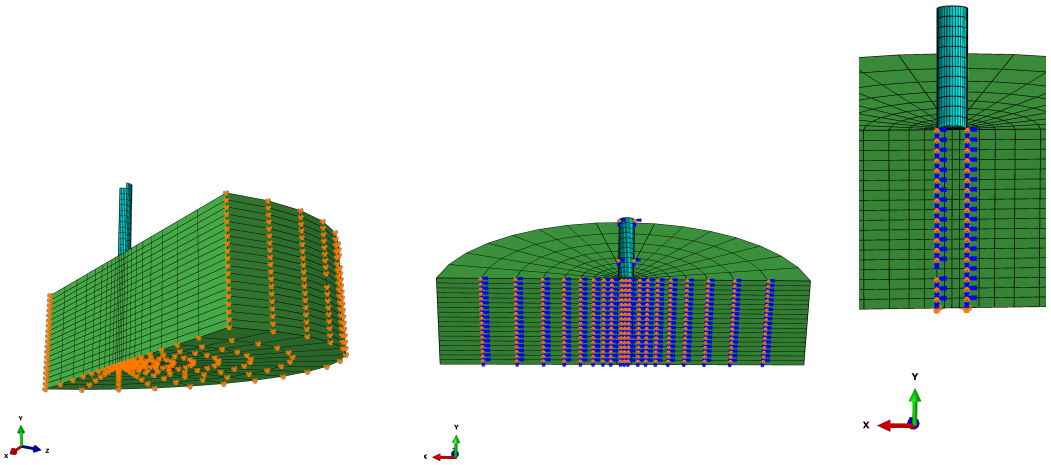

**Figure A.2:** Abaqus boundary conditions and interaction model showing: pinned BD (left), symmetry BD (middle) and contact BC (right). Note: the BC have been properly applied to all nodes 1.

tower to a cantilever beam with top mass, for which an analytical expression exists the calculate the natural frequency ($f_{fb}$)

$$f_{fb} = \frac{1}{2\pi}\sqrt{\frac{k_o}{m_o}}, \tag{A.1}$$

where $k_o$ is the effective stiffness of the tower ($N/m$) and $m_o$ is the effective mass ($kg$). The full OWT natural frequency $f_{OWT}$ ($Hz$) is estimated by multiplying the fixed base tower frequency by coefficients accounting for the lateral foundation resistance ($C_L$), rotational foundation resistance ($C_R$) and the substructure ($C_S$):

$$f_{OWT} = C_L C_R C_S f_{fb}. \tag{A.2}$$

The foundation factors are calculated using non-dimensional stiffness values relating to the lateral stiffness ($\eta_L$), rotational stiffness ($\eta_R$) and cross-stiffness ($\eta_{LR}$), whose calculation is not shown for brevity:

$$C_L = 1 - \frac{1}{1 + 0.5(\eta_R - \eta_{LR}^2/\eta_L)} \tag{A.3}$$

$$C_R = 1 - \frac{1}{1 + 0.6(\eta_L - \eta_{LR}^2/\eta_R)} \tag{A.4}$$

The substructure factor is calculated using the equation:

$$C_S = \sqrt{\frac{1}{1 + (1+\psi)^3\chi - \chi}}. \tag{A.5}$$

It is based on two dimensionless parameters, the bending stiffness ratio ($\chi$) and the length ratio ($\psi$):

$$\chi = \frac{E_T I_T}{E_P I_P} \tag{A.6}$$

$$\psi = \frac{L_S}{L_T} \tag{A.7}$$

Where $E_T$ and $E_P$ are the Young's modulus of the tower and pile ($N/m^2$). $I_T$ and $I_P$ are the second moment of area of the tower and pile ($m^4$). $L_S$ is the length of the sub-structure and $L_T$ is the length of the tower ($m$).

#### A.2.2.1 Input data for Arany foundation model

The calculation described in the previous section requires a information about the geometry of the OWT and the material properties of the tower, monopile and foundation. The tower geometry and the material properties for the structural components are taken from the NREL [42]. The soil properties are taken from the work of Damgaard et al. [85]. These properties are summarised on table A.2.

## A.3 Linear soil material properties

Material properties used to represent soil in this study were taken from Abdel-Rahman [139] (verification) and properties proposed by Damgaard [85] (for

**Table A.2:** Input data used in the Arany foundation model hand calculation

| Variable | Value |
|---|---|
| Tower height (m) | 75.60 |
| Tower diameter top (outer) (m) | 3.87 |
| Tower diameter bottom (outer) (m) | 6.00 |
| Tower thickness average (m) | 0.02 |
| Platform height (m) | 30.00 |
| Monopile diameter (outer) (m) | 6.00 |
| Monopile thickness (m) | 0.06 |
| Mass of rotor nacelle (tonne) | 350.00 |
| Monopile Young's modulus (GPa) | 210.00 |
| Tower Young's modulus (GPa) | 210.00 |
| Tower density (kg/$m^3$) | 7850.00 |
| Soil Young's modulus (Gpa) | 0.17 |
| Soil Poisson ratio | 0.30 |

future work), as shown on Table A.3. The properties used by Abdel-Rahman [139] were non-linear, for use in this work they were linearised by selecting a stiffness modulus ($E_{lin}$) tangential to the initial stiffness from the non-linear model.

## A.4 Foundation verification

### A.4.1 Linear FEA model

Three verification studies were run to ensure that the linear Abaqus model behaved as expected. All geometrical and material properties in this section

**Table A.3:** Material properties for the soil. [1]Calculated using the reference stiffness modulus from the elasto-plastic model and assuming linear material property relationship $G_s = E_{lin}/(2 \cdot (1+\nu))$ with $E_{lin} = 6 \cdot 10^4 kPa$; [2]Calculated from the soil unit weight $\gamma_{soil} = 11.0 kN/m^3$; [3]Variables correlated using correlation matrix

| | Shear modulus $G_s$ $(KPa)$ | Poission's ratio $\nu$ $(KPa)$ | Density $\rho$ $(kg/m^3)$ | Loss factor $\eta$ |
|---|---|---|---|---|
| Verification, linearised | 2.4$e$4 [1] | 0.25 | 1121.3 [2] | n/a |
| Proposed for future work | Mean = 1.7$e$4; CoV = 0.4; Distribution = Log-normal | 0.3 | Mean = 1700; CoV = 0.07; Distribution = Log-normal | Mean = 0.05; CoV = 0.4; Distribution = Log-normal |

relate to the verification case listed on Table A.1 and Table A.3, unless otherwise defined.

Firstly, a parametric study was run to ensure the dimensions of the soil matrix or the mesh density did not influence the natural frequency. Convergence was assessed using the gradient between natural frequency calculated at different parameter inputs. In some cases the limits of the parametric study (e.g. the maximum mesh density) were determined by computational resources (i.e., a laptop with 8Gb RAM):

- Soil matrix mesh density - default mesh element size = 1.4m linearly varying to 20.0m (at outside of matrix), the inner element size was varied [8 0.4]m. Default value had a local gradient below 0.01 Hz/m and was used in further studies.

- Pile/Soil interface mesh density - default = 16 elements around radius (6m) and 18 down pile depth (30m). Gradient 0.003 Hz/element from default number of elements around radius. Natural frequency not sensitive to number of elements along depth of pile.

- Soil radius - varied between [90 190]m. Change in natural frequency below between extremes was 0.2%, natural frequency not sensitivity to radius therefore use 90m.

- Soil depth - varied between [45 80]m. Change in natural frequency below 0.2% between extremes used 45m in further analysis.

- Boundary conditions around soil perimeter changed from pinned to sliding. Change 0.01%, probably not much influence due to the large diameter soil matrix.

As noted previously the embedded length of the pile is 30m, a sensitivity study run with pile embedded lengths $l_{emb} = [27.5 : 2.5 : 45.0]m$ resulted in a 2.5% change to the predicted natural frequency between the maximum and minimum embedded length. From this we concluded that FEA model is

insensitive to this parameter and that variability in it can be neglected from further studies.

Secondly, mudline displacements from the linear Abaqus model were compared to those from, more complex, published numerical tests by Abdel-Rahman [139] of a monopile responding to a static load. The purpose of this comparison was to verify that the pile displacements were approximately correct for the load levels expected during operation of the OWT. Abdel-Rahman [139] developed two FEA models; one with properties based on API p-y curves and another non-linear model with elastic-plastic soil (i.e. stiffness varies with stress) and friction contact elements representing pile-soil interaction. Displacements were introduced by applying a static horizontal point load to the upper face of the pile at El+30m, and the corresponding mudline displacement recorded. For low load levels the mudline displacement matched Abdel-Rahman's output well, with results diverging as the applied load increased, Figure A.3. The linear Abaqus results are a good match to the load displacement relationship derived from API p-y curves, which are non-linear but at the low strain to diameter ratio situations modelled [139] they approach linear behaviour. For comparison, the average load on an operational NREL 5MW turbine at $V_w = 12m/s$ is around $2.2MN$ and at $V_w = 24m/s$ around $1.4MN$, therefore non-linear soil effects (constitutive and interaction) are not expected to have a significant impact on FLS response during operational wind speeds.

The third validation test compared natural frequency of the linear Abaqus model (modified to have very high shear modulus) with that predicted analytically for a OWT fixed at the mudline using: (1) hand-calculation proposed by Arany [15] ($\omega_{n,FA1} = 7.5737Hz$) and (2) the FAST linear frame finite-element beam module SubDyn [17] ($\omega_{n,FA1} = 7.5691Hz$). The shear modulus of the soil was increased to a large value, approximating fixed BC, the first fore-aft natural frequency of the linear Abaqus model converged to $\omega_{n,FA1} = 7.5734Hz$. This verifies that the representing the pile as a shell with kinematic constraints

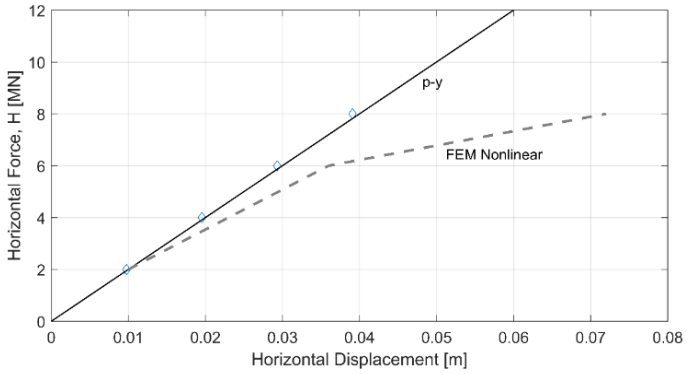


**Figure A.3:** Verification of pile mudline displacements against Abdel-Rahman results. Results from linear Abaqus model are shown as blue diamonds.

on its upper face similarly to a beam element with equivalent properties expected.

### A.4.2 Fixed and flexible at seabed

Different chapters of the thesis used different assumptions regarding the foundation fixity. The ULS application (Chapter 4) used a model with a fixed-base foundation in comparison to the FLS application (Chapter 6) which included a linear foundation model. This section assesses the difference between these two approaches, where the results have been calculated using the properties presented on Table A.2.

Including a foundation model reduces the stiffness of the structure and therefore also its natural frequency. Consequently, a structural analysis without a foundation model may underestimate the maximum loading, as the peak of the wind and wave spectra, which drive structural loading, are typically below the natural frequency of the OWT. Not to modelling the foundation may also be over-conservative if it pushes the natural frequency into the range of frequencies at which the blade passes the tower (3P range), see Section 2.3.

The natural frequency of the NREL 5MW OWT was calculated using the method proposed by Arany et al. [196], and described previously. The natural frequency with no foundation model was 0.271Hz and the natural frequency if a foundation is included was 0.214Hz, a 27% difference. The 3P frequency for the NREL 5MW OWT is 0.35Hz, meaning that the fixed bottom assumption

does not make the structural model impinge upon the operational frequencies of the rotor. It should also be noted that during ULS analysis utilised in this thesis the turbine was not operational.

The error caused with respect to the loading frequencies by assuming the turbine has a fixed foundation can be quantified by calculating the dynamic amplification factor ($D$), using [157]:

$$D = \frac{1}{\sqrt{(1-\beta^2)^2 + (2\eta\beta)^2}}. \tag{A.8}$$

Where $\eta$ is the damping ratio and $\beta$ is the ratio of the applied loading frequency to the natural free-vibration frequency.

A fixed damping ratio of 0.03 is assumed for a parked OWT following Chen and Duffour [86]. Dynamic amplification therefore depends only on the ratio between the natural frequency (calculated in the previous paragraph) and the applied loading. Environmental loading spectra for typical operating conditions are shown in Figure A.4 (left) and the mildest storm conditions from Chapter 4 are shown in Figure A.5 (left). The large difference in dynamic amplification factor between the fixed and foundation cases in Figure A.4 (right) indicates modelling a foundation is vital in order to correctly capture the operating wind conditions. However the small difference in Figure A.5 (right) indicates that for extreme conditions, characterised by high period waves, modelling foundations has a smaller impact. This is further emphasised in Figure A.6 which shows the difference between dynamic amplification factors assuming a fixed base and a foundation over a range of loading frequencies, the error grows large when the loading frequency is above 0.1Hz. From Figure A.5 it is observed that the peak in the wave load spectrum occurs below 0.1Hz.

## A.5 Fatigue calculation with foundation

This section describes how the linear foundation model was included within the fatigue calculation work-flow. The foundation element of the calculation is shown on Figure A.7, which uses properties, Table A.3, as inputs. The aim was

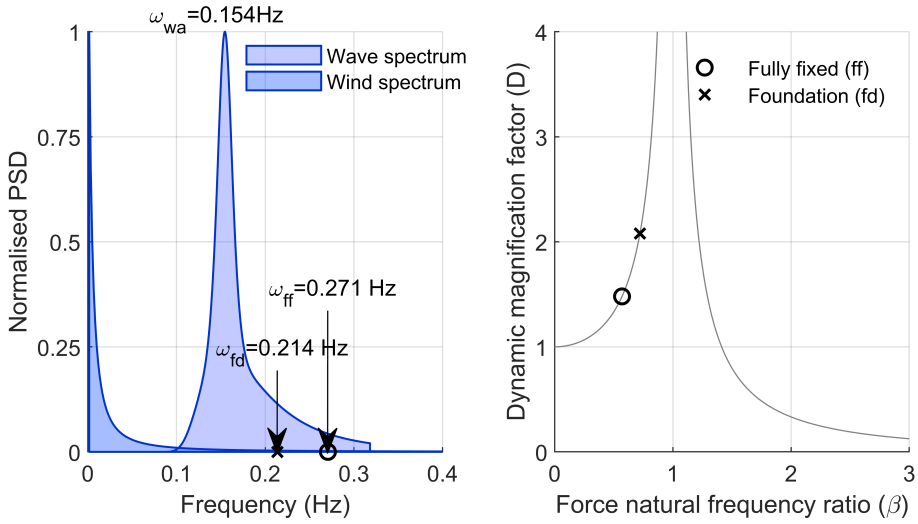


**Figure A.4:** Load spectra (left) and dynamic amplification factor (right). Assuming mean wind speed of 10m/s, significant wave of 3m and peak spectral period using Eq.(4.4).

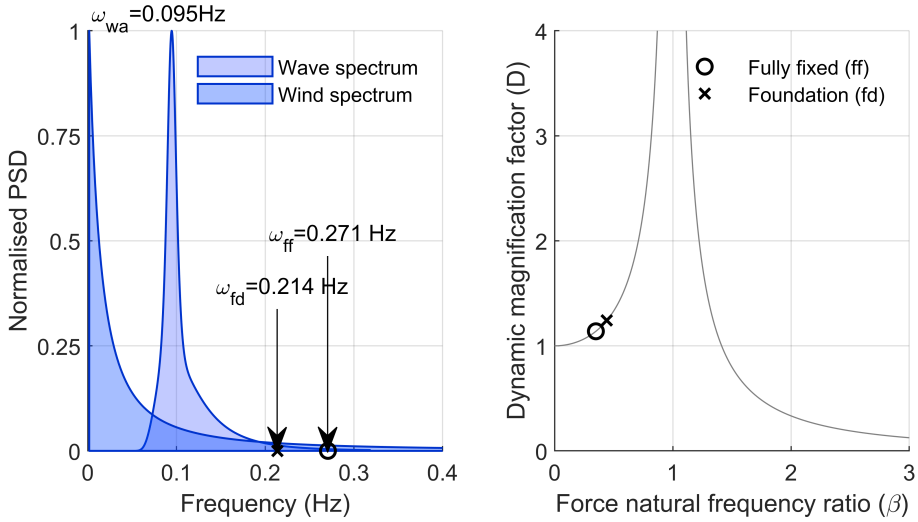


**Figure A.5:** Load spectra (left) and dynamic amplification factor (right). Assuming mean wind speed of 40m/s, significant wave of 10m and peak spectral period using Eq.(4.4).

to run this analysis on Legion, the UCL high performance computing cluster, which does not have Abaqus installed. A custom Matlab script was developed to predict the first eigenvalue of the OWT with soil properties ($\omega_{1,FA}$). This uses the p-y curve method and was verified against the Abaqus model. The natural frequency is extracted and used in an iterative calculation to determine the correct apparent fixity length to use in FAST. The iterations stop when

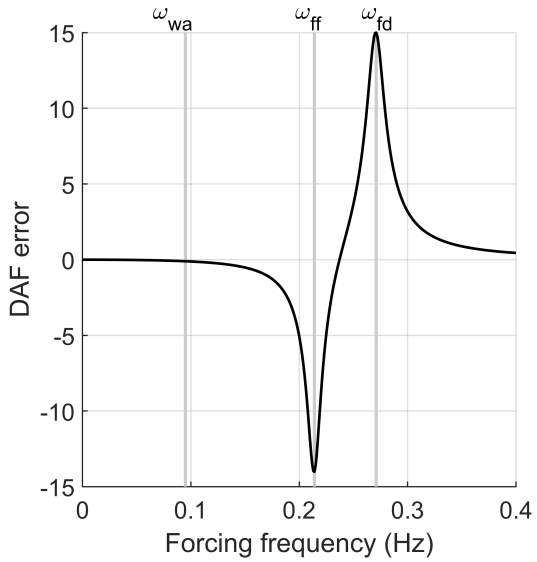


**Figure A.6:** Difference between fixed base and foundation dynamic amplification factor.

the natural frequency of the AF model matches that from the linear Abaqus model within a threshold (of $1^{-4}$). Separately, a linear damping coefficient is calculated using the soil damping ratio and the pile natural frequency which is applied to the transition piece node.

The aim was to run this analysis on Legion, the UCL high performance computing (HPC) cluster, which does not have Abaqus installed. A series of functions were written to enable this work flow and output estimates of fatigue damage. The function was written in Matlab but utilises to call some external programs:

- SubDyn, A linear frame finite element solver. It generates lumped stiff-

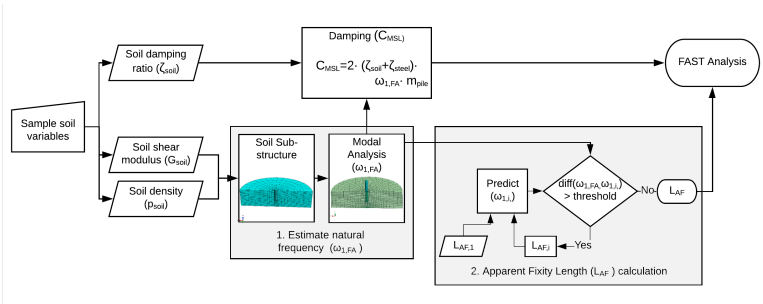


**Figure A.7:** FAST calculation work-flow including pile with AF method.

ness and mass matrices representing the substructure, which are required to in order to calculate the tower mode shape. These quantities change when the stiffness of the soil properties change.

- BModes, A finite-element package that calculates the frequencies and mode shapes of a circular hollow section tapered beam with an offset tip mass. This is used to calculate the tower mode shapes, which are necessary as FAST uses the Rayleigh-Ritz method to calculate the tower response.

- Turbsim, Generates a turbulent wind time history which is an input to FAST.

- FAST, Calculates time history response of the OWT to internally generated waves and the wind speed time series generated by Turbsim.

The HPC cluster utilises the Linux operating system, FAST and Turbsim were installed and tested but SubDyn and BModes proved difficult to install. The functionality provided by these programs was rewritten as custom Matlab functions:

- SubDyn to fem_OWTPy

- BModes to fem_Tower

Allowing the full fatigue calculation to be carried out on Legion. The purpose of this section is to describe the layout of the Dmg_WrapFun function then verify that the fem_MPile and fem_Tower functions provide accurate results.

### A.5.1 Function layout

The layout of "Dmg_WrapFun" is shown on Figure A.8, this wrapper function takes site data, realisations of random variables and the natural frequency regression model then calculates the resulting fatigue damage arising from an hours worth of dynamic simulation. The input data is:

- Site - Mean wind speed, significant wave height, peak spectral period and turbulence intensity.
- Nf_reg – Natural frequency regression model from Abaqus.
- X - Samples of the soil shear modulus and damping.

Computation within Dmg_WrapFun is split across 3 main calculation functions (starting "fun_" in Figure A.8) each of which has its own dependencies:

- fun_Laf - Iteratively calculates the apparent fixity length that will reproduce the same natural frequency the Abaqus foundation model (using NF_Diff and fem_MPile). Also calculates equivalent stiffness and mass matrices for the substructure at the transition point, i.e. the lowest tower node (using fem_MPile).
- fun_FASTRun - Pre-process and initiate an hour long FAST analysis of the OWT with the apparent fixity depth calculated in fun_Laf. This function starts by calling Turbsim to generate a turbulent wind time history (Turbsim) then updates the tower mode shapes based on substructure flexibility (fem_Tower) and prepares FAST input files (all FAST_ functions). The final line in fun_FASTRun runs FAST.
- fun_ImpRFC - Imports data from the output file produced by FAST (Import_FzMxMy) and converts the mudline reaction forces into a stress time history (Pr_Stress_Mn), finally calling the WAFO toolbox [197] to conduct rainflow counting on the time history. The fatigue damage is then estimated.

### A.5.2 Description of fem_Tower

This function models the OWT tower as a beam supported by the Monopile substructure with the hub represented as a point mass offset form the top tower node, indicated on Figure A.11 (right). The purpose is to calculate the

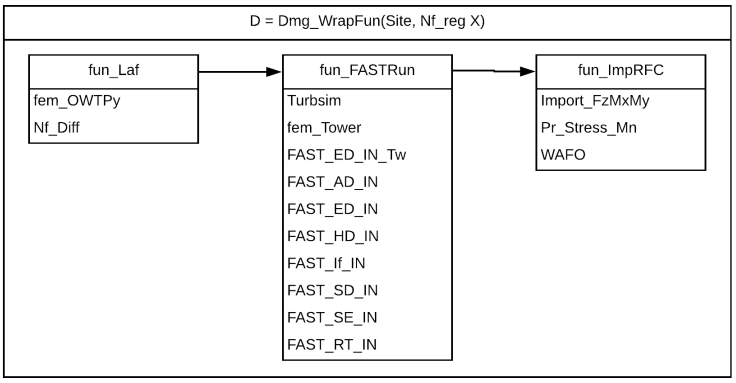


**Figure A.8:** Function dependencies of Dmg_WrapFun.

coefficients of a 6th order polynomial that is fit to the tower mode shape, a required input for FAST.

The tower has a tapered diameter and wall thickness which is discretized into concentric uniform segments with constant diameter and wall thickness. A 12 DOF Timoshenko beam elements [198] are used, to be consistent with BModes [199], the element matrices are shown in Figure A.9 and A.10, the coordinate system is shown on Figure A.11 (left).

The lower BC is restrained by the substructure, therefore the equivalent mass and stiffness matrices, produced by "fem_MPile" function, are added to DOF associated with the tower base node.

The upper BC, located at the tower tip is free. The mass matrix is changed

$$[k_e] = \begin{bmatrix}
\frac{12EJ_y}{L_e^3(1+K_m)} & 0 & 0 & 0 & \frac{6EJ_y}{L_e^2(1+K_m)} & 0 & -\frac{12EJ_y}{L_e^3(1+K_m)} & 0 & 0 & 0 & \frac{6EJ_y}{L_e^2(1+K_m)} & 0 \\
 & \frac{12EJ_x}{L_e^3(1+K_m)} & 0 & \frac{-6EJ_x}{L_e^2(1+K_m)} & 0 & 0 & 0 & -\frac{12EJ_x}{L_e^3(1+K_m)} & 0 & \frac{-6EJ_x}{L_e^2(1+K_m)} & 0 & 0 \\
 & & \frac{EA_x}{L_e} & 0 & 0 & 0 & 0 & 0 & -\frac{EA_x}{L_e} & 0 & 0 & 0 \\
 & & & \frac{(4+K_m)EJ_y}{L_e(1+K_m)} & 0 & 0 & 0 & \frac{6EJ_x}{L_e^2(1+K_m)} & 0 & \frac{(2-K_m)EJ_x}{L_e(1+K_m)} & 0 & 0 \\
 & & & & \frac{(4+K_m)EJ_y}{L_e(1+K_m)} & 0 & -\frac{6EJ_y}{L_e^2(1+K_m)} & 0 & 0 & 0 & \frac{(2-K_m)EJ_y}{L_e(1+K_m)} & 0 \\
 & & & & & \frac{GJ_x}{L_e} & 0 & 0 & 0 & 0 & 0 & -\frac{GJ_x}{L_e} \\
 & & & & & & \frac{12EJ_y}{L_e^3(1+K_m)} & 0 & 0 & 0 & -\frac{6EJ_y}{L_e^2(1+K_m)} & 0 \\
 & & & & & & & \frac{12EJ_x}{L_e^3(1+K_m)} & 0 & \frac{6EJ_x}{L_e^2(1+K_m)} & 0 & 0 \\
 & & & & & & & & \frac{EA_x}{L_e} & 0 & 0 & 0 \\
 & & & & & & & & & \frac{(4+K_m)EJ_x}{L_e(1+K_m)} & 0 & 0 \\
 & & & & & & & & & & \frac{(4+K_m)EJ_y}{L_e(1+K_m)} & 0 \\
 & & & & & & & & & & & \frac{GJ_x}{L_e}
\end{bmatrix} \quad (9)$$

**Figure A.9:** Element stiffness matrix.

$$[m_e] = \rho \begin{bmatrix} \frac{13A_eL_e}{35} + \frac{6J_y}{5L_e} & 0 & 0 & 0 & \frac{11A_eL_e^2}{210} + \frac{J_y}{10} & 0 & \frac{9A_eL_e}{70} - \frac{6J_y}{5L_e} & 0 & 0 & 0 & \frac{13A_eL_e^2}{420} + \frac{J_y}{10} & 0 \\ & \frac{13A_eL_e}{35} + \frac{6J_x}{5L_e} & 0 & \frac{11A_eL_e^2}{210} - \frac{J_x}{10} & 0 & 0 & 0 & \frac{9A_eL_e}{70} - \frac{6J_x}{5L_e} & 0 & \frac{13A_eL_e^2}{420} - \frac{J_x}{10} & 0 & 0 \\ & & \frac{A_eL_e}{3} & 0 & 0 & 0 & 0 & 0 & \frac{A_eL_e}{6} & 0 & 0 & 0 \\ & & & \frac{A_eL_e^3}{105} + \frac{2L_eJ_x}{15} & 0 & 0 & 0 & \frac{13A_eL_e^2}{420} + \frac{J_x}{10} & 0 & -\frac{A_eL_e^3}{140} - \frac{L_eJ_x}{30} & 0 & 0 \\ & & & & \frac{A_eL_e^3}{105} + \frac{2L_eJ_y}{15} & 0 & \frac{13A_eL_e^2}{420} - \frac{J_y}{10} & 0 & 0 & 0 & -\frac{A_eL_e^3}{140} - \frac{L_eJ_y}{30} & 0 \\ & & & & & \frac{J_xL_e}{3} & 0 & 0 & 0 & 0 & 0 & \frac{J_xL_e}{6} \\ & & & & & & \frac{13A_eL_e}{35} + \frac{6J_y}{5L_e} & 0 & 0 & 0 & \frac{11A_eL_e^2}{210} - \frac{J_y}{10} & 0 \\ & & & & & & & \frac{13A_eL_e}{35} + \frac{6J_x}{5L_e} & 0 & \frac{11A_eL_e^2}{210} + \frac{J_x}{10} & 0 & 0 \\ & & & & & & & & \frac{A_eL_e}{3} & 0 & 0 & 0 \\ & & & & & & & & & \frac{A_eL_e^3}{105} + \frac{2L_eJ_x}{15} & 0 & 0 \\ & & & & & & & & & & \frac{A_eL_e^3}{105} + \frac{2L_eJ_y}{15} & 0 \\ & & & & & & & & & & & \frac{J_xL_e}{3} \end{bmatrix} \quad (10)$$

**Figure A.10:** Element mass matrix.

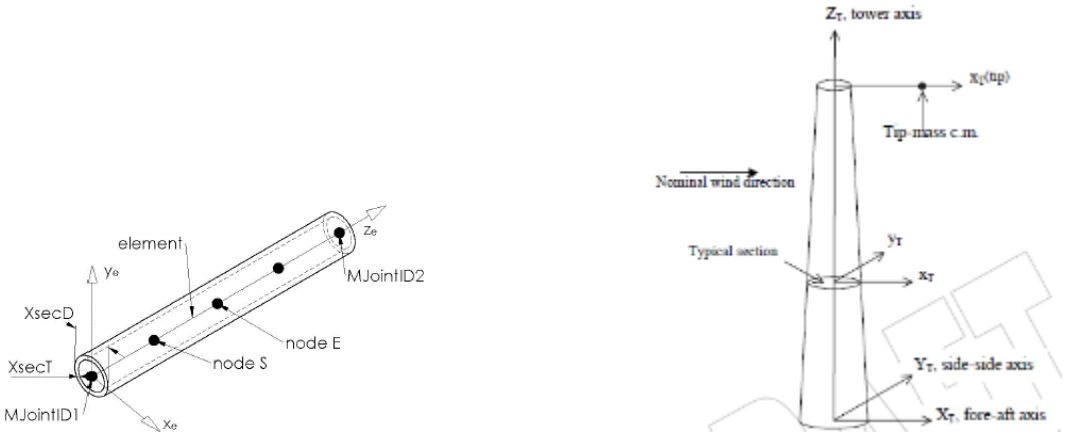


**Figure A.11:** Diagram showing coordinate system, with a beam comprised of 4 elements (left) and tower coordinate system [17] (right).

to include the influence of hub inertia. The hub mass ($m_{hub}$) was added to all the translational DOF. The hub moments of inertia had been previously calculated about its centre of mass ($I_{tx}$, $I_{txz}$, $I_{tzx}$, $I_{tz}$) by NREL and were translated into the tower centreline using parallel axis theorem where necessary (with $r$ the distance between the hub centre of mass and the centreline of the tower). The resulting mass matrix which was added to the upper BC node took the form:

$$M_{tip} = \begin{Bmatrix} m_{hub} & 0 & 0 & 0 & 0 & 0 \\ 0 & m_{hub} & 0 & 0 & 0 & 0 \\ 0 & 0 & m_{hub} & 0 & 0 & 0 \\ 0 & 0 & 0 & I_{tx} & 0 & I_{tzx} \\ 0 & 0 & 0 & 0 & I_{ty} + m_{hub} \cdot r^2 & 0 \\ 0 & 0 & 0 & I_{txz} & 0 & I_{tz} + m_{hub} \cdot r^2 \end{Bmatrix} \quad \text{(A.9)}$$

The natural frequencies of the substructure are then calculated using the eigenvalue solver built-in to Matlab. In a final step a 6th order polynomial is fit to mode shape, so that the coefficients can be input to FAST:

$$f(x) = C_0 + C_1 \cdot x + C_2 \cdot x^2 + C_3 \cdot x^3 + C_4 \cdot x^4 + C_5 \cdot x^5 + C_6 \cdot x^6 \quad \text{(A.10)}$$

The first-order coefficient ($C_1$) and constant term ($C_0$) are deleted as these are insignificant. Tower modal properties in the format required by FAST are calculated by normalizing the remaining coefficients so that they sum to 1.

The function also calculates cross sectional properties for the tower at 11 elevations including: mass density, flexural rigidity and cross section area which are required by FAST.

The function outputs are: the unmodified mode shapes, natural frequencies, normalised mode shape coefficients and the tower cross-sectional properties. The latter two outputs are necessary to run FAST.

### A.5.3 Description of fem_OWTPy

This function models the full OWT as a series of Timoshenko beam elements and outputs the natural frequency, and equivalent stiffness and mass matrices. This is achieved using the built-in Matlab eigenvalue solver combined with Guyan reduction, as described in the following paragraphs.

The model of the wind turbine tower is the same as used in fem_Tower,

so will not be described.

The 12 DOF Timoshenko beam elements, shown in Figure A.9 and A.10, are built into global a matrix representing the entire substructure (from the bottom of the pile to the tower top).

The BC for the below mudline pile can either be rigid or restrained by distributed linear springs. In the rigid case the DOF below the mudline are deleted from the global mass and stiffness matrices. In the spring case, soil stiffness is modelled as linear translational springs distributed at nodes along the pile using the method described by ISO [97] to calculate spring stiffness. The pile toe is restrained in the vertical and rotational directions.

The upper BC is free, no modification.

The global stiffness matrix is condensed into an equivalent matrix with a reduced number of DOF using Guyan reduction (also known as static condensation [200]) to calculate equivalent 6DOF global stiffness matrices where only DOF associated with the upper node are retained. This is achieved by segmenting the stiffness matrix into retained DOF ($K_{11}$ 6-by-6) and discarded DOF ($K_{22}$):

$$\underline{K} = \begin{bmatrix} K_{11} & K_{12} \\ K_{21} & K_{22} \end{bmatrix} \tag{A.11}$$

With a translation matrix defined:

$$T_r = \begin{Bmatrix} I \\ K_{22}^{-}2 \cdot K_{21} \end{Bmatrix} \tag{A.12}$$

Which was used to calculate the equivalent stiffness and mass matrices:

$$\underline{K_{eq}} = T_r^T \cdot \underline{K} \cdot T_r \tag{A.13}$$

$$\underline{M_{eq}} = T_r^T \cdot \underline{M} \cdot T_r \tag{A.14}$$

The natural frequencies of the substructure are then calculated using the

eigenvalue solver built-in to Matlab to solve:

$$(\underline{K_{eq}} - \underline{\lambda} \cdot \underline{M_{eq}}) \cdot \underline{\Phi} = 0 \tag{A.15}$$

The function outputs both the equivalent matrices ($M_{eq}$ and $K_{eq}$) and the first natural frequency ($\sqrt{\lambda_1}$).

### A.5.4 Verification

The function was verified using the standard NREL 5MW turbine monopile geometry [42] with an apparent fixity length equal to 5.9846m (the total monopile length is therefore 35.9846m).

The first natural frequency match well between fem_OWTPy and SubDyn, which predict 4.296Hz and 4.256Hz respectively (difference less than 1%). Also the equivalent stiffness and mass matrices agree well, as indicated on Table A.4, with the majority of the diagonal terms matching to three decimal places.

Additionally verification of the natural frequency of the NREL 5MW with foundation properties values published by Myers et al. [14] and Carswell et al. [201] indicate the fem_OWTPy calculation is accurate.

**Table A.4:** Comparison of equivalent stiffness and mass matrix produced by SubDyn and custom Matlab script.

| | | fem_Mpile | | | | | | SubDyn | | | | | |
|---|---|---|---|---|---|---|---|---|---|---|---|---|---|
| | | x | y | z | xx | yy | zz | x | y | z | xx | yy | zz |
| Equivalent stiffness | x | 2.16E8 | 0 | 0 | 0 | -3.89E9 | 0 | 2.16E8 | 0 | 0 | 0 | -3.89E9 | 0 |
| | y | 0 | 2.16E8 | 0 | 3.89E9 | 0 | 0 | 0 | 2.16E8 | 0 | 3.89E9 | 0 | 0 |
| | z | 0 | 0 | 6.38E9 | 0 | 0 | 0 | 0 | 0 | 6.38E9 | 0 | 0 | 0 |
| | xx | 0 | 3.89E9 | 0 | 9.80E10 | 0 | 0 | 0 | 3.89E9 | 0 | 9.80E10 | 0 | 0 |
| | yy | -3.89E9 | 0 | 0 | 0 | 9.80E10 | 0 | -3.89E9 | 0 | 0 | 0 | 9.80E10 | 0 |
| | zz | 0 | 0 | 0 | 0 | 0 | 2.22E10 | 0 | 0 | 0 | 0 | 0 | 2.22E10 |
| Equivalent mass | x | 1.26E5 | 0 | 0 | 0 | -6.23E5 | 0 | 1.26E5 | 0 | 0 | 0 | -6.22E5 | 0 |
| | y | 0 | 1.26E5 | 0 | 6.23E5 | 0 | 0 | 0 | 1.26E5 | 0 | 6.22E5 | 0 | 0 |
| | z | 0 | 0 | 1.14E5 | 0 | 0 | 0 | 0 | 0 | 1.14E5 | 0 | 0 | 0 |
| | xx | 0 | 6.23E5 | 0 | 4.24E6 | 0 | 0 | 0 | 6.22E5 | 0 | 4.24E6 | 0 | 0 |
| | yy | -6.23E5 | 0 | 0 | 0 | 4.24E6 | 0 | -6.22E5 | 0 | 0 | 0 | 4.24E6 | 0 |
| | zz | 0 | 0 | 0 | 0 | 0 | 1.01E6 | 0 | 0 | 0 | 0 | 0 | 1.01E6 |

The function was verified by comparing the normalised mode shape coefficients and the tower cross-sectional properties. Results for the tower cross-sectional properties are not shown here, but were found to match the NREL certification tests well.

The mode shape coefficient test took the same geometry as used previously and used the equivalent mass and stiffness matrices shown on Table A.5. The first two FA and SS natural frequencies and modes shapes predicted using fem_Tower and BModes are compared in Table A.5. The first coefficients ($C_2$) match well but significant differences occur between some of the higher order coefficients. When we investigate the actual mode shape predicted by these coefficients, shown on Figure A.12, they match well, particularly the first mode. The coefficients are normalised therefore the mode shapes are equal when $x = 1$. Additionally the higher order terms are less important over the majority of the range $0 \leq x \leq 1$, which mitigates against the large differences in these coefficients.

From this it can be seen that the fem_Tower calculation is sufficiently accurate.

**Table A.5:** Comparison of mode natural frequencies and corresponding mode shape coefficients from "fem_Tower" and BModes. The difference between the two methods are shown at the bottom. Note: coefficients match Eq. (A.10).

| | | Natural Frequency (Hz) | Mode Shape Coefficients | | | | |
|---|---|---|---|---|---|---|---|
| | | | $C_2$ | $C_3$ | $C_4$ | $C_5$ | $C_6$ |
| fem_Tower | FA1 | 0.315 | 0.973 | 0.172 | -0.169 | 0.125 | -0.101 |
| | FA2 | 2.267 | 31.026 | -10.977 | -20.660 | -0.883 | 2.494 |
| | SS1 | 0.311 | 0.962 | 0.177 | -0.167 | 0.127 | -0.099 |
| | SS2 | 1.805 | 16.551 | -4.742 | -10.840 | 1.010 | -0.978 |
| BModes | FA1 | 0.339 | 0.981 | 0.138 | -0.110 | 0.076 | -0.086 |
| | FA2 | 2.363 | 29.955 | -12.312 | -16.258 | -3.652 | 3.267 |
| | SS1 | 0.335 | 0.971 | 0.142 | -0.106 | 0.076 | -0.083 |
| | SS2 | 1.896 | 16.365 | -5.652 | -8.688 | -0.571 | -0.455 |
| Difference | FA1 | -0.024 | -0.008 | 0.034 | -0.059 | 0.049 | -0.016 |
| | FA2 | -0.096 | 1.070 | 1.335 | -4.402 | 2.769 | -0.773 |
| | SS1 | -0.024 | -0.008 | 0.035 | -0.061 | 0.051 | -0.016 |
| | SS2 | -0.091 | 0.185 | 0.910 | -2.153 | 1.581 | -0.523 |
| Difference (%) | FA1 | 7.76 | 0.821 | 19.532 | -35.021 | 39.337 | -15.545 |
| | FA2 | 4.22 | 3.450 | -12.161 | -21.307 | -313.503 | 30.969 |
| | SS1 | 7.65 | 0.853 | 19.559 | -36.647 | 40.333 | -16.571 |
| | SS2 | 5.06 | 1.118 | -19.191 | -19.858 | 156.484 | -53.480 |

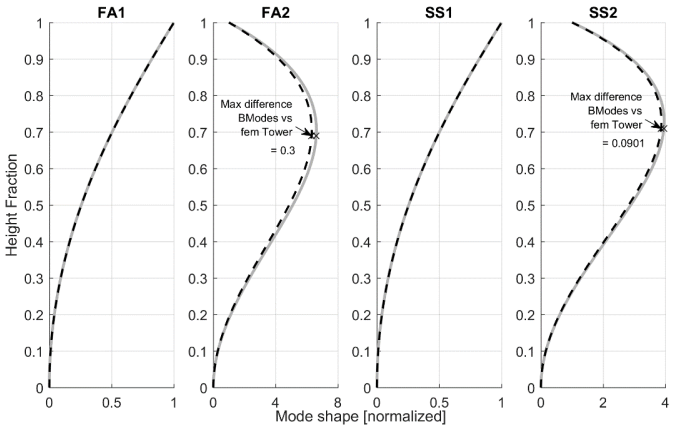


**Figure A.12:** Comparison between the normalized mode shapes predicted using BModes (black) and fem_Tower function (grey).

# Bibliography


[1] "World offshore wind potential." https://openei.org/wiki/. Accessed: 14/05/19.

[2] F. Selot, D. Fraile, and G. Brindley, "Offshore wind in europe; key trends and statistics 2018," tech. rep., Wind Europe, 2018.

[3] T. Stehly, D. Heimiller, and G. Scott, "2016 cost of wind energy review," tech. rep., NREL, 2016.

[4] "Europe powered by green energy: How the north seas can lead the change," tech. rep., Orsted, 2019.

[5] G. Clark, "Industrial strategy offshore wind sector deal," tech. rep., HM Government, Department for Business, Energy & Industrial Strategy, 2019.

[6] International Electrotechnical Commission, "IEC 61400-3. Wind turbines - Part 3: design requirements for offshore wind turbines," 2009.

[7] G. P. Cimellaro, A. M. Reinhorn, and M. Bruneau, "Seismic resilience of a hospital system," *Structure and Infrastructure Engineering*, vol. 6, pp. 127–144, feb 2010.

[8] K. A. Porter, "An overview of PEER's performance-based earthquake engineering methodology," *9th International Conference on Applications of Statistics and Probability in Civil Engineering*, vol. 273, no. 1995, pp. 973–980, 2003.

[9] S. K. Au and Y. Wang, *Engineering risk assessment with subset simulation*. Singapore: John Wiley & Sons, 2014.

[10] J. Carroll, A. McDonald, and D. McMillan, "Failure rate, repair time and unscheduled O&M cost analysis of offshore wind turbines," *Wind Energy*, vol. 19, pp. 1107–1119, aug 2015.

[11] T. Burton, N. Jenkins, D. Sharpe, and E. Bossanyi, *Wind energy handbook*. John Wiley & Sons, Ltd, may 2011.

[12] I. van der Hoven, "Power spectrum of horizontal wind speed in the frequency range from 0.0007 to 900 cylces per hour," *Journal of Meteorology*, vol. 14, pp. 160–164, apr 1957.

[13] E. Simiu, *Design of buildings for wind: a guide for ASCE 7-10 standard users and designers of special structures*. John Wiley & Sons, 2nd ed., 2011.

[14] A. Myers, S. Arwade, V. Valamanesh, S. Hallowell, and W. Carswell, "Strength, stiffness, resonance and the design of offshore wind turbine monopiles," *Engineering Structures*, vol. 100, pp. 332–341, oct 2015.

[15] L. Arany, S. Bhattacharya, J. H. Macdonald, and S. J. Hogan, "Closed form solution of eigen frequency of monopile supported offshore wind turbines in deeper waters incorporating stiffness of substructure and SSI," *Soil Dynamics and Earthquake Engineering*, vol. 83, pp. 18–32, apr 2016.

[16] J. Schijve, *Fatigue of structures and materials*. Amsterdam: Springer Science + Buisiness Media, 2nd ed., 2009.

[17] R. Damiani, J. Jonkman, and G. Hayman, "Subdyn user's guide and theory manual," tech. rep., NREL, Denver, 2015.

[18] K. Wei, S. Arwade, A. Myers, S. Hallowell, J. Hajjar, E. Hines, and W. Pang, "Toward performance-based evaluation for offshore wind tur-

bine jacket support structures," *Renewable Energy*, vol. 97, pp. 709–721, nov 2016.

[19] C. Hübler, C. G. Gebhardt, and R. Rolfes, "Development of a comprehensive database of scattering environmental conditions and simulation constraints for offshore wind turbines," *Wind Energy Science*, vol. 2, pp. 491–505, oct 2017.

[20] S. Azau and R. Bianchin, "Wind in our sails; the coming of Europe's offshore wind industry," tech. rep., The European Wind Energy Association, 2011.

[21] "History of europe's wind industry." https://windeurope.org/about-wind/history/. Accessed: 01-05-2019.

[22] C. Stark, M. Thompson, T. Andrews, G. Beasley, O. Bellamy, P. Budden, C. Cole, J. Darke, E. Davies, D. Feliciano, and A. Gault, "Net zero technical report; committee on climate change," tech. rep., Committee on Climate Change, 2019.

[23] I. Komusanac, D. Fraile, and G. Brindley, "Wind energy in europe in 2018," tech. rep., WindEurope, 2018.

[24] W. Musial, P. Beiter, P. Schwabe, T. Tian, T. Stehly, and P. Spitsen, "2016 Offshore wind technologies market report," *U.S. Department of Energy*, 2016.

[25] T. Remy and A. Mbistrova, "Offshore wind in europe; key trends and statistics 2017," tech. rep., Wind Europe, 2018.

[26] C. W. Zheng, C. Y. Li, J. Pan, M. Y. Liu, and L. L. Xia, "An overview of global ocean wind energy resource evaluations," *Renewable and Sustainable Energy Reviews*, vol. 53, pp. 1240–1251, jan 2016.

[27] A.-K. Govindji, R. James, and A. Carvallo, "Appraisal of the offshore wind industry in japan," tech. rep., Carbon Trust, 2014.

[28] B. Nie and J. Li, "Technical potential assessment of offshore wind energy over shallow continent shelf along china coast," *Renewable Energy*, vol. 128, pp. 391–399, dec 2018.

[29] P. Hevia-Koch and H. K. Jacobsen, "Comparing offshore and onshore wind development considering acceptance costs," *Energy Policy*, vol. 125, pp. 9–19, feb 2019.

[30] G. Smart, "Offshore wind cost reduction; recent and future trends in the UK and Europe," tech. rep., ORE Catapult, 2016.

[31] P. Arwas and D. Charlesworth, "Offshore wind cost reduction; pathways project," tech. rep., The Crown Estate, 2012.

[32] "Offshore wind market development and cost reduction background," Tech. Rep. February, Energy UK, 2018.

[33] J. Koh and E. Ng, "Downwind offshore wind turbines: Opportunities, trends and technical challenges," *Renewable and Sustainable Energy Reviews*, vol. 54, pp. 797–808, feb 2016.

[34] M. Dyrholm, "Global wind report 2018," tech. rep., GWEC, 2019.

[35] "Driving cost reductions in offshore wind," tech. rep., Leanwind, 2017.

[36] P. Higgins and A. Foley, "The evolution of offshore wind power in the united kingdom," *Renewable and Sustainable Energy Reviews*, vol. 37, pp. 599–612, sep 2014.

[37] G. A. M. van Kuik, J. Peinke, R. Nijssen, D. Lekou, J. Mann, J. N. Sørensen, C. Ferreira, J. W. van Wingerden, D. Schlipf, P. Gebraad, H. Polinder, A. Abrahamsen, G. J. W. van Bussel, J. D. Sørensen, P. Tavner, C. L. Bottasso, M. Muskulus, D. Matha, H. J. Lindeboom, S. Degraer, O. Kramer, S. Lehnhoff, M. Sonnenschein, P. E. Sørensen, R. W. Künneke, P. E. Morthorst, and K. Skytte, "Long-term research

challenges in wind energy – a research agenda by the european academy of wind energy," *Wind Energy Science*, vol. 1, pp. 1–39, feb 2016.

[38] J. van Der Tempel, *Design of support structures for offshore wind turbines*. PhD thesis, Technical University of Delft, 2006.

[39] F. Vorpahl, H. Schwarze, T. Fischer, M. Seidel, and J. Jonkman, "Offshore wind turbine environment, loads, simulation, and design," *Wiley Interdisciplinary Reviews: Energy and Environment*, vol. 2, pp. 548–570, nov 2012.

[40] G. Corbetta, A. Mbistrova, and A. Ho, "Wind in power - 2015 European statistics," Tech. Rep. February, The European Wind Energy Association, 2016.

[41] C. Dunn, "Windfarms: has the death of the monopile been greatly exaggerated?." https://www.arup.com/perspectives/windfarms-the-death-of-the-monopile-has-been-greatly-exaggerated. Accessed: 25-04-2019.

[42] J. Jonkman, S. Butterfield, W. Musial, and G. Scott, "Definition of a 5-MW reference wind turbine for offshore system development," Tech. Rep. February, 2009.

[43] S. Hosseini, K. Barker, and J. E. Ramirez-Marquez, "A review of definitions and measures of system resilience," *Reliability Engineering & System Safety*, vol. 145, pp. 47–61, jan 2016.

[44] P. Bocchini, D. M. Frangopol, T. Ummenhofer, and T. Zinke, "Resilience and sustainability of civil infrastructure: toward a unified approach," *Journal of Infrastructure Systems*, vol. 20, p. 04014004, jun 2014.

[45] B. M. Ayyub, "Systems resilience for multihazard environments: Definition, metrics, and valuation for decision making," *Risk Analysis*, vol. 34, pp. 340–355, jul 2013.

[46] T. W. House, *Presidential policy directive 21: Critical infrastructure security and resilience*, pp. 37–53. 01 2014.

[47] A. Decò, P. Bocchini, and D. M. Frangopol, "A probabilistic approach for the prediction of seismic resilience of bridges," *Earthquake Engineering & Structural Dynamics*, vol. 42, pp. 1469–1487, jan 2013.

[48] S. E. Quiel, S. M. Marjanishvili, and B. P. Katz, "Performance-based framework for quantifying structural resilience to blast-induced damage," *Journal of Structural Engineering*, vol. 142, p. C4015004, aug 2016.

[49] M. Bruneau and A. Reinhorn, "Exploring the concept of seismic resilience for acute care facilities," *Earthquake Spectra*, vol. 23, pp. 41–62, feb 2007.

[50] B. R. Ellingwood, "Structural reliability and performance-based engineering," *Proceedings of the Institution of Civil Engineers - Structures and Buildings*, vol. 161, no. 4, pp. 199–207, 2008.

[51] K. Mitchell-Wallace, M. Jones, J. Hillier, and M. Foote, *Natural catastrophe risk management and modelling.* John Wiley & Sons, 2017.

[52] T. Rossetto, I. Ioannou, D. N. Grant, and T. Maqsood, "Guidelines for empirical vulnerability assessment," tech. rep., GEM, 2014.

[53] H. Crowley and V. Silva, "OpenQuake engine book: risk v 1.0.0," tech. rep., GEM Foundation, Pavia, Italy, 2013.

[54] M. Barbato, F. Petrini, V. U. Unnikrishnan, and M. Ciampoli, "Performance-based hurricane engineering (PBHE) framework," *Structural Safety*, vol. 45, pp. 24–35, nov 2013.

[55] M. Ciampoli, F. Petrini, and G. Augusti, "Performance-based wind engineering: Towards a general procedure," *Structural Safety*, vol. 33, pp. 367–378, sep 2011.

[56] H. Park, D. T. Cox, and A. R. Barbosa, "Probabilistic tsunami hazard assessment (PTHA) for resilience assessment of a coastal community," *Natural Hazards*, vol. 94, pp. 1117–1139, aug 2018.

[57] N. Attary, V. U. Unnikrishnan, J. W. van de Lindt, D. T. Cox, and A. R. Barbosa, "Performance-based tsunami engineering methodology for risk assessment of structures," *Engineering Structures*, vol. 141, pp. 676–686, jun 2017.

[58] J. P. Pinelli and M. Barbato, "A comparison study of catastrophe modeling vs. performance-based design," in *13th International Conference on Applications of Statistics and Probability in Civil Engineering (ICASP13)*, IASSAR, 2019.

[59] K. Bakalis and D. Vamvatsikos, "Seismic fragility functions via nonlinear response history analysis," *Journal of Structural Engineering*, vol. 144, oct 2018.

[60] F. Biondini and D. M. Frangopol, "Life-cycle performance of deteriorating structural systems under uncertainty: Review," *Journal of Structural Engineering*, vol. 142, sep 2016.

[61] K. Pitilakis, H. Crowley, and A. M. Kaynia, *SYNER-G : typology definition and fragility functions for physical elements at seismic risk*. Springer Science + Buisiness Media, 2014.

[62] T. Rossetto, I. Ioannou, D. Grant, and T. Maqsood, "Guidelines for empirical vulnerability assessment, gem technical report 2014-08 v1.0.0," tech. rep., GEM Foundation, 2014.

[63] V. Silva, S. Akkar, J. Baker, P. Bazzurro, J. M. Castro, H. Crowley, M. Dolsek, C. Galasso, S. Lagomarsino, R. Monteiro, D. Perrone, K. Pitilakis, and D. Vamvatsikos, "Current challenges and future trends in analytical fragility and vulnerability modelling," *Earthquake Spectra*.

[64] R. E. Melchers and A. T. Beck, *Structural reliability analysis and prediction*. John Wiley & Sons, 3rd ed., 2018.

[65] A. Forrester, A. Sobester, and A. Keane, *Engineering Design via Surrogate Modelling: A Practical Guide*. Wiley, 2008.

[66] T. J. Santner, B. J. Williams, and W. I. Notz, *The Design and Analysis of Computer Experiments*. Springer New York, 2003.

[67] A. Mentes and O. Turan, "A new resilient risk management model for offshore wind turbine maintenance," *Safety Science*, jun 2018.

[68] Q. Feng, X. Zhao, D. Fan, B. Cai, Y. Liu, and Y. Ren, "Resilience design method based on meta-structure: A case study of offshore wind farm," *Reliability Engineering & System Safety*, vol. 186, pp. 232–244, jun 2019.

[69] L. Ferrari, G. Soldi, A. Bianchini, and E. Dalpane, "Statistical analysis of component failures: A 16-year survey on more than 550 wind turbines," in *Volume 9: Oil and Gas Applications; Supercritical CO2 Power Cycles; Wind Energy*, ASME, jun 2018.

[70] J. Ribrant and L. M. Bertling, "Survey of failures in wind power systems with focus on swedish wind power plants during 1997–2005," *IEEE Transactions on Energy Conversion*, vol. 22, pp. 167–173, mar 2007.

[71] J. M. P. Pérez, F. P. G. Márquez, A. Tobias, and M. Papaelias, "Wind turbine reliability analysis," *Renewable and Sustainable Energy Reviews*, vol. 23, pp. 463–472, jul 2013.

[72] P. J. Tavner, J. Xiang, and F. Spinato, "Reliability analysis for wind turbines," *Wind Energy*, vol. 10, pp. 1–18, jan 2007.

[73] T. M. Delorm, Y. Lu, A. Christou, and P. McCluskey, "Comparisons of offshore wind turbine reliability," *Proceedings of the Institution of Mechanical Engineers, Part O: Journal of Risk and Reliability*, vol. 230, pp. 251–264, feb 2016.

[74] I. Lazakis and M. A. Kougioumtzoglou, "Assessing offshore wind turbine reliability and availability," *Proceedings of the Institution of Mechanical Engineers, Part M: Journal of Engineering for the Maritime Environment*, vol. 233, pp. 267–282, nov 2017.

[75] M. Leimeister and A. Kolios, "A review of reliability-based methods for risk analysis and their application in the offshore wind industry," *Renewable and Sustainable Energy Reviews*, vol. 91, pp. 1065–1076, aug 2018.

[76] Z. Jiang, W. Hu, W. Dong, Z. Gao, and Z. Ren, "Structural reliability analysis of wind turbines: A review," *Energies*, vol. 10, p. 2099, dec 2017.

[77] B. Jonkman and J. Jonkman, "FAST Readme v8.12.00a-bjj," tech. rep., NREL, Denver, 2015.

[78] J. Jonkman, S. Butterfield, T. Camp, J. Nichols, J. Azcona, and A. Martinez, "Offshore code comparison collaboration within iea wind annex xxiii : Phase ii results regarding monopile foundation modeling," in *IEA European Offshore Wind Conference*, no. January, p. 15, 2008.

[79] P. Haselbach, A. Natarajan, R. G. Jiwinangun, and K. Branner, "Comparison of coupled and uncoupled load simulations on a jacket support structure," *Energy Procedia*, vol. 35, pp. 244–252, 2013.

[80] M. Seidel, S. Voormeeren, and J.-B. van der Steen, "State-of-the-art design processes for offshore wind turbine support structures," *Stahlbau*, vol. 85, no. 9, pp. 583–590, 2016.

[81] S. Schafhirt and M. Muskulus, "Decoupled simulations of offshore wind turbines with reduced rotor loads and aerodynamic damping," *Wind Energy Science*, vol. 3, pp. 25–41, feb 2018.

[82] DNV GL, "DNVGL-RP-C205. Environmental conditions and environmental loads," 2017.

[83] E. Marino, C. Lugni, and C. Borri, "A novel numerical strategy for the simulation of irregular nonlinear waves and their effects on the dynamic response of offshore wind turbines," *Computer Methods in Applied Mechanics and Engineering*, vol. 255, pp. 275–288, mar 2013.

[84] E. Marino, C. Lugni, and C. Borri, "The role of the nonlinear wave kinematics on the global responses of an OWT in parked and operating conditions," *Journal of Wind Engineering and Industrial Aerodynamics*, vol. 123, pp. 363–376, dec 2013.

[85] M. Damgaard, L. Andersen, L. Ibsen, H. Toft, and J. Sørensen, "A probabilistic analysis of the dynamic response of monopile foundations: Soil variability and its consequences," *Probabilistic Engineering Mechanics*, vol. 41, pp. 46–59, jul 2015.

[86] C. Chen and P. Duffour, "Modelling damping sources in monopile-supported offshore wind turbines," *Wind Energy*, vol. 21, pp. 1121–1140, jun 2018.

[87] A. M. Page, V. Næss, J. B. D. Vaal, G. R. Eiksund, and T. A. Nygaard, "Impact of foundation modelling in offshore wind turbines: Comparison between simulations and field data," *Marine Structures*, vol. 64, pp. 379–400, mar 2019.

[88] R. Shirzadeh, W. Weijtjens, P. Guillaume, and C. Devriendt, "The dynamics of an offshore wind turbine in parked conditions: A comparison between simulations and measurements," *Wind Energy*, vol. 18, pp. 1685–1702, jul 2015.

[89] A. M. Page, G. R. Schafhirt, Sebastian; Eiksund, H. P. Skau, Kristoffer Skjolden Jostad, and H. Sturm, "Alternative numerical pile foundation models for integrated analyses of monopile-based offshore wind turbines," *Proceedings of the Twenty-sixth International Ocean and Polar Engineering Conference - ISOPE 2016*, pp. 111–119, 2016.

[90] M. Muskulus and S. Schafhirt, "Reliability-based design of wind turbine support structures," *Proc SRES 2015*, vol. 1, no. October 2015, pp. 1–13, 2015.

[91] DNV GL, "DNVGL-ST-0126. Support structures for wind turbines," 2016.

[92] A. Jay, A. T. Myers, S. Torabian, A. Mahmoud, E. Smith, N. Agbayani, and B. W. Schafer, "Spirally welded steel wind towers: Buckling experiments, analyses, and research needs," *Journal of Constructional Steel Research*, vol. 125, pp. 218–226, oct 2016.

[93] K.-S. Lee and H.-J. Bang, "A study on the prediction of lateral buckling load for wind turbine tower structures," *International Journal of Precision Engineering and Manufacturing*, vol. 13, pp. 1829–1836, sep 2012.

[94] International Electrotechnical Commission, "IEC 61400-1. Wind turbines part 1: design requirements," 2005.

[95] A. Morató, S. Sriramula, and N. Krishnan, "Kriging models for aeroelastic simulations and reliability analysis of offshore wind turbine support structures," *Ships and Offshore Structures*, vol. 0, pp. 1–14, sep 2018.

[96] C. Hübler, C. G. Gebhardt, and R. Rolfes, "Assessment of a standard ULS design procedure for offshore wind turbine sub-structures," *Journal of Physics Conference Series*, vol. 1104, p. 012013, oct 2018.

[97] British Standard Institution, "EN ISO 19901-1: 2005 petroleum and natural gas industries - specific requirements for offshore structures," tech. rep., 2005.

[98] B. S. Institution, "EN ISO 19902: 2007 + a1:2013 petroleum and natural gas industries - fixed steel offshore structures," tech. rep., 2007.

[99] X. Chen, C. Li, and J. Tang, "Structural integrity of wind turbines impacted by tropical cyclones: A case study from china," in *Journal of Physics: Conference Series*, vol. 753, IOP Publishing, sep 2016.

[100] DNV GL, "Fatigue design of offshore steel structures," tech. rep., DNV GL, 2016.

[101] I. Rychlik, "A new definition of the rainflow cycle counting method," *International Journal of Fatigue*, vol. 9, pp. 119–121, apr 1987.

[102] L. Ziegler, S. Schafhirt, M. Scheu, and M. Muskulus, "Effect of load sequence and weather seasonality on fatigue crack growth for monopile-based offshore wind turbines," *Energy Procedia*, vol. 94, pp. 115–123, sep 2016.

[103] D. Zwick and M. Muskulus, "Simplified fatigue load assessment in offshore wind turbine structural analysis," *Wind Energy*, vol. 19, pp. 265–278, feb 2015.

[104] K. Müller and P. W. Cheng, "Validation of uncertainty in IEC damage calculations based on measurements from alpha ventus," *Energy Procedia*, vol. 94, pp. 133–145, sep 2016.

[105] J. D. Sørensen and H. S. Toft, "Probabilistic design of wind turbines," *Energies*, vol. 3, pp. 241–257, feb 2010.

[106] A. Golafshani, V. Bagheri, H. Ebrahimian, and T. Holmas, "Incremental wave analysis and its application to performance-based assessment of jacket platforms," *Journal of Constructional Steel Research*, vol. 67, pp. 1649–1657, oct 2011.

[107] K. Wei, A. T. Myers, S. R. Arwade, S. Hallowell, J. Hajjar, and E. Hines, "Performance levels and fragility for offshore wind turbine support structures during extreme events," in *ASCE Structures Congress 2015* (N. In-

graffe and M. Libby, eds.), (Portland, Oregon), pp. 1891–1902, ASCE, 2015.

[108] M. Muskulus, "Simplified rotor load models and fatigue damage estimates for offshore wind turbines," *Philosophical Transactions of the Royal Society of London A: Mathematical, Physical and Engineering Sciences*, vol. 373, no. 2035, 2015.

[109] D. H. Kim and S. G. Lee, "Reliability analysis of offshore wind turbine support structures under extreme ocean environmental loads," *Renewable Energy*, vol. 79, pp. 161–166, jul 2015.

[110] A. Quilligan, A. O'Connor, and V. Pakrashi, "Fragility analysis of steel and concrete wind turbine towers," *Engineering Structures*, vol. 36, pp. 270–282, mar 2012.

[111] M. Mardfekri, P. Gardoni, and J. M. Roesset, "Probabilistic demand model based on the virtual work method and fragility estimates for offshore wind turbine support structures," *Civil Engineering*, no. 2008, pp. 1200–1205, 2011.

[112] M. Mardfekri and P. Gardoni, "Probabilistic demand models and fragility estimates for offshore wind turbine support structures," *Engineering Structures*, vol. 52, pp. 478–487, jul 2013.

[113] M. Mardfekri and P. Gardoni, "Multi-hazard reliability assessment of offshore wind turbines," *Wind Energy*, vol. 18, pp. 1433–1450, may 2014.

[114] S. T. Hallowell, A. T. Myers, S. R. Arwade, W. Pang, P. Rawal, E. M. Hines, J. F. Hajjar, C. Qiao, V. Valamanesh, K. Wei, W. Carswell, and C. M. Fontana, "Hurricane risk assessment of offshore wind turbines," *Renewable Energy*, vol. 125, pp. 234–249, sep 2018.

[115] R. D. Risi, S. Bhattacharya, and K. Goda, "Seismic performance assessment of monopile-supported offshore wind turbines using unscaled

natural earthquake records," *Soil Dynamics and Earthquake Engineering*, vol. 109, pp. 154–172, jun 2018.

[116] B. Yeter, Y. Garbatov, and C. Soares, "Fatigue reliability assessment of an offshore supporting structure," in *Maritime Technology and Engineering*, pp. 671–680, CRC Press, sep 2014.

[117] W. Dong, T. Moan, and Z. Gao, "Fatigue reliability analysis of the jacket support structure for offshore wind turbine considering the effect of corrosion and inspection," *Reliability Engineering & System Safety*, vol. 106, pp. 11–27, oct 2012.

[118] D. Veldkamp, "A probabilistic evaluation of wind turbine fatigue design rules," *Wind Energy*, vol. 11, pp. 655–672, nov 2008.

[119] K. Wei, S. R. Arwade, and A. T. Myers, "Incremental wind-wave analysis of the structural capacity of offshore wind turbine support structures under extreme loading," *Engineering Structures*, vol. 79, pp. 58–69, nov 2014.

[120] D. Zwick and M. Muskulus, "The simulation error caused by input loading variability in offshore wind turbine structural analysis," *Wind Energy*, vol. 18, no. 8, pp. 1421–1432, 2015.

[121] I. Abdallah, A. Natarajan, and J. Sørensen, "Influence of the control system on wind turbine loads during power production in extreme turbulence: Structural reliability," *Renewable Energy*, vol. 87, pp. 464–477, mar 2016.

[122] M. Muskulus, "Why design load calculations for OWT SS cannot use load time series from moving rotors," in *Proceedings of the 25th (2015) International Ocean and Polar Engineering Conference*, (Kona), International Society of Offshore and Polar Engineers, 2015.

[123] S. Rose, P. Jaramillo, M. J. Small, and J. Apt, "Quantifying the hurricane catastrophe risk to offshore wind power," *Risk Analysis*, vol. 33, pp. 2126–2141, jun 2013.

[124] P. Grossi and H. Kunreuther, eds., *Catastrophe modeling: a new approach to managing risk*. Springer Science + Buisiness Media, 2005.

[125] K. Porter, K. Farokhnia, D. Vamvatsikos, and I. Cho, "Guidelines for component-based analytical vulnerability assessment of buildings and nonstructural elements, GEM Technical Report 2014-13 V1.0.0," tech. rep., GEM Foundation, Pavia, Italy, 2014.

[126] I. Iervolino, "Assessing uncertainty in estimation of seismic response for PBEE," *Earthquake Engineering & Structural Dynamics*, vol. 46, pp. 1711–1723, feb 2017.

[127] B. Efron and R. Tibshirani, *An introduction to the bootstrap*. New York: Chapman & Hall, 1993.

[128] DNVGL, "DNVGL-RP-C205 environmental conditions and environmental loads," Tech. Rep. August, 2017.

[129] F. Jalayer and C. A. Cornell, "Alternative non-linear demand estimation methods for probability-based seismic assessments," *Earthquake Engineering & Structural Dynamics*, vol. 38, pp. 951–972, jul 2009.

[130] A. F. Mensah and L. Dueñas-Osorio, "A closed-form technique for the reliability and risk assessment of wind turbine systems," *Energies*, vol. 5, pp. 1734–1750, jun 2012.

[131] T. Fischer, W. de Vries, and B. Schmidt, "Upwind design basis - WP4," tech. rep., University of Stuttgart, 2010.

[132] DNVGL, "Environmental conditions and environmental loads," 2017.

[133] P. Agarwal and L. Manuel, "Incorporating irregular nonlinear waves in coupled simulation and reliability studies of offshore wind turbines," *Applied Ocean Research*, vol. 33, pp. 215–227, jul 2011.

[134] J. Jonkman, A. Robertson, and G. Hayman, "HydroDyn user's guide and theory manual," Tech. Rep. March, NREL, Denver, 2015.

[135] N. D. Kelley and B. Jonkman, "NREL/TP-500-41137. Overview of the turbsim stochastic inflow turbulence simulator," tech. rep., NREL, 2007.

[136] A. Morató, S. Sriramula, N. Krishnan, and J. Nichols, "Ultimate loads and response analysis of a monopile supported offshore wind turbine using fully coupled simulation," *Renewable Energy*, vol. 101, pp. 126–143, feb 2017.

[137] B. R. Resor, "SAND2013-2569, Definition of a 5MW/61.5m wind turbine blade reference model," Tech. Rep. April, Sandia National Laboratories, Albuquerque, 2013.

[138] Y.-S. Lee, B.-L. Choi, J. H. Lee, S. Y. Kim, and S. Han, "Reliability-based design optimization of monopile transition piece for offshore wind turbine system," *Renewable Energy*, vol. 71, pp. 729–741, nov 2014.

[139] M. Achmus and K. Abdel-Rahman, "Finite element modelling of horizontally loaded monopile foundations for offshore wind energy converters in Germany," in *Frontiers in Offshore Geotechnics*, no. July, pp. 391–396, Taylor & Francis, aug 2005.

[140] C. Gebhardt and B. Roccia, "Non-linear aeroelasticity: An approach to compute the response of three-blade large-scale horizontal-axis wind turbines," *Renewable Energy*, vol. 66, pp. 495 – 514, 2014.

[141] S. Hallowell and A. T. Myers, "Site-specific variability of load extremes of offshore wind turbines exposed to hurricane risk and breaking waves," *Wind Energy*, vol. 20, pp. 143–157, may 2016.

[142] N. J. Tarp-johansen, I. Kozine, L. Radermakers, J. D. Sørensen, and K. Ronold, "Optimised and balanced structural and system reliability of offshore wind turbines: an account; Riso-R-1420," Tech. Rep. April, Roskilde, 2005.

[143] Joint Committee Structural Safety, "JCSS Probabilistic Model Code," tech. rep., Technical University of Denmark, 2013.

[144] British Standard Institution, "EN 1993-1-6. Eurocode 3: design of steel structures - part 1-6: strength and stability of shell structures," 2009.

[145] DNV GL, "DNV-RP-C202. Buckling strength of shells," 2013.

[146] British Standard Institution, "BS EN 1993-1-1:2005+A1:2014. Eurocode 3 - Design of steel structures - Part 1-1: general rules and rules for buildings," Tech. Rep. 2014, 2005.

[147] I. Lotsberg, "Structural mechanics for design of grouted connections in monopile wind turbine structures," *Marine Structures*, vol. 32, pp. 113–135, jul 2013.

[148] M. Rosemeier, P. Berring, and K. Branner, "Non-linear ultimate strength and stability limit state analysis of a wind turbine blade," *Wind Energy*, vol. 19, pp. 825–846, jun 2015.

[149] K. Porter, "A beginner's guide to fragility, vulnerability, and risk," 2017.

[150] D. Lallemant, A. Kiremidjian, and H. Burton, "Statistical procedures for developing earthquake damage fragility curves," *Earthquake Engineering & Structural Dynamics*, vol. 44, pp. 1373–1389, jan 2015.

[151] "Study of the costs of offshore wind generation; a report to the renewables advisory board & DTI," tech. rep., Department for Trade and Industry, 2007.

[152] M. Dicorato, G. Forte, M. Pisani, and M. Trovato, "Guidelines for assessment of investment cost for offshore wind generation," *Renewable Energy*, vol. 36, pp. 2043–2051, aug 2011.

[153] C. Mone, A. Smith, B. Maples, and M. Hand, "2013 Cost of wind energy review; NREL/TP-5000-63267," tech. rep., National Renewable Energy Laboratory, 2015.

[154] K. Fischer, C. Viljoen, J. Köhler, and M. H. Faber, "Optimal and acceptable reliabilities for structural design," *Structural Safety*, vol. 76, pp. 149–161, jan 2019.

[155] A. A. Taflanidis, E. Loukogeorgaki, and D. C. Angelides, "Offshore wind turbine risk quantification/evaluation under extreme environmental conditions," *Reliability Engineering & System Safety*, vol. 115, pp. 19–32, jul 2013.

[156] C. Hübler, C. G. Gebhardt, and R. Rolfes, "Methodologies for fatigue assessment of offshore wind turbines considering scattering environmental conditions and the uncertainty due to finite sampling," *Wind Energy*, vol. 21, pp. 1092–1105, jun 2018.

[157] A. K. Chorpa, *Dynamics of structures*. Prentice Hall, 4th ed., 2012.

[158] DNV GL, "DNV-OS-J101. Design of offshore wind turbine structures," 2014.

[159] M. Kuhn, *Dynamics and design optimization of offshore wind conversion systems*. PhD thesis, Delft University of Technology, 2001.

[160] J. Häfele, C. G. Gebhardt, and R. Rolfes, "A comparison study on jacket substructures for offshore wind turbines based on optimization," *Wind Energy Science*, 2018.

[161] H. S. Toft, L. Svenningsen, W. Moser, J. D. Sørensen, and M. L. Thøgersen, "Assessment of wind turbine structural integrity using response surface methodology," *Engineering Structures*, vol. 106, pp. 471–483, jan 2016.

[162] Q. Huchet, C. Mattranda, P. Beaurepaire, N. Gayton, and N. Relun, "The help of metamodels for the wind turbine certification," in *Safety, Reliability, Risk, Resilience and Sustainability of Structures and Infrastructure*, IASSAR, 2017.

[163] S. Brandt, M. Broggi, J. Häfele, C. G. Gebhardt, R. Rolfes, and M. Beer, "Meta-models for fatigue damage estimation of offshore wind turbines jacket substructures," *Procedia Engineering*, vol. 199, pp. 1158–1163, 2017.

[164] J. Häfele, R. Damiani, R. King, C. G. Gebhardt, and R. Rolfes, "A systematic approach to offshore wind turbine jacket pre-design and optimization: geometry, cost, and surrogate structural code check models," *Wind Energy Science*, pp. 1–29, may 2018.

[165] N. Barltrop and A. Adams, *Dynamics of Fixed Marine Structures*. Butterworth Heinmann, 3rd ed., 1991.

[166] L. Ziegler, S. Voormeeren, S. Schafhirt, and M. Muskulus, "Design clustering of offshore wind turbines using probabilistic fatigue load estimation," *Renewable Energy*, vol. 91, pp. 425–433, jun 2016.

[167] S. Márquez-Domínguez and J. D. Sørensen, "Fatigue reliability and calibration of fatigue design factors for offshore wind turbines," *Energies*, vol. 5, pp. 1816–1834, jun 2012.

[168] J. Oest, R. Sørensen, L. C. T. Overgaard, and E. Lund, "Structural optimization with fatigue and ultimate limit constraints of jacket structures for large offshore wind turbines," *Structural and Multidisciplinary Optimization*, vol. 55, pp. 779–793, jul 2016.

[169] DNV GL, "Probabilistic methods for planning of inspection for fatigue cracks in offshore structures," Tech. Rep. May, 2015.

[170] C. H. Lange, "Probabilistic fatigue methodology and wind turbine reliability," Tech. Rep. May, Sandia National Laboratories, 1996.

[171] J. L. Beck and K. M. Zuev, *Rare-event simulation*. Springer International Publishing, 2015.

[172] A. O'Hagan, "Bayesian analysis of computer code outputs: A tutorial," *Reliability Engineering & System Safety*, vol. 91, pp. 1290–1300, oct 2006.

[173] L. Ziegler, S. Voormeeren, S. Schafhirt, and M. Muskulus, *Sensitivity of wave fatigue loads on offshore wind turbines under varying site conditions*, vol. 80. Elsevier BV, 2015.

[174] C. Hübler, C. G. Gebhardt, and R. Rolfes, "Hierarchical four-step global sensitivity analysis of offshore wind turbines based on aeroelastic time domain simulations," *Renewable Energy*, vol. 111, pp. 878–891, oct 2017.

[175] H. S. Toft, L. Svenningsen, J. D. Sørensen, W. Moser, and M. L. Thøgersen, "Uncertainty in wind climate parameters and their influence on wind turbine fatigue loads," *Renewable Energy*, vol. 90, pp. 352–361, may 2016.

[176] C. Rasmussen and C. Williams, *Gaussian processes for machine learning*. Cambridge: MIT Press, 2006.

[177] M. Stein, *Interpolation of spatial data: some theory for kriging*. New York: Springer, 1999.

[178] E. Bush and L. Manuel, "The influence of foundation modeling assumptions on long-term load prediction for offshore wind turbines," in *Proceedings of the ASME 28th International Conference on Ocean. Offshore and Artic Engineering*, (Honolulu), pp. 1–9, ASME, 2009.

[179] M. Damgaard, V. Zania, L. Andersen, and L. Ibsen, "Effects of soil–structure interaction on real time dynamic response of offshore wind turbines on monopiles," *Engineering Structures*, vol. 75, pp. 388–401, sep 2014.

[180] A. M. Mood, F. A. Graybill, and D. C. Boes, *Introduction to the theory of statistics*. Singapore: McGraw-Hill, third ed., 1974.

[181] Q. Huchet, C. Mattrand, P. Beaurepaire, N. Relun, and N. Gayton, "AK-DA: An efficient method for the fatigue assessment of wind turbine structures," *Wind Energy*, vol. 22, pp. 638–652, jan 2019.

[182] DNV, "Classification notes no30.6. structural reliability analysis of marine structures," tech. rep., 1992.

[183] J. Häfele, C. Hübler, C. G. Gebhardt, and R. Rolfes, "An improved two-step soil-structure interaction modelling method for dynamical analyses of offshore wind turbines," *Applied Ocean Research*, vol. 55, pp. 141–150, feb 2016.

[184] V. Valamanesh, A. Myers, and S. Arwade, "Multivariate analysis of extreme metocean conditions for offshore wind turbines," *Structural Safety*, vol. 55, pp. 60–69, jul 2015.

[185] J. M. Jonkman and B. J. Jonkman, "FAST modularization framework for wind turbine simulation: full-system linearization," *Journal of Physics: Conference Series*, vol. 753, p. 082010, 2016.

[186] V. Negro, J.-S. López-Gutiérrez, M. D. Esteban, P. Alberdi, M. Imaz, and J.-M. Serraclara, "Monopiles in offshore wind: Preliminary estimate of main dimensions," *Ocean Engineering*, vol. 133, pp. 253–261, mar 2017.

[187] J. D. Sørensen, "Reliability assessment of wind turbines," in *12th International Conference on Applications of Statistics in Probability and Civil Engineering*, (Vancouver), The University of British Columbia, 2015.

[188] E. Bush and L. Manuel, "Foundation models for offshore wind turbines," in *47th AIAA Aerospace Sciences Meeting Including The New Horizons Forum and Aerospace Exposition*, no. January, (Orlando), 2009.

[189] S. Jung, S.-R. Kim, A. Patil, and L. C. Hung, "Effect of monopile foundation modeling on the structural response of a 5-MW offshore wind turbine tower," *Ocean Engineering*, vol. 109, pp. 479–488, nov 2015.

[190] V. L. Krathe and A. M. Kaynia, "Implementation of a non-linear foundation model for soil-structure interaction analysis of offshore wind turbines in FAST," *Wind Energy*, vol. 20, pp. 695–712, sep 2016.

[191] M. Damgaard, L. Andersen, and L. Ibsen, "Computationally efficient modelling of dynamic soil–structure interaction of offshore wind turbines on gravity footings," *Renewable Energy*, vol. 68, pp. 289–303, aug 2014.

[192] W. Carswell, J. Johansson, F. Løvholt, S. Arwade, C. Madshus, D. DeGroot, and A. Myers, "Foundation damping and the dynamics of offshore wind turbine monopiles," *Renewable Energy*, vol. 80, pp. 724–736, aug 2015.

[193] M. Zaaijer, "Foundation modelling to assess dynamic behaviour of offshore wind turbines," *Applied Ocean Research*, vol. 28, pp. 45–57, feb 2006.

[194] S. Krammer, *Geotechnical earthquake engineering*. Prentice Hall, 1996.

[195] M. Damgaard, *Dynamic properties of offshore wind turbine foundations*. PhD thesis, Aalborg University, 2014.

[196] L. Arany, S. Bhattacharya, J. Macdonald, and S. J. Hogan, "Design of monopiles for offshore wind turbines in 10 steps," *Soil Dynamics and Earthquake Engineering*, vol. 92, no. November 2015, pp. 126–152, 2017.

[197] P. Brodtkorb, P. Johannesson, G. Lindgren, I. Rychlik, J. Ryden, and E. Sjo, "WAFO - a Matlab toolbox for analysis of random waves and loads," in *Proc. 10th Int. Offshore and Polar Eng. Conf*, vol. 3, (Seattle), pp. 343–350, 2000.

[198] J. Przemieniecki, *Theory of matrix structural analysis*. McGraw-Hill, 1969.

[199] G. Bir, "User's guide to bmodes (software for computing rotating beam coupled modes)," Tech. Rep. September, National Renewable Energy Laboratory, 2007.

[200] R. Clough and J. Penzien, *Dynamics of structures*. McGraw-Hill, second ed., 1993.

[201] W. Carswell, S. R. Arwade, D. J. DeGroot, and M. A. Lackner, "Soil-structure reliability of offshore wind turbine monopile foundations," *Wind Energy*, vol. 18, pp. 483–498, jan 2014.